INFORMATION TO USERS

This manuscript has been reproduced from the microfilm master. UMI films the text directly from the original or copy submitted. Thus, some thesis and dissertation copies are in typewriter face, while others may be from any type of computer printer.

The quality of this reproduction is dependent upon the quality of the copy submitted. Broken or indistinct print, colored or poor quality illustrations and photographs, print bleedthrough, substandard margins, and improper alignment can adversely affect reproduction.

In the unlikely event that the author did not send UMI a complete manuscript and there are missing pages, these will be noted. Also, if unauthorized copyright material had to be removed, a note will indicate the deletion.

Oversize materials (e.g., maps, drawings, charts) are reproduced by sectioning the original, beginning at the upper left-hand corner and continuing from left to right in equal sections with small overlaps. Each original is also photographed in one exposure and is included in reduced form at the back of the book.

Photographs included in the original manuscript have been reproduced xerographically in this copy. Higher quality 6" x 9" black and white photographic prints are available for any photographs or illustrations appearing in this copy for an additional charge. Contact UMI directly to order.

UMI

A Bell & Howell Information Company
300 North Zeeb Road, Ann Arbor, MI 48106-1346 USA
313/761-4700 800/521-0600

EXTINCTION OF ULTRAVIOLET-A, VISIBLE AND NEAR INFRARED WAVELENGTH LIGHT IN SNOW AND ANTARCTIC SEA ICE

A

THESIS

Presented to the Faculty

of the University of Alaska Fairbanks

in Partial Fulfillment of the Requirements

for the Degree of

DOCTOR OF PHILOSOPHY

By

Timothy Kyle Quakenbush, B.S.

Fairbanks, Alaska

December 1994

EXTINCTION OF ULTRAVIOLET-A, VISIBLE AND NEAR INFRARED WAVELENGTH LIGHT IN SNOW AND ANTARCTIC SEA ICE

By

Timothy Kyle Quakenbush

RECOMMENDED:

Gunter Weller, Ph.D.

Glen Shaw, Ph.D.

Knut Stamnes, Ph.D.

William Stringer, Ph.D.

Gerd Wendler, Ph.D., Committee Chair

John Morack, Ph.D., Department Head

APPROVED:

Paul Reichardt, Ph.D., Dean, College of Natural Science

Joseph Kan, Ph.D., Dean, Graduate School

DEC. 20, 1994

Date

ABSTRACT

The optical properties of sea ice are important in the understanding of sea ice thermodynamics, growth and decay processes, polar climates, and remote sensing. The optical properties of ice have been fairly well described, but most studies have focused on wavelengths longer than 400 nm, and on Arctic sea ice. With increased interest in the effects of changing ultraviolet light levels from Antarctic ozone depletion, there has been recent work done on the extinction of ultraviolet light in Antarctic sea ice, including the study reported here.

A spectrometer was modified, and taken on two trips to Antarctica to measure the extinction of light in sea ice. Extinction in summer and in winter sea ice were measured in the wavelength range 320 to 900 nm with the resolution range of 1 to 6 nm. This wavelength range covers the ultraviolet A band (320 - 400 nm), photosynthetically active region (PAR, 400 - 700 nm), and a small part of the near infrared (NIR, 700 - 1000nm).

The extinction coefficient in the middle of melting sea ice had a minimum of 0.6 m^{-1} in the range of 450 - 500 nm, rising to 1 m^{-1} at 350 nm, and 1.8 at 700 nm. Winter sea ice had spectrally flat extinction between 320 - 600 nm with values ranging from 1.7 - 5 m^{-1} for different ice floes. This is in contrast to an expected minimum around 450 nm from absorption by ice and water. Extinction increased to 10 - 15 m^{-1} at 900 nm in the winter sea ice. Both warm and cold ice had increased extinction at all wavelengths near the bottom of the floes.

Algae were identified in several ice floes by the chlorophyll absorption peaks at 330, 430 and 680 nm. The presence of algae in the ice was associated with an increase in the extinction by a factor of up to 5 for wavelengths shorter than 600 nm, with a much smaller effect on longer wavelengths. Absorption by algae was evident at nearly all depths in some of the ice, but was mostly concentrated in the bottom 15% to 35%.

TABLE OF CONTENTS

LIST OF FIGURES

LIST OF TABLES

1. Introduction

The optical properties of sea ice have long been regions of interest. Albedo, transmission of light into the ocean, and absorption of light in the ice have been studied in visible (400 - 700 nm), near infrared (700 - 1000 nm) and infrared (1 - 15 μm) wavelengths to improve the understanding of the thermodynamics of sea ice in the polar oceans[1,2,3,4], biological studies[5,6,7,8,9,10,11] and to aid in remote sensing applications. More recent studies have been aimed at the ultraviolet A (UVA, 320 - 400 nm) and B (UVB, 280 - 320 nm) bands with respect to polar ozone depletion and possible effects of increased UVB on the biology in the ice and underlying water[12,5,13].

1.1 Measured Extinction in Terms of Absorption and Multiple Scattering

Before proceeding, it would be useful to review a two stream approximation to interpret in-situ extinction measurements in terms of absorption and scattering in the ice. The starting point is the radiative transfer equation[14] appropriate for planer geometries.

$$\mu \frac{dI(\Omega)}{dz} = -(\alpha+\sigma)I(\Omega) + \sigma \int_{4\pi} \frac{p(\Omega',\Omega)}{4\pi} I(\Omega')\, d\Omega'$$

where:

μ = cosine zenith angle to direction of travel = $(\vec{I} \bullet \hat{z})$

$I(\Omega)$ = radiance travelling along direction angle Ω

α = absorption coeficient per unit length

σ = scattering coeficient per unit length

$\frac{p(\Omega',\Omega)}{4\pi}$ = normalized phase function denoting the probability of light scattering from direction Ω'into Ω.

Equation 1.1

This is for monochromatic light travelling in a layered medium where α, σ and p are

functions of the depth (z). The direction angle can be expressed in spherical coordinates as $d\Omega = \sin(\theta)d\theta d\phi$. The left-hand side of Equation 1.1 represents the change in the amount of radiance travelling in direction Ω. The first term on the right side is the amount of radiance that was absorbed into nonradiative forms of energy ($-\alpha I(\Omega)$), plus the total amount of radiance that was scattered($-\sigma I(\Omega)$) into a direction other than Ω. The second term is the power that was scattered from all other directions into Ω. This is a power source term. Since sea ice is at terrestrial temperatures, and the wavelength of light is much shorter than the infrared band, the thermal emission source term was not included. The vertical coordinate is defined so that $z = 0$ at the top surface of the ice, and $z < 0$ below.

The purpose of this exercise is to manipulate Equation 1.1 into two equations describing the upward and downward travelling flux. With this in mind, the source multiple scattering term can be split into two integrals over the upward travelling ($+2\pi$) and downward travelling (-2π) hemispheres of Ω'.

$$\mu\frac{dI(\Omega)}{dz} = -(\alpha+\sigma)I(\Omega) + \sigma\int_{2\pi}\frac{p(\Omega',\Omega)}{4\pi}I(\Omega')\,d\Omega' + \sigma\int_{-2\pi}\frac{p(\Omega',\Omega)}{4\pi}I(\Omega')\,d\Omega'$$

Equation 1.2

To produce terms that describe upward flux, integrate both sides of Equation 1.2 over all upward travelling direction angles Ω.

$$\int_{2\pi}\mu\frac{dI(\Omega)}{dz}d\Omega = -(\alpha+\sigma)\int_{2\pi}I(\Omega)\,d\Omega + \sigma\int_{2\pi}\left[\int_{2\pi}\frac{p(\Omega',\Omega)}{4\pi}I(\Omega')\,d\Omega'\right]d\Omega + \sigma\int_{2\pi}\left[\int_{-2\pi}\frac{p(\Omega',\Omega)}{4\pi}I(\Omega')\,d\Omega'\right]d\Omega$$

Equation 1.3

Changing the order of integration in the two source multiple scattering terms allows the

separation of I(Ω') from the integral over the scattering phase function.

$$\int_{2\pi} \mu \frac{dI(\Omega)}{dz} d\Omega = (\alpha+\sigma) \int_{2\pi} I(\Omega)\, d\Omega$$

$$+ \sigma \int_{2\pi} I(\Omega') \left[\int_{2\pi} \frac{p(\Omega',\Omega)}{4\pi} d\Omega \right] d\Omega' + \sigma \int_{-2\pi} I(\Omega') \left[\int_{2\pi} \frac{p(\Omega',\Omega)}{4\pi} d\Omega \right] d\Omega'$$

Equation 1.4

Using the definitions of the fraction backscattering coefficient (β), upward flux(F^+), upward average intensity ($\langle I \rangle^-$), and downward average intensity ($\langle I \rangle^-$)

$$\beta = \int_{2\pi} \frac{p(\Omega,\Omega')}{4\pi} d\Omega = \int_{2\pi} \frac{p(\Omega',\Omega)}{4\pi} d\Omega = \int_{-2\pi} \frac{p(\Omega',\Omega)}{4\pi} d\Omega$$

for Ω and Ω' in opposite hemispheres

$$F^+ = \int_{2\pi} \mu\, I(\Omega)\, d\Omega$$

$$\langle I \rangle^{\pm} = \frac{\int_{\pm 2\pi} I(\Omega')\, d\Omega'}{\int_{\pm 2\pi} d\Omega'} = \frac{1}{2\pi} \int_{\pm 2\pi} I(\Omega')\, d\Omega'$$

Equations 1.5a, b, c

one finds Equation 1.4 may now be written as

$$\frac{dF^+}{dz} = -(\alpha+\sigma)2\pi \langle I\rangle^+ + \sigma(1-\beta)\, 2\pi \langle I\rangle^+ + \sigma\beta\, 2\pi \langle I\rangle^-.$$

Equation 1.6a

A similar equation for the downward flux is obtained by integrating equation 2 over the lower hemisphere of Ω

$$-\frac{dF^-}{dz} = -(\alpha+\sigma)2\pi \langle I\rangle^- + \sigma(1-\beta)\, 2\pi \langle I\rangle^- + \sigma\beta\, 2\pi \langle I\rangle^+.$$

Equation 1.6b

To get values of the absorption (α), single scattering (σ), and fractional backscattering (β) coefficients, measured values of upward and downward flux ($F^{\pm}$) and average intensity ($\langle I\rangle^{\pm}$) are needed at different depths in the ice. This would require more time than is available (approximately two days per site) when working from an ice breaker. There are also large sources of error in subtracting flux values ($dF^- \cong F^-(z_2) - F^-(z_1)$).

Approximating the average upward and downward intensities to be proportional to the corresponding fluxes, i.e.

$$F^{\pm} \cong A\, 2\pi \langle I\rangle^{\pm}$$

Equation 1.7

one obtains a pair of coupled equations known as the two stream approximation

$$\pm A\frac{dF^{\pm}}{dz} = -(\alpha+\sigma)F^{\pm} + \sigma(1-\beta)\, F^{\pm} + \sigma\beta\, F^{\mp}.$$

Equation 1.8

The value of the proportionality constant (A) depends on the problem of interest. It is common to use an average cosine of the zenith angle (μ). The approximation in Equation

1.7 requires the angular distribution of light to be very similar at different depths. This is an acceptable approximation when measuring light in a material with sufficient multiple scattering to convert any direct beam radiance into diffuse radiation. In this case Equation 1.8 can be used to get an idea of what is contained in flux extinction measurements. The solution to Equation 1.8 follows from assuming it to be exponential[14,15]

$$\begin{pmatrix} F^{+} \\ F^{-} \end{pmatrix} = \begin{pmatrix} A \\ B \end{pmatrix} e^{Kz} + \begin{pmatrix} C \\ D \end{pmatrix} e^{-Kz}$$

$$K = \frac{1}{A}\left[\alpha\,(\alpha + 2\sigma\beta)\right]^{1/2}.$$

Equation 1.9

The values of A, B, C and D depend on the boundary conditions. If the lower boundary is optically deep, then C and D must be zero because the increasing solutions are unacceptable. The coefficient K in Equation 1.9 is the apparent extinction of flux, and the absorption (α), scattering (σ) and backscattering fraction (β) coefficients are intrinsic properties of the material. In this thesis the apparent extinction will be referred to as extinction, and the intrinsic coefficients will be referred to as absorption, scattering, and backscattering coefficients with the understanding that they are apparent and intrinsic properties respectively. The apparent extinction (K) is calculated from the measured data ($F(z_1)$ and $F(z_2)$) as follows,

$$\frac{F(z_2)}{F(z_1)} = e^{K(z_2 - z_1)}.$$

Equation 1.10

The corresponding downward flux ratio from the two stream approximation relates the apparent flux extinction to the intrinsic absorption , single scattering, and fractional backscattering coefficients using Equation 1.9

$$K = \frac{1}{A}\left[\alpha\,(\alpha + 2\sigma\beta)\right]^{1/2}.$$

Equation 1.11

For the case where the extinction (K) is measured, Equation 1.11 can be rearranged to the following form to estimate the light backscattering ($\sigma\beta$), or absorption (α) given the other variables

$$\sigma\beta = \frac{\left((AK)^2 - \alpha^2\right)}{2\alpha}$$

or

$$\alpha = -\sigma\beta + \left[\left(\sigma\beta\right)^2 + (AK)^2\right]^{1/2}.$$

Equation 1.12

Beer's law is obtained by neglecting the multiple scattering term in Equation 1.1. Then the bulk extinction takes the form $K(z) = (\alpha(z) + \sigma(z)) / \mu$. The two stream approximation gives a simple approximation to the effects of multiple scattering of light in a material. If there is no light scattering ($\sigma = 0$), or if the material is very strongly forward scattering ($\beta = 0$) Equation 1.11 reduces to the Lambert - Beer law for an absorbing material ($K = \alpha/A$). An expression for absorption in the general case can be obtained by integrating Equation 1.1 over all direction angles Ω.

$$\int_{4\pi} \mu \frac{dI(\Omega)}{dz} d\Omega = -(\alpha+\sigma) \int_{4\pi} I(\Omega)\, d\Omega + \sigma \int_{4\pi} \left[\int_{4\pi} \frac{p(\Omega',\Omega)}{4\pi} I(\Omega')\, d\Omega' \right] d\Omega$$

$$\frac{d(F^+ - F^-)}{dz} = -(\alpha+\sigma)\, 4\pi \langle I \rangle + \sigma\, 4\pi \langle I \rangle = -4\pi\, \alpha \langle I \rangle$$

or

$$\alpha = \frac{-1}{4\pi \langle I \rangle} \frac{d(F^+ - F^-)}{dz}.$$

Equation 1.13

This has the similar experimental problem as Equation 6a and b. Subtracting the upward and downward flux can produce large errors unless the optical thickness (K dz) is large enough. For the purpose of this thesis, the extinction relation in Equations 1.11 and 1.12 will be used to estimate scattering in sea ice.

1.2 Previous Measurements of Sea Ice Optical Properties

A good early description of the optical properties of sea ice was made by Grenfell and Maykut[16]. They measured albedo and extinction in various types of snow and ice in the Arctic Basin. Their spectrometers [17] had small fields of view and were made to collect light from under an ice floe, or from horizontal holes drilled in ice or snow. The wavelength range of their data was from 400 to 750 nm. Their extinction data showed a similar spectral shape for all ice types with a minimum light loss in the 450 to 550 nm region and a large increase towards the longer wavelengths. The magnitudes at 500 nm ranged from about 15 m^{-1} for dry compact snow down to 0.6 m^{-1} for blue ice below an old melt pond.

Similar spectral extinction curves were measured by Perovich[18] in "artificially grown salt ice." He put light collectors at several depths in a tank of NaCl water and allowed it to freeze during the winter months. Glass fiber optic cables carried the light to a spectrometer[17]. The spectral shape followed the expected low values in the 400 to 550 nm

band rising fast towards longer wavelengths, but the magnitude of the curves were larger for cold salty ice than for pure ice.

As described earlier, the extinction of light in sea ice is a function of absorption and multiple scattering. In an effort to separate these two effects Grenfell and Perovich performed some well controlled experiments to measure the spectral absorption of pure, bubble-free ice. The first experiment[19] measured absorption in the wavelength range of 400 to 1400 nm, and later the same method[20] was used in the range 250 to 400 nm. Their method was to carefully grow ice blocks in a cold room and measure the spectra of a beam of light with and without the ice block in the optical path. The resulting absorption spectrum for pure bubble-free ice had values below 0.1 m^{-1} between 390 and 500 nm, increasing to about 0.7 m^{-1} at 250 nm, as well as toward longer wavelengths, with an absorption of 3 m^{-1} at 1000 nm. In the wavelength range of 400 - 600 nm, the absorption of light by pure bubble free ice is one to two orders of magnitude smaller than the extinction measured in real and artificial sea ice, but they are in the same order of magnitude for the wavelength range of 600 to 900 nm.

A study of the effects of light scattering in sea ice[21,22,23,24] was done by placing a lamp over the surface of an ice floe, and measuring the distribution of light exiting the top and bottom surfaces. Different filters, ranging from 250 nm to 700 nm, were placed in front of the lamp to get spectral data. The effects of scattering were found by matching parameters in a Monte Carlo model to the light distribution data. This method shows that an isotropically scattering material should make the light exit the bottom boundary in a much wider area than was measured. Forward scattering gives a better match to the data[23]. Extinction values for the ice were found by integrating the received light over the measurement area. They ranged from about 3.4 m^{-1} at 250 nm, to 2.4 m^{-1} at 350 nm, and back up to 4.5 m^{-1} at 700 nm.

Grenfell and Hedrick[25] measured the angular distribution of light from near single scattering in small samples of artificial salt ice. They directed a collimated beam of light at one side of small, polished monoliths cut from ice grown in a tank of saline water. Their

measurements gave the single scattering phase function in Equation 1.1 for various salinities and ice types. The measured phase functions were strongly forward peaked, as expected from bubbles and brine pockets much larger than the wavelength of light. A small scattering peak at 75° from the incident beam was observed in the glacier ice. This was expected because of internal refraction of rays at the air-ice surface of gas bubbles. The light scattering by salt ice was much more forward-peaked which fits the picture of brine pockets being the major source of light scattering.

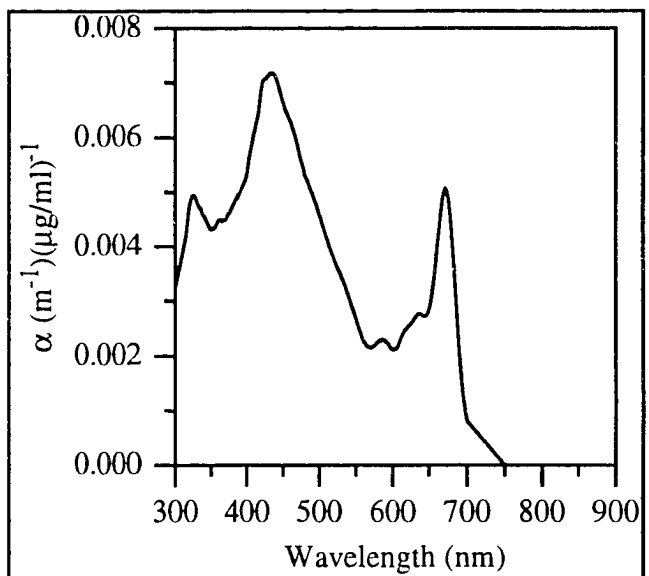

Figure 1.1. Specific absorption measured[27] from algae taken from Antarctic congelation ice.

Contaminants in sea ice can drastically change the spectral shape and magnitude of light extinction. There have been a large number of studies of the relation between light in sea ice and the biology in and under the ice. The absorption spectra of sea ice algae have an ultraviolet peak at 330 nm, a strong, wide peak at 430 nm, a minimum in the 580 - 620 nm band, and a lesser peak at 680 nm[6,26,27]. Figure 1.1 is the specific absorption curve measured from algae colonies taken from Antarctic congelation ice. The amount of algae present in ice is commonly measured in terms of the chlorophyll concentration. The term "specific absorption" refers to the light absorption by enough algae to yield 1 μg of chlorophyll per ml of ice. An algae bloom in McMurdo Sound has been observed[7] to double the extinction of the fast ice. Also, the shape of the spectral absorption by algae has been observed to change in response to changes in the color of the illuminating radiation[9]. Early in the growth season the absorption by algae in McMurdo Sound sea ice had the expected absorption at the blue 430 nm peak and the yellow 680 nm peak. After a bloom, the increased algae in the congelation ice reduced the amount of blue light reaching the

bottom platelet ice. The algae in the bottom platelet layer still had the same absorption peaks, but it absorbed light more strongly in the wavelength range 450 to 600 nm than the populations in the congelation ice above. Another interesting behavior of ocean-sea ice biology is the ability of some algae to adapt to increases in the ratio of ultraviolet B (280 - 320 nm) to photosynthetically active region (PAR) radiation[9,16,5].

1.3 Models of Sea Ice Optical Property

Most optical models of sea ice use measured data of extinction and scattering, and commonly calculate the top surface albedo, internal absorption, and light transmitted out of the bottom. Different measured extinction and scattering values are used in the models according to the ice type, age, and state of growth or decay.

The thermodynamics of sea ice was modeled by Maykut and Untersteiner[2] using Beer's law to approximate the energy given to the interior of the ice by solar radiation.

Grenfell[1] used the approach of applying measured extinction in a two-stream model to study the energy budget of ice-covered polar oceans. The backscattering coefficient was calculated from the ice volume reflectivity to deal with multiple scattering. His results were the albedo, transmission, and net spectral irradiance for spring and summer sea ice. This model verified that Beer's law is only an approximation in materials where multiple scattering of light is strong. The modeled transmitted irradiance at 650 nm is larger than Beer's law by a factor of 1.42 for 0.05 m thick blue ice, and 1.34 for a very optically thick ice layer.

A two-stream model by Perovich[28] used similar measured data of extinction in sea ice, plus measurements of absorption in pure bubble-free ice. The focus of these calculations was to examine the effects of variable sea ice thickness over an ice sheet, as well as growth and decay changes in the ice with time. The results showed the change in reflected and transmitted spectral irradiance for nonuniform ice in Mould Bay, Canada over several months in the spring.

Models of the relation between light in sea ice and sea ice biology also use the same method of applying measured extinction spectra. An example is a study by Arrigo et al.[8] to account for spectral changes in the light in and under an ice layer during production of biogenic material.

There are two more recent radiative transfer models that calculate the optical properties of sea ice. A four-stream model by Grenfell[3] and a multi-stream, coupled atmosphere, sea-ice, ocean model by Jin et al.[4] used ice temperature, salinity and bulk ice density to calculate the optical scattering properties that affect light propagation in the ice. Relations found by Cox and Weeks[29] are used to find the volume fraction of brine and gas in the ice. Grenfell[25] related these volumes to measured scattering phase functions. Jin et al. used an approximation of a power law size distribution of spherical bubbles and brine pockets and performed Mie calculations to get the scattering phase functions. Both models used absorption measurements of pure bubble-free ice and the contaminants of interest.

1.4 Purpose of Project.

The previous measurements and models described above give a good description of observed sea ice. Most of the work done to date has been performed on Arctic sea ice, covered wavelengths longer than 400 nm, and most measurements were taken above and below the ice. The purpose of this project was to expand the measurements of downward irradiance in sea ice into the ultraviolet, and to take the measurements at several depths in Antarctic sea ice.

The general plan was to find a way to collect light from inside an ice floe, obtain a spectrometer to fit the measurement method, and get depth profiles of spectral irradiance from several ice types in different states of growth and decay. The irradiance extinction in the ice and Equation 1.11 can be used to estimate the absorption and scattering effects.

The adopted measurement method was to drill a small hole through the ice and insert a light collector. The size of a high resolution spectrometer would require a large disturbance in the ice, so a fiber optic cable was used to carry the light from a small collector to the

spectrometer. An existing 0.5 m Ebert-Fastie spectrometer was modified to accept light from the light guide and to allow computer control and data acquisition. The usable wavelength range covered the ultraviolet A (UVA, 320 - 400 nm), visible (400 - 700 nm) and near infrared (NIR, 700 - 900 nm) in the solar spectrum. The method used could be applied to measurements in the UVB (280 - 320 nm).

1.5 Project History

During the 1990 - 1991 academic year the spectrometer was modified for field measurements. The 1980 vintage electronics were replaced to allow computer control and data acquisition. The light guide purchased was a quartz fiber optic bundle. A diffuser cavity was made to couple the cable to the spectrometer entrance slit. The final step of the prototype instrument was to mount it in a light-tight, rugged box. This would prevent light leakage problems and keep the system self-contained in one shippable package.

In August 1991 the system was taken to the Taku Glacier near Juneau, Alaska for a field test. A series of snow optics measurements was taken in wet summer snow. The snow optics measurements are described in chapter 3.

The snow optics measurements suggested several changes, which were done during the next year. The primary changes were construction of the ice light collector, purchase of a new photomultiplier tube (PMT) and construction of parts to control the temperature, humidity, and electric field around the PMT. There were also major changes made to the control and acquisition software.

Measurements in summer Antarctic sea ice were done on a cruise of the ice breaker, United States Coast Guard Polar Star during December 1992 and January 1993. This measurement program is the subject of Chapter 4.

The next round of instrument improvements was to construct a filter wheel and associated entrance optics. The filter wheel allowed removal of the second order grating diffraction from the longer wavelengths. A more important purpose was to allow simultaneous

measurements of downward sky irradiance with a second light guide along with the downward ice irradiance. The previous cruise revealed how important it is to account for the fast changes in sky conditions. Also the spectrometer case was modified to allow changing the grating so that better UVA data could be obtained. Chapter 2 contains a complete description of the instrument and light collectors.

The final field trip was part of the August-September 1993 cruise of the ice reinforced research vessel N. Palmer through winter sea ice. Chapter 5 discusses this final set of measurements, and Chapter 6 covers the overall conclusions of the project.

2. Spectrometer Design for Measuring Light in Sea Ice

As stated in chapter 1, the measurement of the optical properties of sea ice has previously involved placing an entire instrument or a light detector in or under an ice floe[7,23,22,24]. Another technique[19,20] is to measure the light lost from a collimated beam passed through an ice sample in a laboratory setting. There are some methods that measure light at several depths in ice or snow, but they commonly involve drilling horizontal holes in the wall of a pit[17,16,34].

The instrument described in this chapter is designed to take in- situ measurements of downward travelling light in and under sea ice. It is an expansion of the instrument made by Roulett et al.[7]. The primary differences of this system, compared to previous systems, are that the light collectors are separate from the spectrometer and the usable spectral range is from 300 to 900 nm. One of the collectors gathers downward traveling light from inside an ice layer by being inserted into a vertical 5 cm diameter hole, and the other gathers downward flux from the sky. The disturbance of the radiation field by the hole in the ice is addressed in section 2.5. The instrument is best described in terms of three primary systems: optics, instrument control and signal processing. Some example measurements are presented after the description of the instrument.

2.2 Optics

Figure 2.4 is a diagram of the instrument optics as used in an ice floe. The instrument optics are described in four parts: Ice and sky light collectors (A and B in Figure 2.4), entrance optics (C, D, and E), spectrometer optics (F) and exit optics (G, H, and I). Figures 2.1, 2.2, and 2.3 are photographs of the spectrometer, ice light collector and sky flux collector respectively.

2.2.1 Light Collectors

The ice light collector is a Lambertian reflector in a quartz tube (Figure 2.5). The reflector (A in Figure 2.5) is made of Spectralon[30]. This is a plastic material with a diffuse

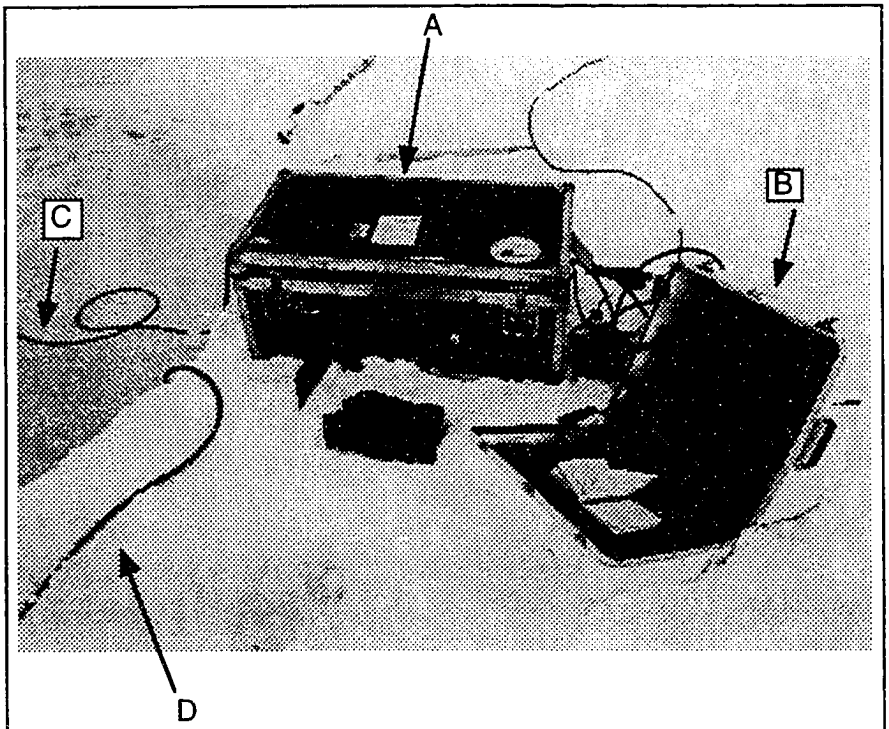

Figure 2.1. Photograph of the spectrometer in its case and the main computer in the box to the lower right.
A = spectrometer in its case
B = main computer in protective shelter
C = light guide from ice light collector
D = light guide from sky flux collector

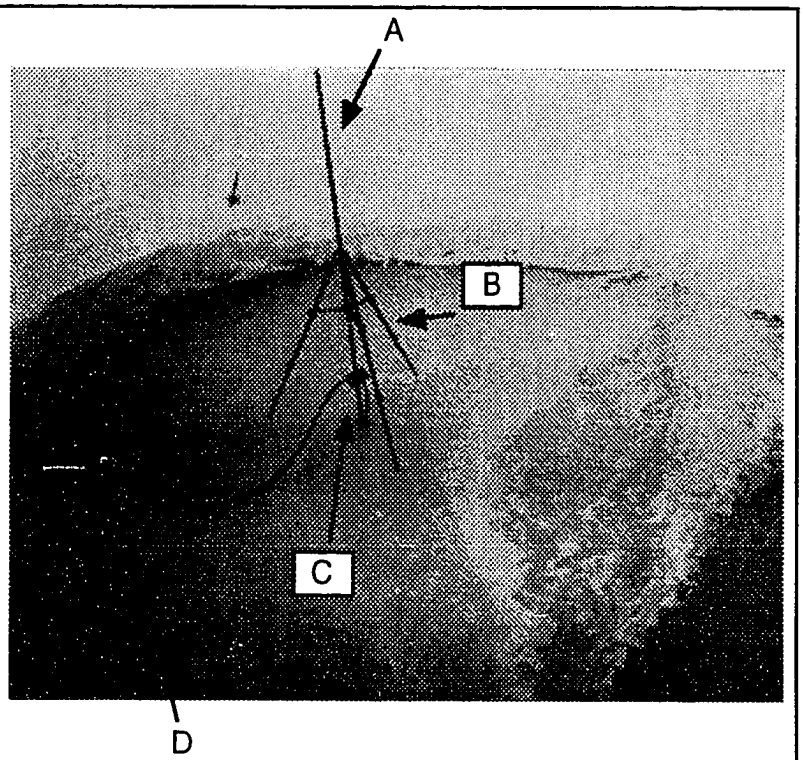

Figure 2.2. Photograph of the ice light collector support pipe and tripod on an area of ice cleared of snow. Note the black foam plug for the hole has been slid up the support pipe for the photograph.
A = support pipe
B = tripod
C = black foam plug for the ice hole
D = light guide

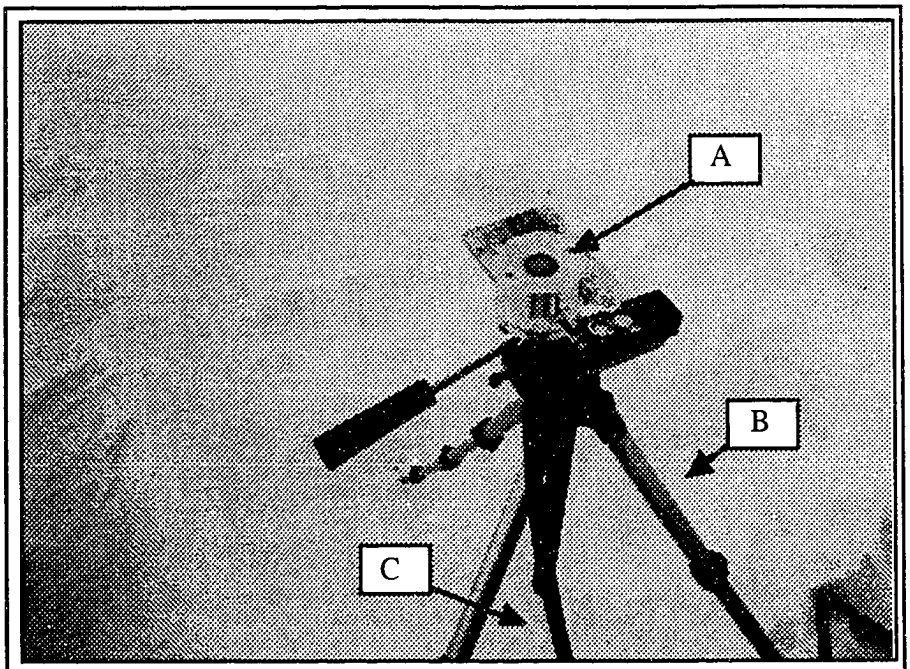

Figure 2.3. Photograph of the sky flux collector and tripod on an ice floe.
A = sky flux collector
B = tripod
C = light guide

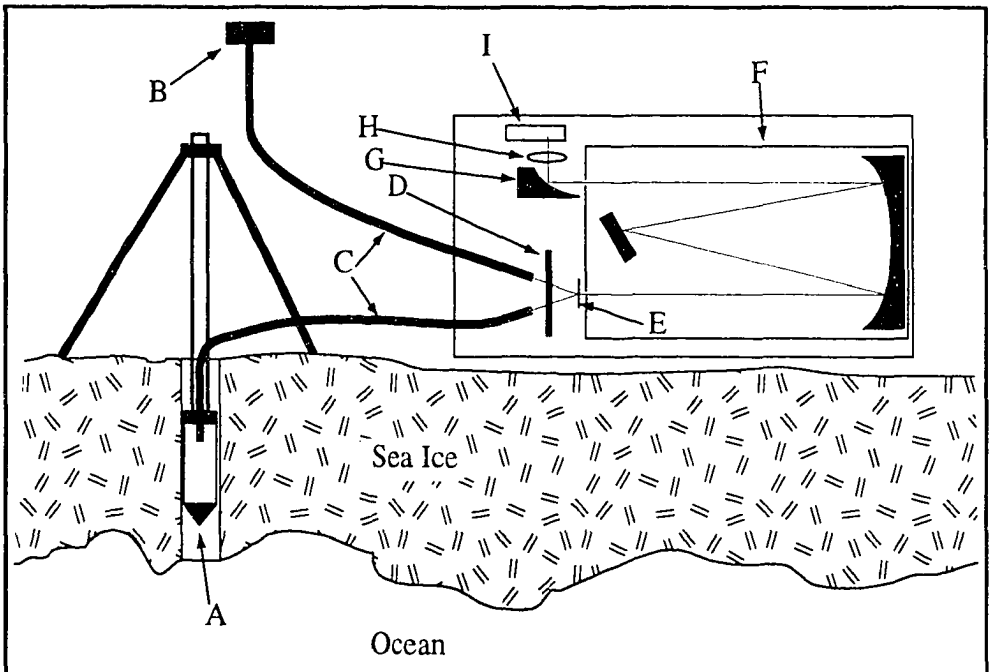

Figure 2.4. Diagram of optical arrangement for measurements of downward irradiance from the sky and from within sea ice where:

A = ice light collector	F = Ebert spectrometer
B = sky flux collector	G = parabolic mirror
C = light guides	H = quartz lens
D = filter wheel	I = photomultiplier tube.
E = ground quartz diffuser	

reflectivity greater than 0.98 between wavelengths of 300 nm to 1000 nm when properly prepared. The reflector sits facing up in an aluminum base at the bottom of the quartz tube (B). At the top of the quartz tube is a water tight mount (C) for the light guide (D) and support pole (E). The top piece of the collector also blocks light that is guided down the hole in the ice. The outside diameter of the ice light collector is 4.52 cm, the vertical distance from the light guide entrance to the reflector surface is 11.5 cm and the diameter of the reflector area in view of the cable is 3.66 cm.

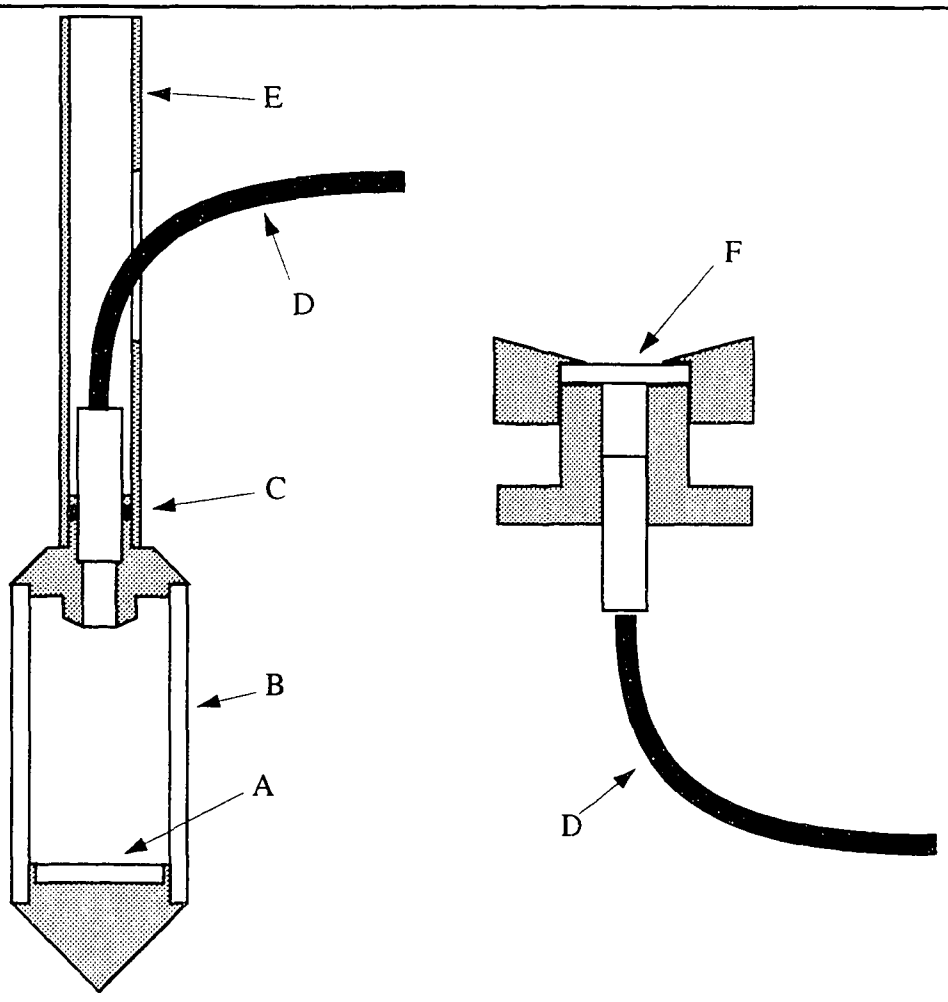

Ice Light Collector Sky Flux collector

Figure 2.5. Cut–away views of the ice light collector and downward sky flux collector, where

A = Lambertian reflector
B = quartz tube
C = watertight mount for optic cable and support pipe
D = optic cables
E = support pipe
F = diffuser

Light traveling downward through the ice is diffusely reflected from the reflector. The field of view of the fiber optic cable is limited so that the cable only sees the Spectralon reflector.

The inside of the top of the collector is painted black.

The sky light collector (Figure 2.5) is a Teflon transmission diffuser (F) in the field of view of another quartz fiber optic light guide (D). The diffuser is 6 mm thick to attenuate the downward sky radiation to levels comparable to intensities collected in 1 m of ice. This diffuser can be replaced with a 1.5 mm thick piece of Teflon when comparison to small light levels is not necessary, such as measuring snow albedo.

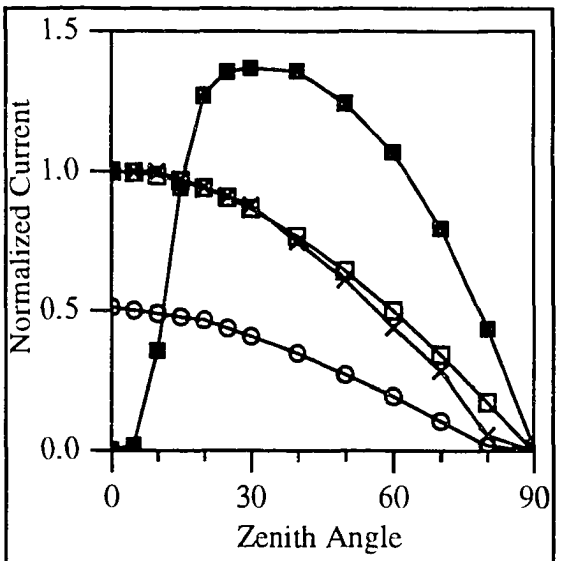

Figure 2.6. Angular response of collectors normalized to the data point of θ=0° for the sky collector with the 1.5 mm thick diffuser where:

□ = cos(θ) for comparison

X = sky light collector with 1.5 mm thick diffuser

O = sky light collector with 6 mm thick diffuser

■ = ice light collector

Figure 2.6 shows the normalized angular response of the two light collectors. A cosine curve is included for comparison. The response curves were measured by placing a 1000 W lamp at 5.2 m from the collector surface and integrating the signal from 580 nm to 670 nm, at several incidence angles between 0^0 and 90^0. It is important to note that the ice light collector response in Figure 2.6 was measured with the collector in air. When the collector is placed in water with the reflector facing straight up, the light travels from the sea water (n = 1.33) into synthetic fused silica (n = 1.46) and then into the air (n = 1) inside the collector volume. The result is that light travelling in angles less than 45° from a vertical axis is reflected back into the water.

Several liquids were tested to fill the inside of the collector. The fluid needed to have an

index of refraction that was similar or slightly greater than for sea water, must not form solids at cold temperatures, and it must be compatible with Spectralon and the adhesives used in the collector and optic cable. A fluid was not found that would match these requirements. For that reason the ice light collector was filled with air.

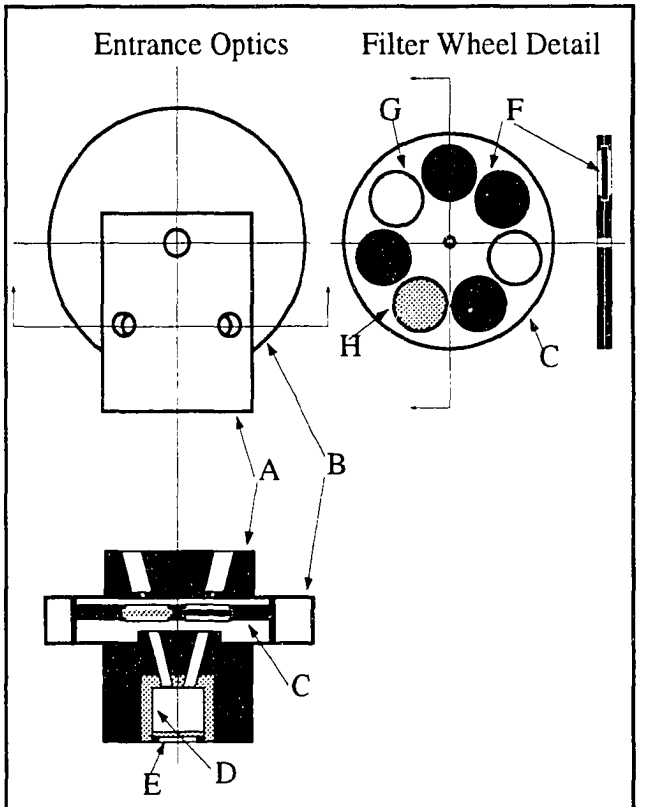

Figure 2.7. Entrance optics and filter wheel detail. The entrance optics cut-away view is in the plane of the optical axis to show the position of the filter wheel and optical paths.
A = optic cable mounts
B = filter wheel housing
C = filter wheel
D = Spectralon walls of diffusing chamber
E = ground quartz diffuser plate that illuminates the spectrometer entrance slit
F = black opaque disk
G = open filter hole
H = 495 nm longwave pass filter

2.2.2 Entrance Optics

The fiber optic light guides were made with multimode, plastic-clad synthetic fused silica fibers with a 210 μm core diameter. The field of view of the fibers is 12°. One of the cables was 5 m long with 117 fibers in the bundle. The spectral range of transmission for this cable was 300 - 1350 nm. The other cable was 7.5 m long with 235 fibers. Damage to the fibers in this cable degraded the transmission for wavelengths shorter than 400 nm to an unusable level.

The two optic cables carry light to the entrance optics (Figure 2.7). Light from the cables shine on a filter wheel (C). The wheel has 7 filter spaces. Aluminum disks painted black (F) fill four spaces, a filter (H) occupies one other

space and the remaining two spaces are open (G). The filter passes wavelengths longer than 495 nm with a transmission of 86%. The pair of disks in neighboring spaces block both cables to allow the measurement of the system dark signal. The remainder of the disks is arranged to block one cable while passing light from the other. The synchronization of signal sampling with the filter wheel is described in sections 2.3.2 and 2.4.3. After the light passes through the filter wheel, it enters the diffusing chamber (D). Light scattered by the diffuser (E) illuminates the spectrometer entrance slit.

2.2.3 Spectrometer Optics

The spectrometer (Figure 2.4) was a 0.5 m Ebert-Fastie design[31,32] purchased from Jarrell-Ash Scientific[33]. The entrance and exit slits are curved and adjustable from 5 μm to 3 mm. The ruled area of the grating is 52 by 52 mm. The grating mount holds the grating with a spring clip and a three-point standoff so that the grating can be easily changed without the need to realign the spectrometer optics. The grating is rotated by a precision screw and sine bar which are described in section 2.3. It is possible to resolve the 313.16 - 313.18 nm Mercury doublet in first order diffraction with a 1180 groove/mm grating, though a resolution of 1 to 6 nm was used in measurements of light in sea ice.

2.2.4 Exit Optics

The light detector is a photomultiplier (PMT) tube with a photocathode made of GaAs. This PMT was chosen because it has a wide, flat spectral response (200 - 900 nm). Monochromatic light exiting the spectrometer is focused on the PMT (I in figure 2.4) by an off-axis parabolic mirror (G) and a quartz lens (H). The focusing optics are necessary to compress the 2 cm long slit image onto the 1.2 cm PMT window. A three-axis positioner connects the PMT housing to the mirror housing so that the PMT can be aligned under the reduced slit image.

2.3 Instrument Control

Figure 2.8 is a block diagram of the spectrometer control parts. The parts that are controlled are the grating, the filter wheel and the PMT temperature and surrounding humidity. The grating and filter wheel are driven by motors with position encoders. An MCX-02 computer counts the quadrature pulses from the encoders and uses programmable transfer functions to calculate the voltage for each motor and supplies those voltages. The spectrometer wavelength is tracked with a separate encoder to avoid wavelength errors due to slack in the grating drive gears. The main computer (A) sends motor velocity and acceleration commands to the MCX-02 over an RS232 port. The main computer is an 80386 portable with a modified Keithly DAS8 sampling board.

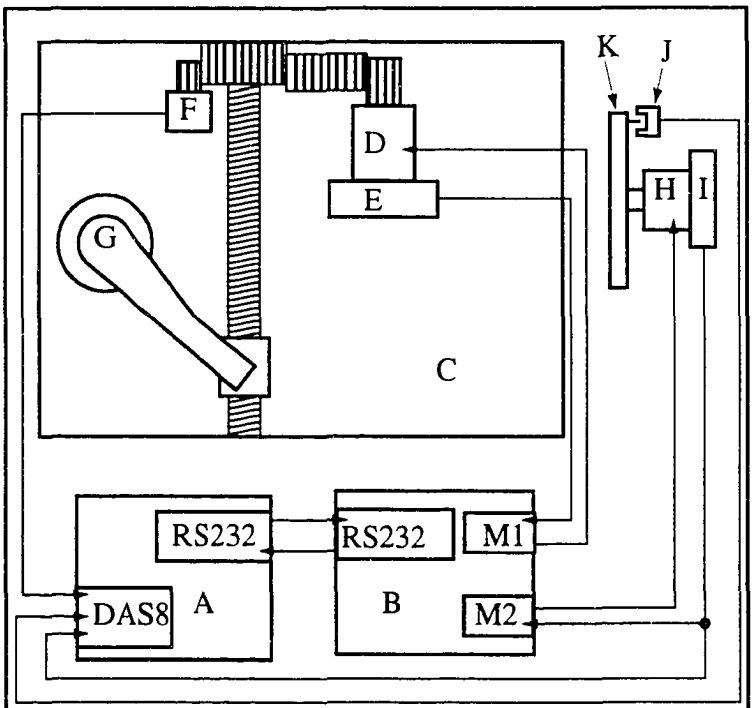

Figure 2.8. Spectrometer control diagram. The arrows indicate the receiving end of the signal paths.
A =main computer with DAS8 sampling board
B = motor control computer
C = spectrometer gear housing
D = grating drive motor
E = grating motor position encoder
F = grating position encoder
G = grating mount bearing and sine bar
H = filter wheel motor
I = filter wheel position encoder
J = filter wheel home position photo-interrupt
K = filter wheel
RS232 = communications ports
M1 and M2 = motor control integrated circuits

2.3.1 Grating Position

The grating mount (G in Figure 2.8) is rotated by a precision screw and sine bar. A motor and encoder (D and E) drive the screw via a few gears. The sine bar approximates a sine function so that constant motor velocity gives a constant change in wavelength at the exit slit[33]. A separate encoder (F) is driven directly from the screw so that the wavelength can be precisely tracked. A logic circuit (not shown) produces a hardware interrupt pulse that signals the parent computer to update the wavelength variable in the sampling software. This arrangement tracks the wavelength position of an 1180 groove/mm grating to 0.01 ± 0.005 nm.

2.3.2 Filter Wheel Control

The filter wheel motor (H in Figure 2.8) is controlled by the MCX-02 the same way as the grating drive motor. The wheel rotates at 1500 rpm. The parent computer knows the position of the wheel by using a counter on the DAS8 card to count the quadrature pulses from the motor encoder (I). A photo-interrupt on the wheel (J) resets the counter every revolution. The acquisition software only allows sampling when the counter matches preprogrammed values for when a filter, hole or dark level is in view.

2.3.3 Photomultiplier Tube Environment

The response and dark noise of the PMT are strongly dependent on the temperature. Peltier heat pumps, ethylene glycol coolant and a radiator are used to keep the PMT housing temperature at -10 °C. A small flow of desiccated air is pumped through the housing. It enters in the base near the heat pumps where it is cooled, flows into contact with the PMT and exits through a port that blows on the outside of the quartz lens to prevent frost buildup.

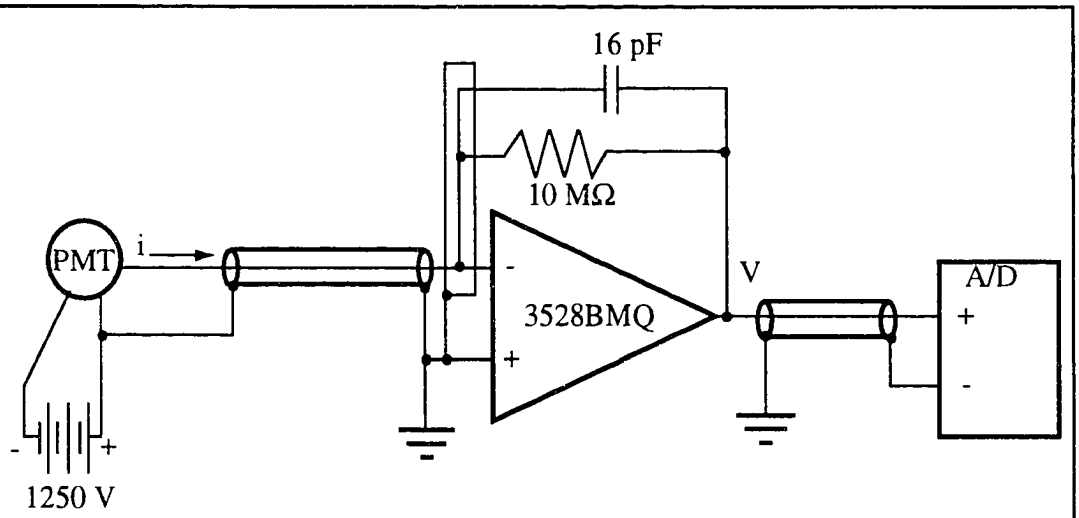

Figure 2.9. Signal path schematic diagram. Refer to equation 2.1 for a description of the PMT output current (i) and amplified voltage (V).
PMT = photomultiplier tube
A/D = programmable amplifier and analog to digital converter in the main computer

2.4 Signal Processing

The PMT produces a current proportional to the number of photons striking the cathode. A high gain amplifier converts the nanoampere-sized current to a voltage that can be easily digitized. The parent computer samples the voltage and stores the numbers according to the viewed wavelength and optic cable and filter wheel position in view. A simplified schematic diagram of the signal path is in Figure 2.9.

2.4.1 Photomultiplier Tube

The PMT is a model R636 made by Hamamatsu. It has a GaAs photocathode activated in Cesium. This gives it a very flat response from 400 to 800 nm and a usable range of 200-900 nm. It is operated at 1250 volts. The dark noise was measured at about 1 nA with a PMT temperature of 25 °C and about 0.04 nA at -10 °C. The maximum current output is 1000 nA. This gives a usable dynamic range of 4 orders of magnitude.

2.4.2 Amplifier

The amplifier is a single chip operational amplifier 3528BMQ made by Burr Brown (Figure 2.9). The input bias current is less than 0.0002 nA which is negligible compared to the 0.04 nA PMT dark noise. It is configured as an inverting current to voltage amplifier. Neglecting the input bias current, the current to voltage gain relation is given by

$$V = \frac{-iR}{1+j2\pi fRC} = \frac{-i10^{7}}{1+jf10^{-3}}$$

where

V = voltage sampled by main computer

i = PMT anode current

$j = \sqrt{-1}$

f = signal frequency in Hz

R = 10MΩ

C = 16 pF.

Equation 2.1

The resistor is a metal film type which is stable with changes in temperature. The DC gain is 10 V per 1000 nA and the frequency bandwidth is 0 to 1.1 KHz with a phase shift of 0 to -63° respectively.

All connections to the negative input of the amplifier are insulated with Teflon and surrounded by a ground plane on the circuit board to reduce current leakage out of the PMT current (i in Figure 2.9 and Equation 2.1).

2.4.3 Digital Sampling

The output voltage from the amplifier is sampled on the DAS8 board in the parent computer. The A/D converter has a 12 bit resolution. The programmable gain of the DAS8 board allows PMT current measurement better than 1% over the range of 0.049 to 1000 nA.

The parts of the software that needed to be fast were written in 80386 Assembly language. The remainder was written in C. The sample wavelength resolution can be set between 0.01 and 655.35 nm. The scan speed can be set to a value in the range of 3.7×10^{-4} to 9.2 nm/s.

Sums and sample counts are maintained for the dark signal and each of the six filter wheel - optic cable combinations. When the wavelength counter variable reaches the end of the sample wavelength resolution, the sum and count values are stored in memory along with the current wavelength and a new group of sums and counts are started for the next resolution bin. After the scan is complete, the data are stored in a disk file with some header information on the instrument parameters.

2.5 Measurements and Data Processing

The examples of data presented here were taken on 10 September 1993 at 76.10° S, 167.8° W which is north of Thurston Island, Antarctica. These measurements were part of a two-month cruise of the Nathanial B. Palmer research vessel. The ice here was 80 cm thick with a 30 cm snow cover. It was first year ice that looked greenish-grey. The ice temperature ranged from -6.7 °C to -1.3 °C and the salinity ranged from 10.5‰ to 3.2‰.

After the equipment was moved from the ship onto the ice, the spectrometer was turned on to allow the PMT response to stabilize. An area of ice 5 m in diameter was cleared of snow since snow cover would attenuate the near UV wavelength light before reaching the ice. Based on scattering measurements done by Trodahl et al.[22], the snow edge should reduce the light at the bottom of the center of the cleared area by about 1%. They put a lamp on the

top of a 1.5 m thick first year ice layer. The light emerging out the bottom at 1 m away horizontally was a factor of 10 less than that emerging from the ice directly under the lamp.

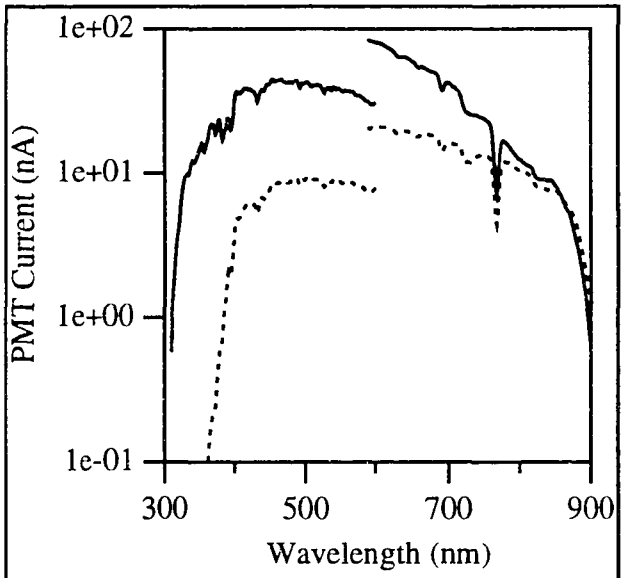

Figure 2.10a. PMT current from ice light and sky flux measurement. The solid curve is from the ice light collector at 0.1 m in a 0.85 m thick, greenish ice floe. The dashed lines are from the sky flux measured concurrently with the solid curves. The 2360 groove/mm grating was used for wavelengths shorter than 600 nm, and the 1180 groove/mm grating was used for longer wavelengths. There is a discontinuity because the gratings have different spectral reflection efficiencies.

A vertical, 5 cm diameter hole was drilled through the ice near the center of the cleared area. A black foam plug was inserted into the top of the hole around the light collector support pipe to prevent the sky radiation from entering the hole. There is also the question of light emitted from the brighter, top layers being guided down the hole to the collector. Light impinging on the wall of the hole would not be reflected by the water-ice interface, but would be scattered by the inclusions in the ice. There would be very little reflection at the interface since the indices of refraction of sea ice (1.34) and ocean water (1.33) are very similar. Scattering by inclusions would diffusely reflect a small part of the impinging light down to lower layers. To enter the collector, the light in the hole must pass through the gap between the collector and the wall of the hole. The effect would be an increase in measured light at the lower depths, and reduced values of extinction.

Once the instrument and light collectors were set up as represented in Figure 2.4, spectra were collected at 10 cm depth intervals in the ice. Two gratings were used to cover the wavelength range of 320 - 900 nm. A 2360 groove/mm grating blazed for 260 nm peak

reflection was used for wavelengths of 280 - 600 nm, and an 1180 groove/mm blazed for 520 nm peak reflection was used for 580 - 900 nm.

The downward light spectra were recorded with sampled a signal sum and sample count every 1 nm. The spectrometer entrance and exit slits were set at 2 mm to give a measured resolution of 2 nm with the 2360 groove/mm grating and 4 nm with the 1180 groove/mm grating. The scan speed was adjusted to obtain 800 to 1500 PMT current samples per nm in wavelength depending on the light level in the ice.

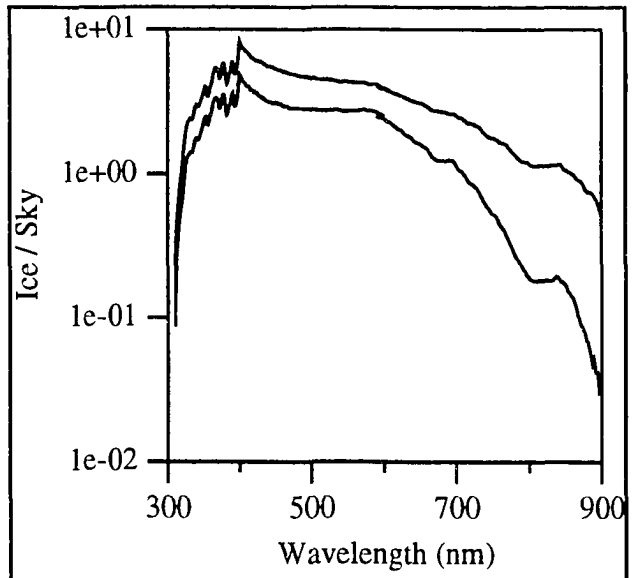

Figure 2.10b. Ice light spectra divided by their corresponding sky flux spectra from the same measurements used in Figure 2.10a. The top curve was taken at 0.1 m depth and the bottom curve is from 0.3 m. The spectra for wavelengths shorter than 400 nm were scaled to the 400 nm point instead of being normalized.

Figure 2.10a displays the raw PMT current signals with the background levels subtracted for the ice light and sky flux spectra collected at 0.1 and 0.3 m. The solid curves are from the ice light collector, and the dotted curves are from the sky flux collector. The data are in units of nanoamperes from the PMT. The background signal levels were the averages of PMT current between 280 and 290 nm (not shown). The background for each spectrum is different due to a small amount of light that is scattered from surfaces inside the spectrometer allowing some "white" light to reach the PMT. The discontinuity at 600 nm is because the two gratings have a different spectral reflection efficiency. The sky light curve is lower then the ice light curve because the thick sky flux diffuser was used. These curves contain effects of the optic cable and instrument response, which are wavelength dependent. Also, note the steep drop in the sky flux signal for wavelengths shorter than 400 nm from the optic cable described earlier.

Figure 2.10b displays the ice light normalized by the sky flux. The curves are calculated from the data shown in Figure 2.10a. The ice light data are scaled by the sky flux value at 400 nm due to the poor ultraviolet transmission of the optic cable used on that collector. The top curve is from the measurement at 0.1 m, and the bottom is from 0.3 m in the ice. The data with wavelengths longer than 600 nm had to be scaled to match the data in wavelengths shorter than 600 nm. The scale factors were 1.01 and 1.04 for the depths 0.1 m and 0.3 m respectively. Some discrepancy is expected since the ice light collector was positioned separately for sampling with the different gratings.

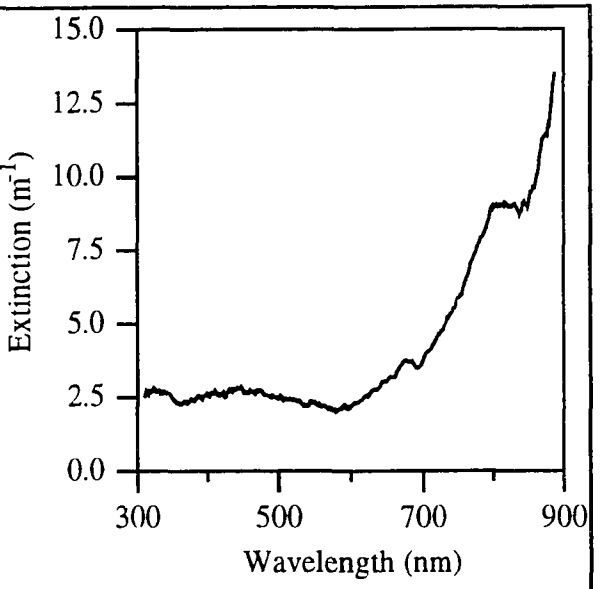

Figure 2.10c. Spectral extinction between the 0.1 m and 0.3 m depths calculated from the data in figure 2.10b. The small peaks at 330, 430, and 680 nm are due to the algae in the ice.

Figure 2.10c shows the extinction calculated from the data in Figure 2.10b. Note the chlorophyll absorption peaks at 330, 430 and 680 nm[7], as well as the ice absorption feature at 800 nm to 840 nm. The extinction of 2.5 m^{-1} in the range 320 nm to 600 nm agrees with first year sea ice[16] (1 m^{-1}) with increased absorption by biogenic material (Figure 1.1). The spectral structure and magnitude of this extinction curve are discussed in chapter 5.

The extinction values are comparable to flux extinction because sea ice is a highly scattering medium. The amount of scattering in clean sea ice at 600 nm can be estimated from Equation 1.12 with K = 1 m^{-1} for first year ice[16], α = 0.1 m^{-1} for absorption by ice[19], and a value for the fraction of backscattered light[25] of β = 35%. This gives a value for scattering of σ = 29 m^{-1}, or a skin depth of 3.5 cm where 63% (1-e^{-1}) of the light that

entered the top ice surface has been scattered at least once. This is the depth where the light entering the collector is approximately proportional to the downward radiant flux. This assumption would not work in material where there is little scattering such as water, because the radiation field is concentrated around the straight down direction by refraction at the air - water surface.

2.6 Measurement Uncertainties

The sources of uncertainty in the light measurements are (1) the electronics and digital sampling, (2) PMT stability, (3) how well the light entering the collector represents the downward flux in the ice, and (4) the difference between measured downward sky flux and the true light source that illuminates the depth in the ice where the ice light collector is positioned.

A 7 W halogen lamp was used to test the PMT, electronics, and digital sampling. Figure 2.11a shows the irradiance spectra from four distances between the lamp and optic cable. The end of the optic cable was shielded with a black tube to limit the field of view to 10°, and then positioned facing the lamp. The wall behind the lamp was covered with a black velvet cloth. Spectra were taken with distances (d)

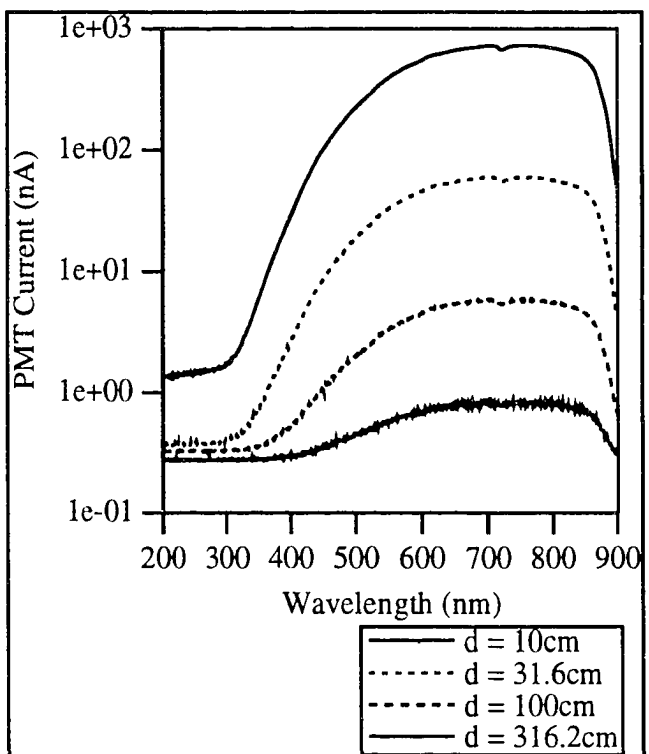

Figure 2.11a. Spectra measured from a 7 W halogen lamp at distances (d) of 10, 31.6, 100, and 316.2 cm from the end of optic cable. The background signal level can be seen in the wavelength range of 200 - 300 nm. The background signal is the sum of the PMT dark noise, stray light and amplifier offset voltage.

between the lamp and cable end of d = 10, 31.6, 100, and 312.6 cm. These spacings give relative irradiance values at the cable end of 1, 0.1, 0.01, and 0.001. No corrections have been applied to remove the background signal level or the wavelength dependant instrument response in Figure 2.11a. The background signal level (BG) is the sum of the PMT dark current, internal stray light, and the amplifier offset voltage. The value of BG for each spectrum in Figure 2.11a was calculated from the average of the points between 200 and 250 nm. The fiber optic cable does not transmit light in that wavelength band. The standard deviation of the points between 200 and 250 nm is a measure of the noise level in data.

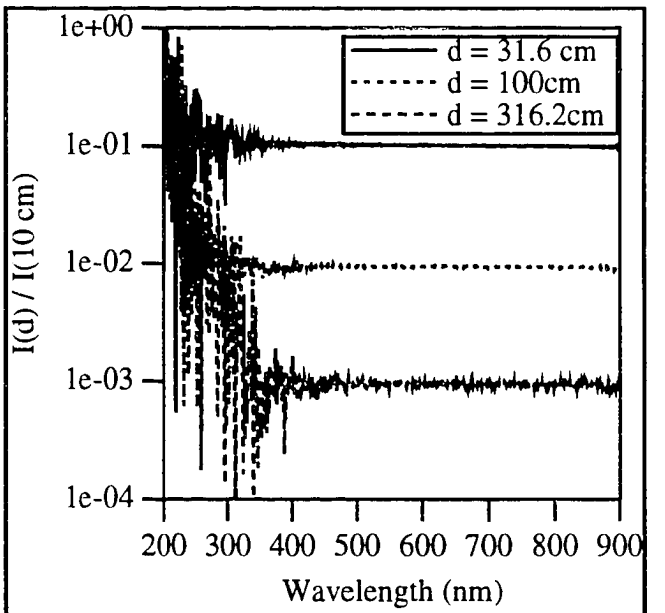

Figure 2.11b. Spectra from Figure 2.11a normalized by the d = 10 cm curve. The distance between the lamp and cable end were 10, 31.6, 100, and 316.2 cm to give relative irradiance values at the cable end of 1, 0.1, 0.01, and 0.001.

Figure 2.11b shows the normalized spectra from Figure 2.11a. The BG current values were subtracted from the four curves and then the d = 31.6, 100 and 316.2 cm curves were normalized by the d = 10 cm curve. The three normalized current ratio spectra have values of 0.1, 0.01, and 0.001 as expected since irradiance from a point source is proportional to d^{-2}. The ratios in Figure 2.11b are flat where the signal to noise ratio (s/n) is greater than 20. The s/n values pass through 20 at the wavelengths 300, 320, 345, and 420 nm for the curves of d = 10, 31.6, 100, and 316.2 cm in Figure 2.11a.

Figures 2.11a and b show that for s/n greater than 20, the PMT, signal processing and digital sampling have a linear response to the light entering the cable end. Data with s/n less than 50 were not included in this thesis. The flat regions in Figure 2.11b can give a

measure of the fractional random uncertainty of the instrument. The fractional uncertainty (δI/I), at a 95% confidence level, was calculated by

$$\frac{\delta I}{I} = \frac{2s}{m}$$

where

$\frac{\delta I}{I}$ = fractional uncertainty

s = standard deveation

m = mean.

Equation 2.2

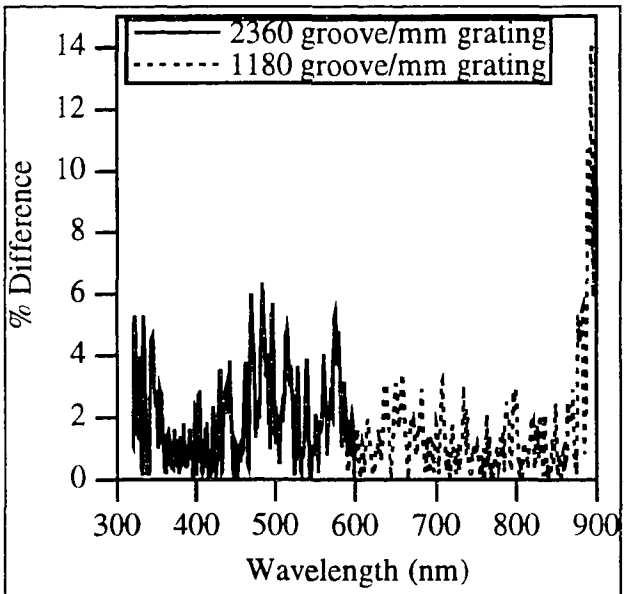

Figure 2.12. Absolute value of the percent difference between a pair of spectra taken with each grating with the ice light collector at 20 cm depth in an ice floe.

The points used to find s and m are from the curves in Figure 2.11b in the wavelength range of 500 to 900 nm. The values of δI/I are 0.02, 0.02, and 0.10 for the top, middle, and bottom curves respectively. This means the spectrometer system measures light intensity within 2% except for conditions requiring the highest gain setting (d=316.2 cm in Figure 2.11b) which has an uncertainty of 10%. These uncertainties apply when normalizing spectra and do not relate to absolute units of radiant energy since absolute calibration of the instrument was not performed.

To test how well the spectrometer measures light in ice, two spectra on each grating were taken with the ice light collector at 20 cm depth in an ice floe. The collector was not disturbed between the measurements. Figure 2.12 shows the absolute value of the percent difference between the two spectra for each grating. These measurements contain the 2% random instrument uncertainty described above, plus the variation between the light received by the sky flux collector and the light entering the ice that illuminates the layer where the ice light collector was placed. The average for all points in Figure 2.12 is 1.8, and the standard deviation is 1.7. This gives an upper limit of the random uncertainty of

5.2% calculated from the mean plus two standard deviations. The difference rises to 14% at 895 nm due to the reduced near infrared light levels in the ice.

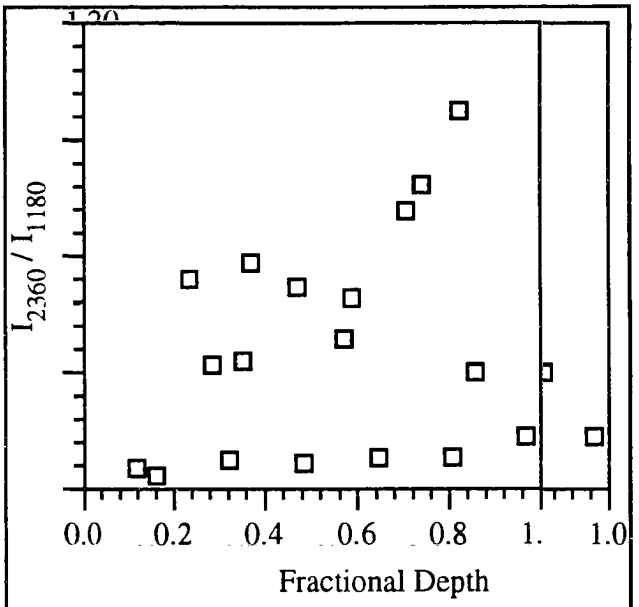

Figure 2.13. Scale factors used to match the 1180 groove/mm grating spectra to the 2360 groove/mm spectra for the data in Chapter 5.

Another indication of uncertainty in the measurements can be seen in the range of scale factor values used to match the 1180 groove/mm grating spectra to their corresponding 2360 groove/mm grating spectra. These factors were used to match spectra of R from Equation 5.1. A spectrum of R values is an ice light spectrum normalized by sky flux and by the spectrum taken at the top depth in the ice floe. Figure 2.13 is a scatter plot of all the scale factors from the data in Chapter 5. The depth in the ice for the scale factors is expressed as a fraction of the ice thickness to compare values from different ice floes. These points express the same uncertainties as Figure 2.12 plus the repeatability in placing the ice light collector at the same depth and changes in the distribution of ice chips and slush between the light collector and the wall of the hole in the ice. The scatter in the points shows there is no dependence of the scale factor on depth in the ice. The average of the scale factors is 1.06 with a standard deviation of 0.05. Also note that all the values are above one. Spectra taken with the 1180 groove/mm grating are about 5% smaller than those taken with the 2360 groove/mm grating. Figure 2.13 agrees with Figure 2.12 with a 5% random uncertainty.

The uncertainty in the normalized measured light levels (R) propagates to uncertainty in extinction according to

$$\delta K = \left(\left(\frac{\partial K}{\partial R_1} \delta R_1 \right)^2 + \left(\frac{\partial K}{\partial R_2} \delta R_2 \right)^2 + \left(\frac{\partial K}{\partial \Delta z} \delta \Delta z \right)^2 \right)^{1/2}$$

$$= \frac{1}{\Delta z} \left(\left(\frac{\delta R_1}{R_1} \right)^2 + \left(\frac{\delta R_2}{R_2} \right)^2 + \left(K \, \delta \Delta z \right)^2 \right)^{1/2}$$

where

$K = -\frac{1}{\Delta z} \ln \left(\frac{R_2}{R_1} \right)$ = extinction in the layer Δz

δK = uncertainty in extinction (K)

δR_1 = uncertainty in ice light (R) at depth z_1

δR_2 = uncertainty in ice light (R) at depth z_2

$\delta \Delta z$ = uncertainty in layer thickness ($\Delta z = z_2 - z_1$)

R = normalized ice light spectrum from Equation 5.1.

Equation 2.3

Figure 2.14 shows the extinction from Figure 2.10c with the upper and lower error limits from Equation 2.3. The solid line is the extinction curve, the dotted lines are the upper and lower error limits with $\delta R/R = 5\%$, and the long dashed curves are the error limits with $\delta R/R = 10\%$. The layer thickness was $\Delta z = 0.1$ m with an uncertainty of $\delta \Delta z = 0.007$ m. The percent error in the wavelength range of 320 - 600 nm is 29% for $\delta R/R = 5\%$, and 57% for $\delta R/R = 10\%$. The percent error in extinction drops to 10% and 15% at 850 nm for $\delta R/R = 5\%$ and 10% respectively.

2.7 Conclusions

The ice light collector allows in-situ measurement of light profiles in ice layers. It has an angular cosine response only for zenith angles between 45° and 90°. Measurements yield realistic extinction values at depths where multiple scatter has converted any direct beam

radiance to diffuse radiation. This is the case whenever the top surface is more than an optical depth of 0.5 from the top surface.

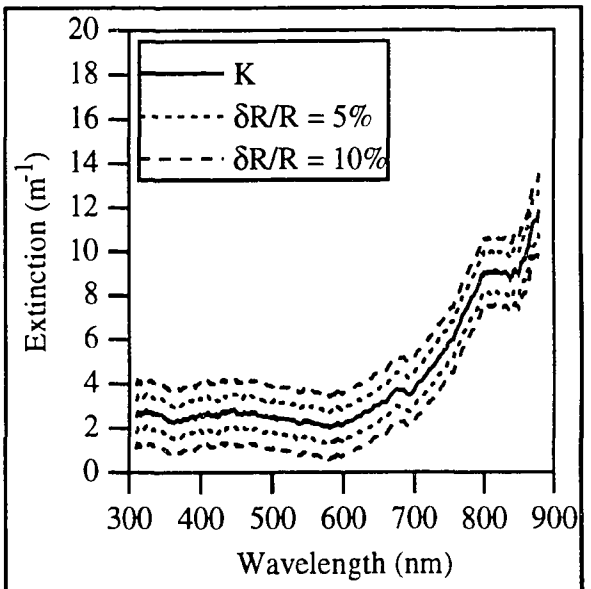

Figure 2.14. Extinction from Figure 2.10c (K) and extinction error limits for ice light uncertainties (δR/R) of 5% and 10%. The ice layer thickness was 0.1 m.

Further testing to find a compatible combination of Spectralon, adhesives, and a fluid with the correct properties could yield a cosine response for zenith angles between 20° and 95°.

Measuring radiant sky flux simultaneously with the downward light in the ice removes effects of changes in the downward sky flux. Separating the light collectors from the spectrometer via fiber optic light guides allows a high resolution spectrometer to be used. It also allows the coupling of a wide range of light collection schemes to the spectrometer for in-situ and laboratory settings. The dynamic range covers four orders of magnitude, and the usable wavelength range of the instrument is from 320 nm to 900 nm in the solar spectrum. The resolution can be adjusted from 0.03 nm to 6 nm with an 1180 groove/mm grating.

The instrument is capable of measuring the light entering the end of the fiber optic cable with a 2% uncertainty. There is an additional 3% uncertainty associated with collecting light from inside an ice floe and normalizing it to the downward sky flux. The uncertainty in the ice light spectra propagates to an extinction uncertainty (δK/K) of 29% for a 0.1 m thick ice layer. The value of δK/K is proportional to the inverse of the optical thickness ($[K\Delta z]^{-1}$).

3. Ultraviolet (A) and Short-Wave Radiation on the Juneau Icefield, Alaska [34]

3.1 Acknowledgment

This chapter is a manuscript that has been accepted for publication[34]. It is included because the measurements provided a field test of the instrumentation and methods for future studies in Antarctica. The authors are Timothy Quakenbush and Gerd Wendler. The field program and measurements were done by Mr. Quakenbush with many suggestions from Dr. Wendler. Mr. Quakenbush wrote 80% of this article, and Dr. Wendler wrote the other 20%. This study was supported by NSF Grant, DPP 90-17969. Dr. Maynard M. Miller, Director, Juneau Ice field Research Program under the aegis of the Foundation for Glacier and Environmental Research supported us generously. Further, the help of Carl Byers and the student intern Andrew Otto are gratefully acknowledged.

3.2 Abstract

Polar ozone depletion has lead to interest in ultraviolet light (UV) at the Earth's surface. High resolution spectral measurements were carried out on the Juneau Ice field in Southeast Alaska in the summer of 1991 to study the UV-A (320 - 400 nm) and short wavelength visible (400 - 600 nm) radiation field in and above a snow covered area. Radiative measurements of the sun, clear and cloudy sky and the reflectivity and extinction of a glacier snow pack were performed.

Clear sky measurements agree with a Rayleigh scattering atmosphere. Comparing direct solar radiation to diffuse radiation from cloudy skies indicates clouds scatter light evenly across the observed wavelengths with absorption by water drops increasing the extinction in the UV and yellow-red ranges.

The reflectivity of snow was highest in the blue (90%). It decreased to 78% at 350 nm, and to 88% at 600 nm. Its absolute values depend on the physical characteristics of the snow cover.

The extinction coefficient of UV in snow was higher than the mean of the short wavelength band of the visible spectrum. Values ranged from 10 m^{-1} at 330 nm, dropped to about 4 m^{-1} in the blue (480 nm), and climbed to 9 m^{-1} at 590 nm. Larger extinction values occur at longer wavelengths. This final point is probably the most interesting and has been made possible due to a quartz fiber optic light guide. It carries light from inside snow or ice to a spectrometer, making high resolution measurements in these media possible with minimal disturbance to the medium itself.

3.3 Introduction

In the classic paper by Farman et al.[35] a substantial decrease in ozone was observed in Antarctica based on observations by the British Antarctic Survey. Considerable work has been done toward understanding the polar ozone depletion process[36,37]. The reduction in the amount of stratospheric ozone is most prominent in high southern latitudes during austral spring. However, it also occurs to a lesser degree in the Arctic[37]. During the Arctic spring a large fraction of the polar regions is covered with snow.

Most of the ultra-violet light is absorbed by a small amount of ozone, equivalent to a layer 3 to 4 mm thick at standard atmospheric pressure. The small change in surface UV radiation could have a large effect on life since it is much more biologically active compared to the visible range of the solar spectrum.

A fair amount of work has been done on the radiative characteristics of snow and ice in the visible wavelength range, however little has been done for wavelengths shorter than 400 nm. During the summer of 1991 measurements were carried out on the reflectivity, transmittance and absorption of snow and ice on a glacier in Southern Alaska. Our measurements were performed in the UV-A and short wavelength end of the spectrum (320 to 600 nm). The signal to noise ratio of our measurements in the UV-B band (280 to 320 nm) was too small for the data to be useful, however, the methods described later are applicable in this region which is so important to life processes on Earth. Absorption by ozone is very strong in the UV-B band, and weak in the UV-A band.

Measurement of light extinction in snow has traditionally been difficult to perform. Before the advent of quality fiber optic light guides, the entire measuring instrument or detector was placed in a hole in the snow. This makes for a substantial disturbance of the snow pack. An alternative method was to cut out samples of snow or ice and analyze their absorption characteristics in a cold room, also leaving open the possibility of disturbances. In contrast to these older methods, the measurements presented here were taken *in situ* with a synthetic quartz fiber bundle and an Ebert-Fastie spectrometer. The spectrometer is capable of the very high resolution of 0.3 Å and the flexible cable allowed measurement of spectral intensity with minimal disturbance to the medium. A description of the instrument is in the next section.

3.4 Instrumentation

The spectrometer used in this field study was a scanning Ebert-Fastie design with a 0.5 m focal length mirror. The instrument was manufactured by Fisher Scientific Company[33]. Fastie[31,32] originally described this arrangement of optics. The instrument uses a single grating with a groove spacing of 1180 grooves/mm. The entrance and exit slits are curved, 20 mm long, and the width can be adjusted from 5 μm to 3 mm. A slit width of 50 μm was used for our measurements, giving an optical bandwidth of about 0.2 nm at the detector.

The primary innovation of the spectrometer is the use of a quartz optical fiber light guide. Light is fed to the entrance slit through the light guide and a diffuser. Figure 3.1 shows a drawing of the optics. The cable is 5 m long with a total cross section active area of 3.25 mm^2. It is made of a bundle of 25 μm core diameter synthetic quartz fibers. Both ends are terminated with stainless steel ferrules. The field of view of the cable end is 12°.
The diffuser is necessary to uniformly illuminate the entrance slit with the non-uniform cone of light emitted from the cable. It is a 3 cm hemispheric cavity machined from Spectralon, a very white reflective plastic. The open face of the hemisphere is covered by a Spectralon mask that covers areas not in view of the entrance slit's narrow field of view. Light from the cable enters through a 3.5 mm hole in the side of the hemisphere and is

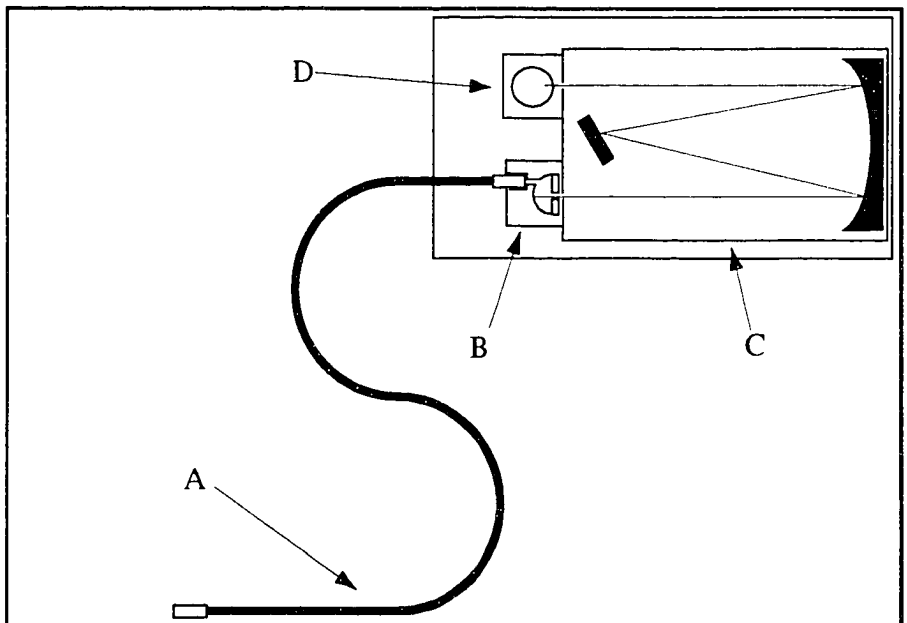

Figure 3.1. Schematic of the spectrometer optics.
A = synthetic fused silica fiber optic light guide
B = entrance light diffuser
C = Ebert spectrometer
D = photomultiplyer tube

diffusely reflected from the mask plate back into the chamber. The slit sees the diffusely illuminated area on the center of the hemisphere surface.

A system of optical encoders, grating drive motor, and a portable computer control and monitor the position of the grating which determines the wavelength of light that reaches the photomultiplier tube (PMT) detector. The wavelength scan rate is programmable from 0 to 550 nm/s with a tolerance of 1%. The computer tracks the wavelength of light entering the PMT over the range 200.00 to 900.00 nm with an accuracy of 0.01 nm.

The detector system is a 1P28 series photomultiplier tube and an electrometer. Its usable range is from 300 nm to 650 nm. The electrometer amplifies the nanoampere sized current

from the PMT to a measurable voltage. A sampling board in the computer converts the voltage to 12 bit numbers at a rate of 11 KHz. Sums and sample counts of the digitized electrometer voltage are stored in consecutive bins along with the wavelength of the end of the bin. The width of the bins can range from 0.01 to 655.35 nm/bin. The measurements presented here use a width of 1 nm/bin.

Support instrumentation included a PD-1 Davos pyranometer and a Linke Feußner pyroheliometer to verify constancy in the incoming radiation field during spectral sampling. Other meteorological and glaciological equipment was used as additional support.

3.5 Place and Time of Observations

The measurements were taken on the Juneau Ice field which lies North of Juneau, Alaska. There are about 4000 km^2 of glacierized terrain. The specific location was the Taku Glacier, one of the larger glaciers (18 km length) of the ice field. More than 40 years of glaciological work has been carried out on the Juneau Ice field under the leadership of M. Miller[38,39,40]. Measurements were carried out on the Taku Glacier close to Camp 10 (58° 37' N, 134° 30' W, altitude of 1077 m), one of many research and training camps established by M. Miller. Our group occupied the camp from 21 July to 4 August 1991.

There had been a new snow fall on 18 July, but by the time measurements were able to begin three days later, the snow was melting. The snow grain size was 1.0-1.2 mm, and the density ranged from 0.50 to 0.55 g cm^{-3}.

Measurements were obtained under different sky conditions. For example, there were clear skies on 21 July, medium to thin stratus clouds on 26 July, and thick stratus with drizzle on 27 July 1991.

3.6 Observations

3.6.1 Downward Irradiance

The solid line in Figure 3.2 shows a measured spectrum of direct beam solar irradiance between 330 and 600 nm. The measurement was taken at 10:45, 21 July 1993 Alaska local time under clear sky conditions. The data have been converted from PMT current to irradiance by comparison to a standard lamp. Since the cable end has a 12° field of view, the spectrum also includes light scattered in small forward angles. The major Fraunhofer solar absorption lines can easily be seen in the measured spectrum. A few are labeled in Figure 3.2.

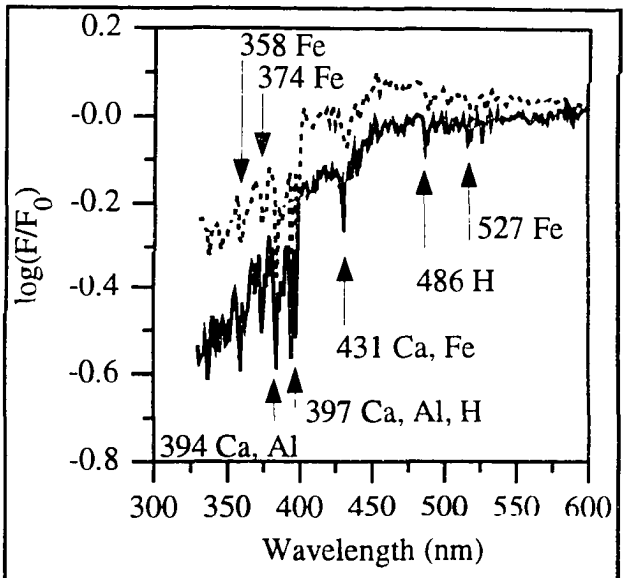

Figure 3.2. The solid line is a direct beam spectral irradiance (F) measured at 10:45, 21 July 1991 solar time (solar elevation = 45°), on the Taku Glacier, Juneau Icefield, Alaska. The cable end was aimed at the sun under clear sky conditions. The dotted line is the direct beam spectral irradiance(F) above the Earth's atmosphere as reported by Iqbal (1983). Each curve has been normalized to the irradiance at 600 nm (F_o).

The dotted line in Figure 3.2 represents the spectrum of direct beam solar irradiance above the Earth's atmosphere taken from Iqbal[41]. The agreement between the two curves gives confidence in the instrumentation used. Not only are the general forms of the spectra similar, but the peaks also occur at the correct wavelength. Both curves are normalized to their respective irradiance value at 600 nm.

In Figure 3.3 measurements of diffuse sky radiance under clear and cloudy (stratus clouds) sky conditions are presented. In both cases collected light was traveling straight down in the 12° field of view of the cable end. These curves are in units of current from the PMT detector (I) in microamperes. As expected the spectral radiance for the clear sky

is about an order of magnitude less than for the cloudy sky since water drops scatter light across the observed wavelengths, and air scatters according to Rayleigh scatter.

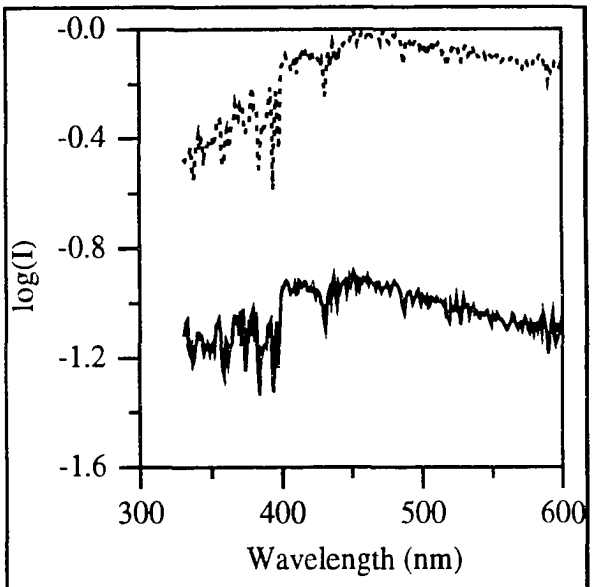

Figure 3.3. Microamperes (I) from the light detector for measurements of downward sky spectral radiance under clear (solid line) and cloudy (dotted line) conditions. The light was collected by pointing the optic cable end straight up (12° field of view). The solar elevations were 46° and 44° respectively.

The scattering and absorption by stratus cloud cover can also be seen in Figure 3.4. The solid line is the ratio of diffuse clear sky radiance to the direct beam irradiance. The dotted line is the ratio of the diffuse sky radiance measured under a thick stratus cloud layer to the direct beam irradiance. The same direct beam spectral irradiance is used for both ratios. Both curves are normalized at 450 nm. The solid curve shows that a cloud-free atmosphere scatters light into the optic cable's field of view much more strongly toward shorter wavelengths, as expected from Rayleigh scattering. Measurements of diffuse to direct ratios by Garrison et al.[42] (1978) display an increase farther into the UV. Photographs with a 320 nm filter taken by Livingston[43] reveal a bright, optically thick atmosphere.

The dotted curve has a flat maximum from about 450 to 550 nm, and drops off toward the UV and yellow-red. This is consistent with the solar beam being scattered by a water cloud with drop sizes much larger than the wavelength of observed light. Large drop size means even scattering across the wavelength range, and water absorbs more in the UV and yellow-red compared to the blue and green region.

3.6.2 Albedo

The terms reflectivity and albedo have different meaning in this article. Reflectivity is the upward traveling radiance reflected from a surface, divided by the downward traveling radiance from the sky. The measured radiance values are monochromatic, and contain light collected in the 12° field of view of the optic cable end. Albedo refers to the spectrally integrated irradiance reflected from a surface, divided by the integrated downward sky irradiance. The irradiance values measured here were done with the Davos pyranometer which collects light in a 2π solid angle.

Snow has the highest reflectivity of all natural substances. Albedo values in excess of 90% have been observed for new dry snow. The albedo is not only high but also can vary widely depending on snow age, grain size, and contaminants[44]. Pioneering work was carried out by Liljequist[45] in Antarctica, and by Dirmhirn and Trojer[46] in the Austrian Alps.

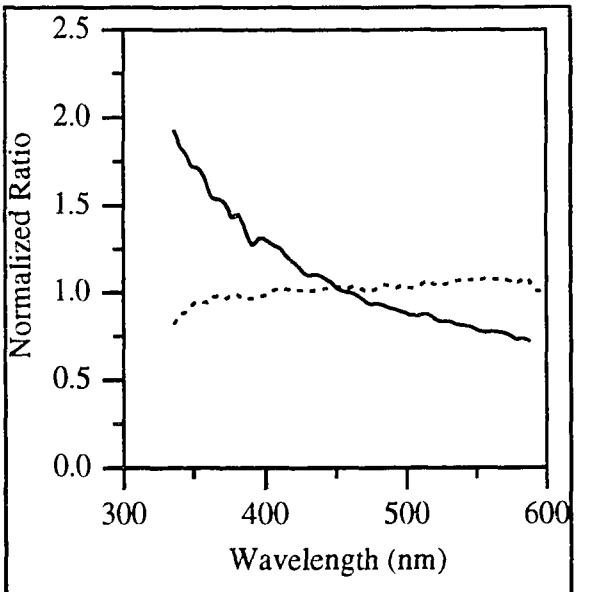

Figure 3.4. Downward spectral radiance ratios. The solid line is the clear sky diffuse radiance divided by the clear sky direct beam. The dotted line is the downward diffuse radiance measured under a thick stratus cloud layer divided by the same direct beam measurement. Both curves are normalized at 450 nm. The clear sky and direct solar beam measurements were taken near 11:00, 21 July 1991 solar time (solar elevations = 46° and 44° respectively), and the cloudy sky measurement was taken at 10:44, 27 July 1991 solar time (solar elevation = 43°). The sky radiance measurements were taken by pointing the optic cable end straight up (12° field of view).

A fairly complete model of the optical properties of snow from the visible to infrared with and without contaminants were produced by Warren[47]. The reflectivity was found to depend strongly on snow grain size, snow age, contaminate concentration, and whether the

snow had never melted, was wet, or refrozen.

Reflectivity was calculated from two spectral measurements. It is the ratio of the upward traveling radiance reflected from the snow surface divided by the downward sky radiance. The radiance values were measured by directing the 12° field of view of the optic cable end straight up at the sky, and straight down at the snow surface. The measurements were made under a thick stratus cloud layer to ensure isotropic sky radiance so that the reflectivity can be comparable to measurements with the 2π pyranometer measurements. The spectral reflectivity (solid line in Figure 3.5) shows a fairly strong dependence on wavelength. It has its maximum in the blue-green, and drops in the UV and yellow-red wavelength bands. For comparison, the dotted line in Figure 3.5 is from measurements in the visible range by Grenfell and Maykut[16], carried out on snow covered ice near the T-3 ice island in the Arctic Ocean, the shorter dashed line is from model calculations by Warren[47] for 1 mm snow grains with a volcanic ash concentration of 10 ppm by weight and the longer dashed line is for alpine snow from Grenfell and Perovich[48]. All reflectivity curves agree between 400 and 600 nm except for the Grenfell and Perovich data. Our measurements give a lower reflectivity toward the UV, which is more in agreement with previously published results by Eaton and Dirmhirn[49]. This is furthermore

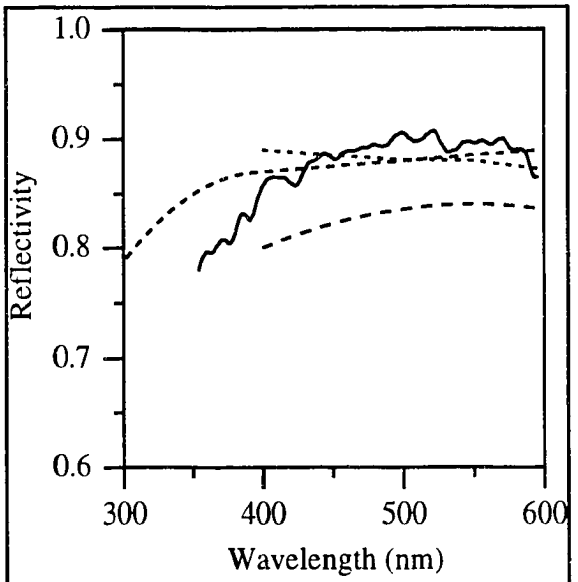

Figure 3.5. The solid line is the spectral reflectivity of snow taken on the Taku Glacier, 27 July 1991. Note that the reflectivity has its maximum in the blue/green, and decreases both for longer and shorter wavelength. The dotted line is a measured spectrum by Grenfell and Maykut[16] carried out near T-3 in the Arctic Ocean, the shorter dashed line is from model calculations by Warren[47] for snow with a volcanic ash concentration of 10 ppm by weight, and the long dashed line is alpine snow from Grenfell and Perovich[19].

in agreement with results published by Ambach and Eisner[50], who compared UV to the global radiation. They found similar results to ours for "dirty" snow, but the opposite for clean snow. This effect is likely due to multiple reflection between the snow surface and cloud layer[51], since both absorb more in the UV and yellow-red ranges than in blue or green. A model by Dozier et al.[52] shows similar values to those presented in Figure 3.5.

The mean reflectivity for our measured range of 350 and 600 nm was 87% for the snow on the Taku Glacier. The integrated albedo over the entire spectrum was measured by the Davos pyranometer at 66%. The difference is expected since the pyranometer includes the red and near IR. The reflectivity of wet snow in these regions is substantially lower.

For comparison, the mean reflectivity was estimated from the model calculations[47] used for the short dashed line in Figure 3.5. The mean is about 87% in the 300 to 600 nm band, 33% in the 600 to 1500 nm band, and 55% for the full range of 300 to 1500 nm.

3.6.3 Light Extinction

Measurement of spectral extinction in a snow pack has been difficult in the past[53]. It has been common to place a filter radiometer in an undercut hole, or at the end of a snow column. These methods lead to considerable disturbance of the snow-pack which can lead to significant errors. Another method is to take snow or ice samples to a laboratory and analyze them using an artificial light source. Again, many errors are encountered[54].

The use of a fiber optic cable greatly reduces the snow-pack disturbance. A 1 m wide by 1.5 m deep trench was dug in the snow pack to carry out our measurements. Horizontal holes were drilled in the walls of the trench at several depths. The holes were 1 m long with a diameter of 2 cm. The end of the cable was then inserted into the holes. The collected light was traveling horizontally within the 12° field of view of the cable end. The same technique was used by Grenfell and Maykut[16] to measure extinction in the visible region. The assumption that below the surface layer, snow scatters light strongly enough to make the horizontally directed radiance proportional to the downward irradiance is used

to calculate extinction.

In Figure 3.6 the natural log of horizontal radiance (I) in three integrated wavelength bands is plotted against depth. A linear regression is drawn for each band. For totally uniform snow, a straight line is expected according to the Bouguer-Lambert Law. The point scatter around each line in Figure 3.6 is expected because the snow pack is not uniform. Extinction coefficients (K) are found from the linear regression lines. The red (590-610 nm) shows the strongest decrease with depth ($K = 9.8\ m^{-1}$), while in the blue (450-470 nm) the absorption is at a minimum ($K = 4.6$). The ultraviolet (350-370 nm) lies between these two values ($K = 6.8$). Green (520-540 nm), which is not shown in the graph, displayed a very similar value to the UV ($K = 6.7$). The extinction coefficient as a function of wavelength is given in Figure 3.7. The lowest values of 4.2 m^{-1} were found near 480 nm, while the highest values of 8.8 and 7.5 m^{-1} occurred at 350 and 580 nm, respectively. The extinction curve explains why the walls of a snow or ice cave look blue, where there is a minimum in spectral extinction. Extinction coefficient model calculations by Warren[47] for pure snow with a crystal size of 1.3 mm are also included in Figure 3.7. The shape of the two curves is very similar.

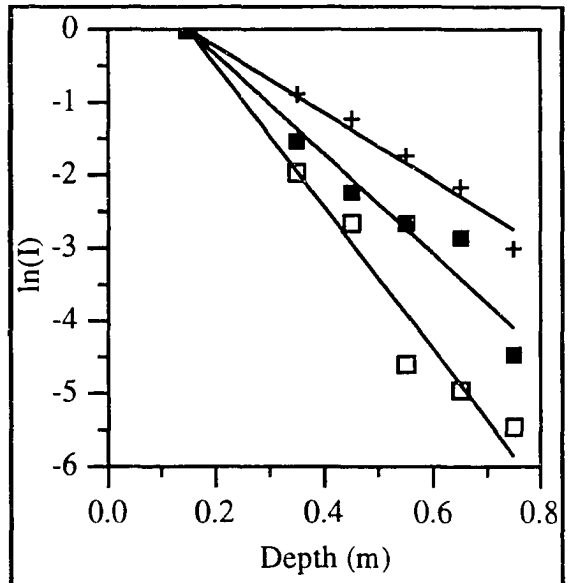

Figure 3.6. The natural log of the light detector current for measurements of radiance in different wavelength bands vs. snow depth. For totally uniform snow, a straight line is expected. The 590 - 610 nm (red) band shows the strongest decrease with depth, while 450 - 470 nm (blue) is absorbed the least. 350 - 370 (UV) lies between these two values. The 520 - 540 nm band (green, which is not shown) displayed very similar values to the UV.
■ = 350 - 370 nm
+ = 450 - 470 nm
□ = 590 - 610 nm.

3.7 Conclusion

The use of a quartz fiber optic bundle greatly aids light extinction measurements. It makes intensity measurements possible with only a small disturbance to the medium in question. Spectral sky and reflectivity measurements are simplified by orienting the cable end instead of the entire spectrometer.

A comparison of spectral intensities for clear and cloudy conditions shows all wavelengths being strongly scattered by clouds. The cloud layer was optically thicker in the UV-A and yellow-red compared to the blue-green band.

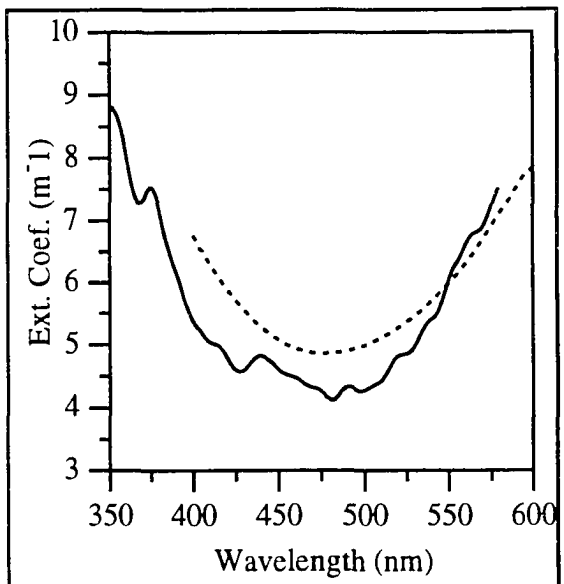

Figure 3.7. The solid curve is the extinction coefficient in snow on Taku Glacier, 26 July 1991. The dotted curve is from model calculations for pure snow with a snow grain size of 1.3 mm[47].

Reflectivity and extinction measurements agree generally with previous work, both actual observations and model calculations. The maximum in reflectivity and the minimum in extinction were measured at a wavelength of 480 nm (blue). Toward the UV, and even to a greater extent toward the longer wavelengths the reflectivity decreased and the extinction coefficient increased.

4. Extinction of Near Ultraviolet and Visible Light in Summer Antarctic Sea Ice

4.1 Introduction

Measurements of the extinction of light in summer Antarctic sea ice were carried out during a cruise of the USCG Polar Star between Hobart, Australia, and McMurdo Station, Antarctica. The Polar Star left Hobart on 18 December 1992, and arrived at McMurdo on 3 January 1993. During that time measurements were taken on 5 free-floating ice floes, and one group of measurements was made at the edge of the fast ice in the Ross Sea. Extinction curves were calculated using Equation 1.10 from spectra of downward travelling light taken at several depths. The wavelength range was 350 to 700 nm with a resolution of 1 nm. The extinction values were then compared to the physical characteristics of the ice (crystal type, size, inclusion volume, salinity, temperature and contaminants).

4.2 Instrumentation

As stated in Chapter 1, the spectrometer was fitted with a single fiber optic cable to carry light from the ice light collector for this study. Figure 4.1 is a drawing of the spectrometer arrangement used for this trip. The photographs in Figures 2.1, 2.2 and 2.3 show the spectrometer in its case, and the light collector support hardware on an ice flow. The sky flux collector in Figure 2.3 was later constructed as a result of the measurements presented in this chapter. The description of the spectrometer and light collector is in Chapter 2. The diffuser cavity is the same used for the snow optics measurements in Chapter 3. An 1180 groove/mm grating was used in the spectrometer, the slit width was adjusted to 500 μm, and the PMT signal was sampled at a rate of 15 KHz and averaged into data points of 1 nm resolution. This produces an overall resolution of 2 nm.

Other support instrumentation and tools included a Davos global pyranometer to monitor the sky radiation while sampling, a 5 cm ice drill, 10 cm ice coring drill, and instruments to measure ice temperature and salinity as described by Jeffries et al.[55].

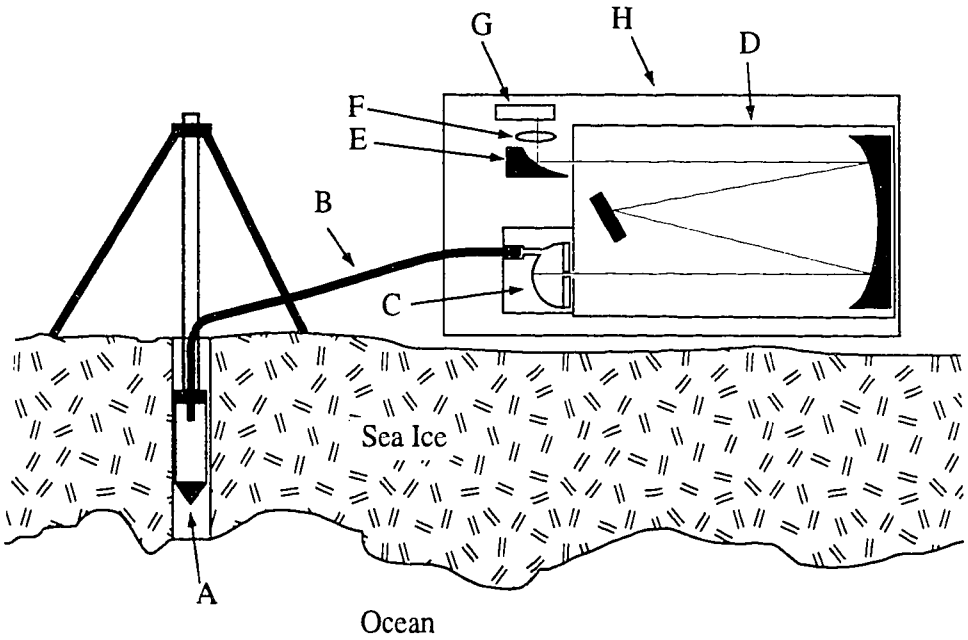

Figure 4.1. Spectrometer optics arrangement on an ice floe.

A = light collector	E = parabolic mirror
B = quartz fiber optic cable	F = quartz lens,
C = diffuser cavity	G = PMT
D =Ebert spectrometer	H = light tight box.

4.3 Measurements

Once an ice floe was selected, the Polar Star was maneuvered to the windward side of the floe for safety reasons. The equipment was moved onto the ice via crane and the spectrometer was set up near the center of the floe. Ice temperature and salinity were measured from a core taken about 5 m from the ice optics measurements. After the optics work was complete, a core was taken next to the optics ice hole to observe the ice crystal structure.

To prepare for the ice optics measurements, the spectrometer was turned on, and the PMT allowed to stabilize. During this time the 5 cm diameter drill was used to make a vertical

hole through the ice, the ice thickness was measured, and the optic cable and light collector support were set up.

Spectra were measured at several depths in the floe. The hole was covered with a 5 cm diameter piece of black foam while sampling. The light collector depth was measured from the reflector surface to the top of the ice, according to previously made marks on the support pipe. The Davos pyranometer was monitored during the 2 minutes required to scan a spectrum. If the global sky radiation changed by more than 5%, the scan was repeated.

While one group gathered the light spectra, another drilled the ice cores. Immediately after the first core was taken, the temperature was measured at 10 cm intervals and the core was cut at the same points and bagged for later salinity measurements. The second core was drilled near the light measurement hole and placed in core tubes for later structure analysis.

There were three types of ice encountered. They were free floating pack ice floes with a deep snow cover (20 - 100 cm), the same with very little snow (1 - 3 cm), and finally the fast ice in McMurdo Sound.

The deep snow removed too much light (K ~ 15 - 20 m^{-1}) to get an acceptable signal to noise ratio in the ice, but the thin snow cover allowed good data. Figures 4.2a - f describe such an ice floe with 1 - 2 cm of wet snow.

This floe was positioned at 76° 5.8' S, 167° 50.6' E. It was about 30 m in diameter and 1.88 m thick at the hole drilled for light measurements. The ice temperature was fairly constant ranging from -1.8 at the top and bottom, to -2.7 at 0.4 m depth. The water temperature was -1.8 °C. The salinity ranged from 7.4‰ at the top, peaked at 11.3‰ between 0.2 and 0.3 m, and dropped to 6.6‰ at the bottom. The ice temperature suggests it was in a state of melting, but the cores taken were consolidated ice. The sky was overcast with an altostratus cloud layer, and the solar zenith angle ranged from 51.51° to 51.55° during the sampling period, which gives a zero air mass global irradiance ($1367*\cos(\theta)$ wm^{-2}) of 851 to 850 wm^{-2}.

Figure 4.2a is a contour plot of the downward light as a function of depth from the top of the ice, and of the wavelength of light. Spectra were taken at depths of 0.1, 0.2, 0.4, 0.6, 0.8, 1.0, 1.4, 1.8 and 2.0 m. The spectra at 0.1 m and 2.0 m were strongly affected by their nearby boundaries (K ~ 10 - 15 m^{-1}) and are not presented here. The wavelength range is 360 - 700 nm. The data were normalized to the spectrum taken at 0.2 m. A 5th order polynomial was fit to each normalized spectrum, and a linear interpolation was used to create spectra at every 1 cm depth interval. This gave an evenly spaced matrix to calculate contour lines. The polynomial fit to the measured data was used to smooth the fluctuations caused by changes in the sky radiation. The correlation for each fit was always better than $R^2 = 0.98$.

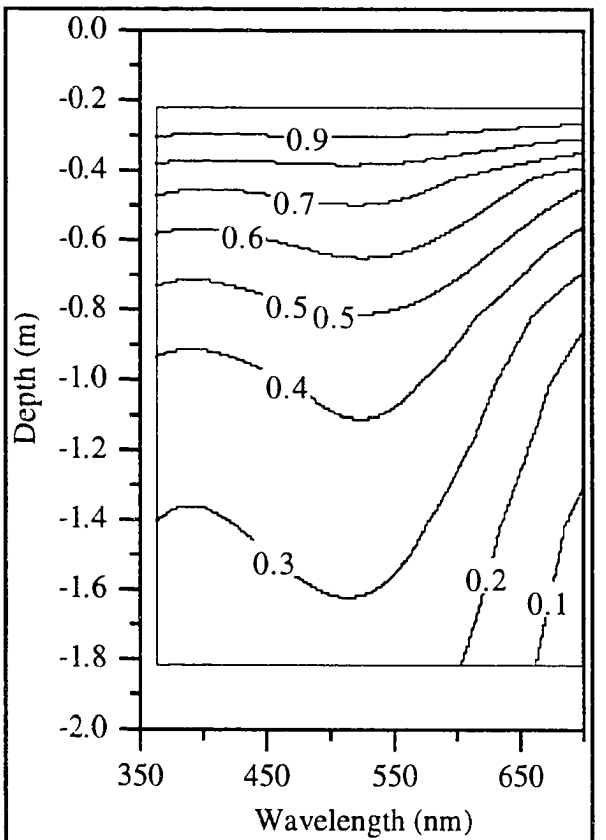

Figure 4.2a. Contours of downward light normalized by the spectrum measured at a depth of 0.2 m. The spectra were measured from a drifting ice floe, 30 m diameter, 1.88 m thick, on 1 Jan 93, at 76° 5.8 S, 167° 50.6 W, and solar zenith angles 51.51° - 51.55°. The data for wavelengths shorter than 360 nm are not shown because of marginal signal to noise ratio in the bottom depths at short wavelengths.

Figure 4.2b is a contour plot of the downward light extinction calculated from the polynomial light intensity spectra used to create Figure 4.2a. Extinction can be calculated from Beer's law and the spectra at the top and bottom of each layer, assuming that light entering the collector is proportional to the downward flux. Each extinction curve was spaced at the center depth of it's respective layer for the depth-wavelength-extinction matrix calculation,

and contours were derived from that matrix. That is why the top of the graph is at a depth of 0.3 m and the bottom is at 1.3 m. The units of the contour labels are m^{-1}.

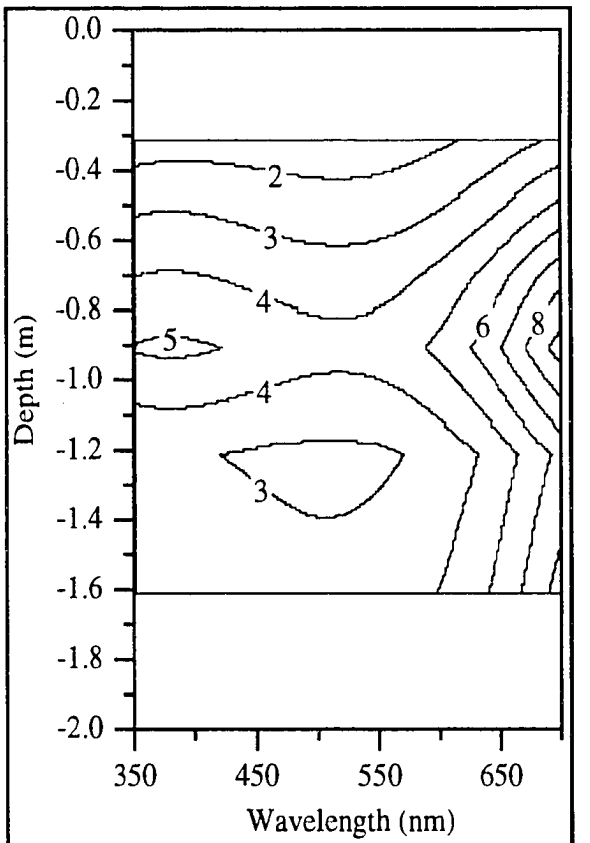

Figure 4.2b. Extinction coefficients calculated from the spectra in Figure 4.2a. The contours are in units of m^{-1}.

Figures 4.2c - f are the physical properties measured from one of the ice cores. Vertical sections 4 mm thick were cut with a band saw. The sections were viewed between cross polarized films on a light table to observe the crystal widths (Figure 4.2c) and ice type (Figure 4.2d) according to descriptions by Jeffries[55]. When the core was removed from the hole, there were several breaks. These could be thin horizontal void areas, or simply weak spots in the ice that broke while drilling. The breaks are marked in Figure 4.2f by horizontal lines and depth marks to the right of the figure.

After viewing the crystal structure in the cold room, it was observed that there were three types of inclusions in the ice: spherical, planar, and tubular. The ice around the inclusions appeared very clear. The cold room was at -12 °C. This is well above the temperature of -23.5 °C where solid salts form in the brine pockets. The spherical inclusions appeared to be gas bubbles with optically smooth boundaries, and the diameters ranged from 0.1 to 5 mm. The planar inclusions were primarily vertically oriented with thickness about 0.1 mm and mean diameters between 1 and 10 mm, and the boundaries were smooth. These were probably brine pockets in the congelation crystals that drained while the cores were in transit. The tubular inclusions appeared to be vertical brine drainage tubes with widths of 1 to 20 mm and were 10 to 200 mm long. The boundaries were rough in spots or entirely rough. The side of the core not

used for vertical sections was cut for density and contaminant measurements. Physical layers were defined by crystal type and visual estimates of inclusion densities in the vertical sections. The inclusion volume was calculated from ice density measurements. The bulk ice density (Figure 4.2f) for each layer was found by cutting several 3 cm cubes, measuring the length, width, and height with calipers within 0.5%, and weighed to 0.01%. Since brine drainage occurred before these measurements, the density is really an indicator of the volume density of all inclusions. The remainder of the ice was placed in sample bags, melted, filtered onto dried and weighted quartz fiber filters, dried, and finally weighed with the contaminant. After correcting for the difference in ice and water density, this gives a contaminant concentration (Figure 4.2e) in units of µg/ml of ice. Unfortunately the samples were in a liquid state too long to measure chlorophyll.

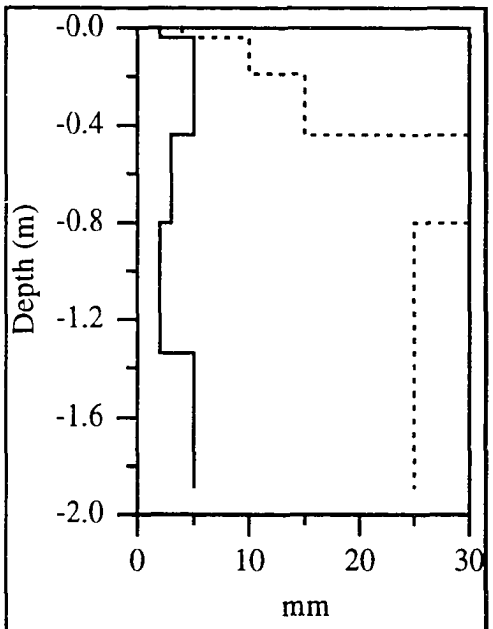

Figure 4.2c. The max and min crystal size from the ice floe. The size is the crystal diameter in frazil ice, or crystal width otherwise.

Figures 3a - f describe similar measurements done near the edge of the fast ice in the Ross Sea. The position was 77° 37.7' S, 165° 7.0' E. The ice had 0 - 1 cm of snow cover and was 2.14 m thick. The ice temperature ranged from -1.7°C at the top, rising steadily to -1.2°C at the depth of 1.6 m. The water temperature was -1.7°C. The salinity ranged from 3.6‰ at the top to 8.2‰ at 0.4 m, and dropped to 7.7‰ at 1.6 m.

Because of our previous experience with loss of light from snow cover, it was decided to remove the snow in a 6 m diameter circle around the optics ice hole to allow more light to penetrate the ice. Spectra were taken at 0.2, 0.4, 0.8, 1.6, and 2.14 m depths in the ice. The sky was clear of clouds, and the solar zenith angle ranged from 55.4° to 54.6° during the ice optics measurements, so the zero air mass irradiance was 777 to 791 w m^{-2}. Figure

4.3 graphs were produced in the same manner as the Figure 4.2 graphs. The core at depths 1.44 - 1.6 m was damaged so there is no data in this range for Figures 3c - f. There is also no data at depths 0.94 - 1.24 m in Figure 4.3e because some sample bags leaked.

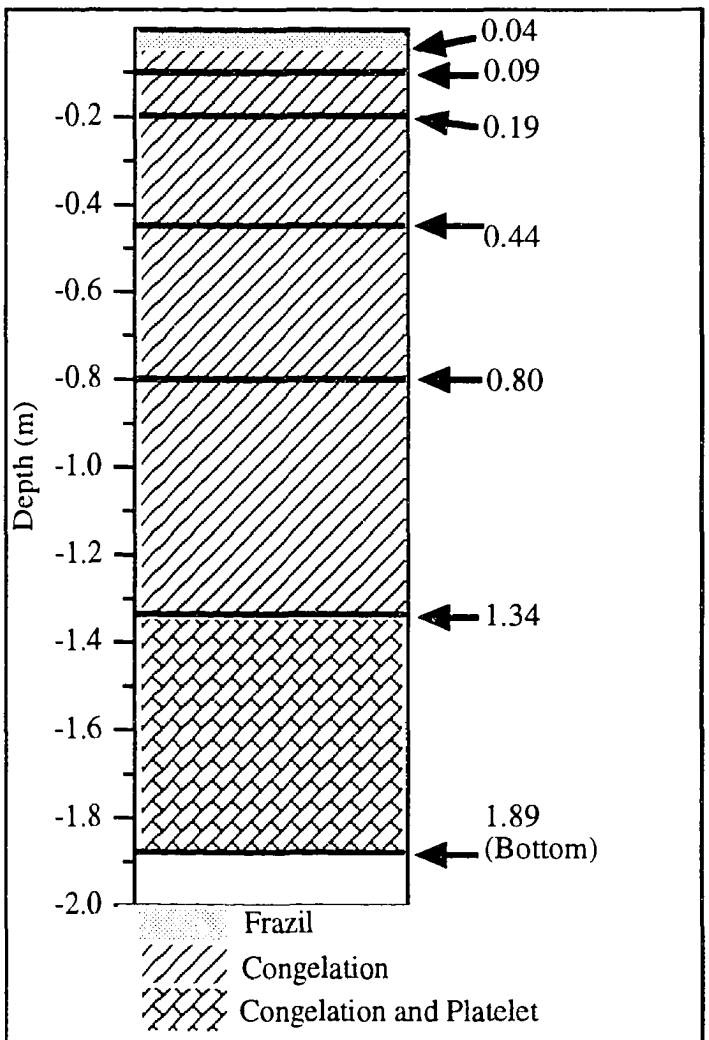

Figure 4.2d. The crystal type and breaks in the core taken from the ice floe. The breaks are marked at the right by depths and arrows.

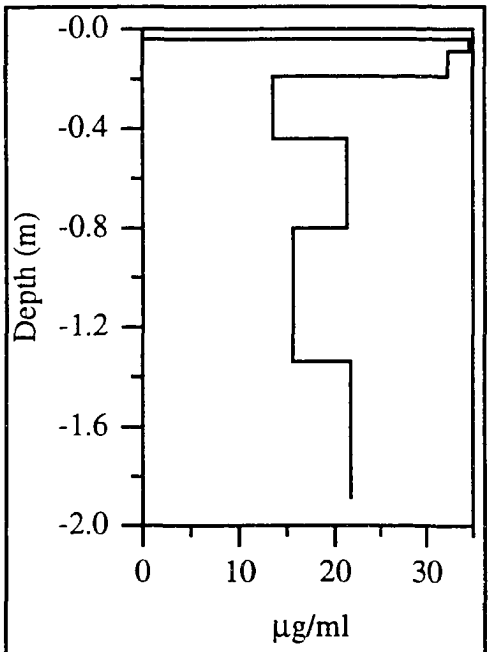

Figure 4.2e. The filtered contaminant concentration in the ice floe measured by melting ice core samples in bags, filtering onto dried and preweighed quartz fiber filters, and finally dried and weighed.

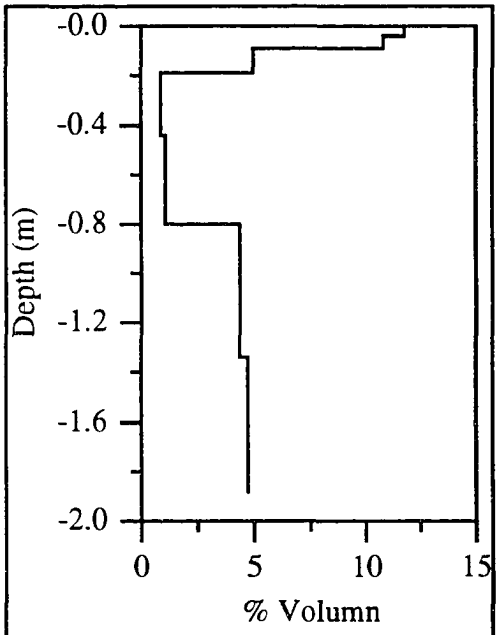

Figure 4.2f. The percent volume of gas and brine inclusions in the ice floe. These values were calculated from the density measurements of 3 cm cubes cut from the ice core after brine drainage occurred.

4.4 Discussion

In general, the ice floe of Figure 4.2 shows the expected extinction as a function of wavelength for ice in a state between first year grey ice[3] and first year blue ice[16] with extinction values ranging from 2 to 9 m^{-1}. The exception to this is a small peak at 400 nm at all depths in Figure 4.2b. Algae with a large fraction of detrital material would produce the overall larger extinction values compared to those in Figure 4.3b, but the chlorophyll absorption peak should occur at 430 nm.

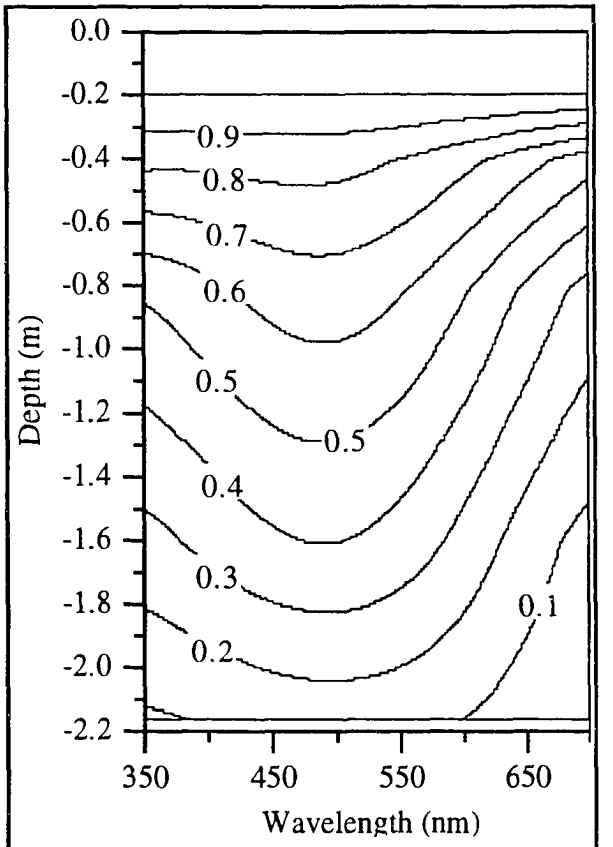

Figure 4.3a. Contours of downward light normalized by the spectrum measured at a depth of 0.2 m. The spectra were measured near the edge of the fast ice in the Ross Sea. The ice was 1.88 m thick. Measurements were taken on 6 January 1993, at 77° 37.7' S, 165° 7.0' E, with solar zenith angles 55.4° - 54.6°.

The extinction in Figure 4.2b increases from the 0.2 - 0.4 m layer to the 0.8 - 1.0 m layer, and then decreases slightly toward the bottom. The contaminant concentration is fairly steady with an average of 20.4 μg/ml. The small inclusion volume (1%) in the 0.2 to 0.8 m layer and larger (5%) volume in lower layers agrees with the trend in extinction. The average for the entire thickness was 3.8%. The larger amount of inclusions scatters more light which would increase the extinction[3] in depths below 0.8 m. The larger extinction in the 0.8 - 1.0 m layer compared to lower depths is most likely due to a shift if the size and type distribution of the inclusions. More small air bubbles compared to brine pockets would cause larger extinction[3].

Another possibility is spectral changes in the sky radiation between scanning spectra at different depths. For a layer 0.2 m thick, the source light must change by a factor of 0.82 to increase extinction by 1 m^{-1}. Readings from the Davos Pyranometer indicate the global sky radiation stayed within the 5% criterion, so changes in sky radiation are not the likely cause.

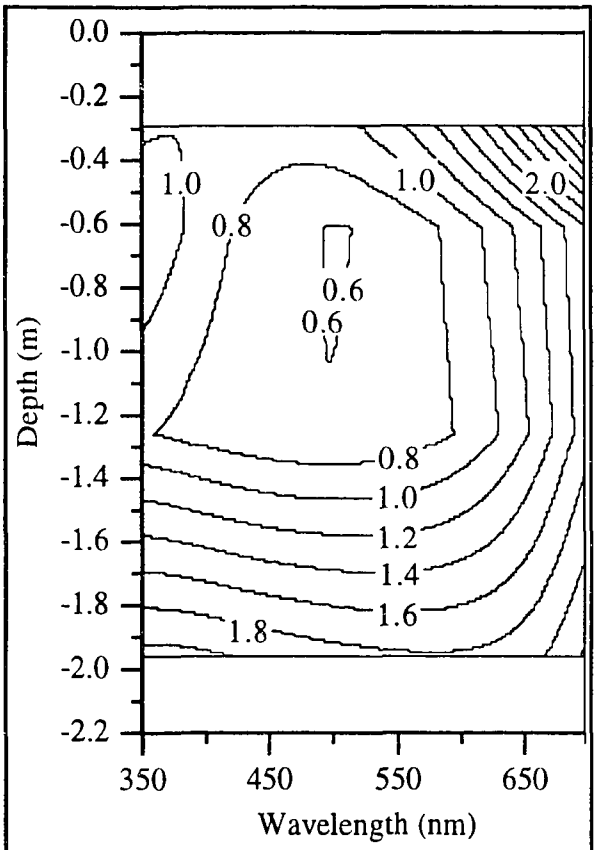

Figure 4.3b. Extinction coefficients calculated from the spectra in Figure 4.3a. The contours are in units of m^{-1}.

The fast ice in the Ross Sea (Figure 4.3a - f) was optically different from that of Figure 4.2. Excluding the top 0.2 m of ice, the extinction ranged from 0.6 to 2 m^{-1} (Figure 4.3b) and followed an expected shape and magnitude for melting blue ice[16]. Also note that there is not an extinction peak at 400 nm in Figure 4.3b.

The contaminant loading (Figure 4.3d) ranges from 10 - 15 µg/ml below 0.2 m depth with an average of 12.5 µg/ml. This is a factor of 0.61 from the ice floe. This ice has areas with much larger inclusion volume fraction (14%) (Figure 4.3e) and a higher average for all depths at 5.7%. In short, the fast ice has more inclusion volume, less contaminants, and less extinction. The smaller extinction agrees with smaller contaminant concentration, and suggests that the inclusions in the fast ice are dominated by brine pockets, which scatter less light, and in a more forward direction than gas bubbles.

The extinction values for the free floating ice floe dropped by about one order of magnitude from the 0.1 - 0.2 m layer ($K \sim 10\ m^{-1}$, not shown in Figure 4.2b) to the 0.2 - 0.4 m layer.

The same change is true to a lesser degree in the fast ice (Figure 4.3b) between the layers 0.2 - 0.4 m and 0.4 - 0.8 m. The depths where the extinction values stabilize are at optical depths (τ = K z) of 0.40 and 0.48 respectively. This suggests that an optical depth of about 0.48 is where light entering the collector is approximately proportional to the downward flux. A similar result was found by Grenfell and Maykut[16] who measured extinction in multi-year white ice and first year blue ice and found that it dropped sharply from 100 m^{-1} to 2 m^{-1} between the surface and 0.1 m depth. From there it decreased to about 1.3 m^{-1} at 1 m in the ice.

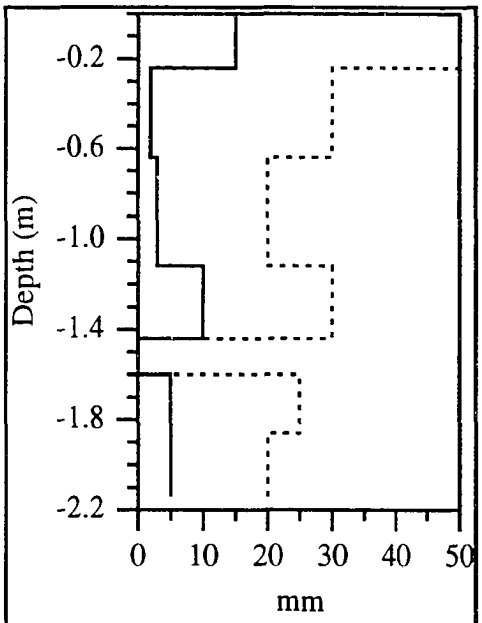

Figure 4.3c. The max and min crystal size in the shore-fast ice. The size is the crystal diameter in frazil ice, and crystal width otherwise.

The estimate for the scattering coefficient in the fast ice is σ = 17 m^{-1} from Equation 1.12 and the values of K = 0.6 m^{-1} (Figure 4.3b at 500 nm), absorption by ice[19] α = 0.1 m^{-1}, and 35% backscattering[25]. If this scattering value also applies to Figure 4.2b, then the absorption by contaminants is $\alpha_{detrital} = \alpha_{total} - \alpha_{ice}$ = 1.1 m^{-1}, where α_{total} is from Equation 1.12. Model results in Section 5.5 indicate that this is a realistic value for absorption by a small amount of algae with a large fraction of detrital material.

Weller[56] found a strong relation between ice grain size and the extinction of broadband solar radiation by snow and ice. Grain size is an important factor in extinction by snow and snow ice due to the direct relation to the amount of refracting air-ice interfaces. In the case of sea ice, the surface of an ice crystal is generally in contact with the ice of other crystals instead of air. Measurements by Grenfell and Perovich[19] show that a collimated beam of light entering a pure, bubble free block of ice was scattered less than 2.6° over a 2.83 m length by the ice crystals interfaces. In general, the optical properties of sea ice are

described in terms of scattering by gas bubbles and brine pockets, and absorption by ice, brine, and contaminants[18,28,25,8,4]. To test the grain size dependence, the extinction at 450 nm for each of the 10 depths in Figures 4.2b and 4.3b was compared to the crystal size for the corresponding layers. The linear fit $K(d) = -0.13\ d + 3.35$ had a correlation of $R^2 = 0.57$, and the exponential fit $K(d) = 3.25\ e^{-0.07\ d}$ produced a correlation of $R^2 = 0.60$. There does not appear to be a relation between the extinction and ice crystal size presented here, but 10 points in not a large enough sample size to make a statistical judgement.

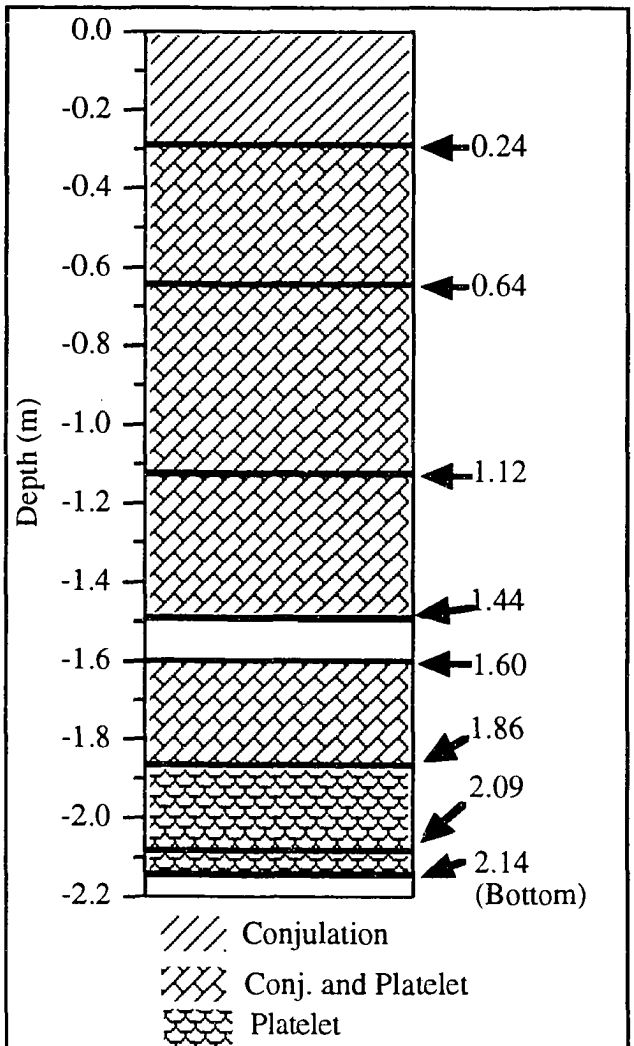

Figure 4.3d. The crystal type and breaks in the core taken from the shore-fast ice. The breaks are marked at the right by depths and arrows.

4.5 Conclusions

At depths where the diffuse radiation field has been produced by multiple scattering, the light that enters the collector is approximately proportional to the downward flux. This region is below optical depths (Kz) of 0.48 from the top surface in sea ice.

In general the shape and magnitude of the extinction agree with the results of others for warm, first year sea ice[18,3]. The free floating ice floe had larger extinction (2 - 9 m^{-1}) than the fast ice (0.6 - 3 m^{-1}). The average percent inclusion volumes (Figures 2e and 3e) were

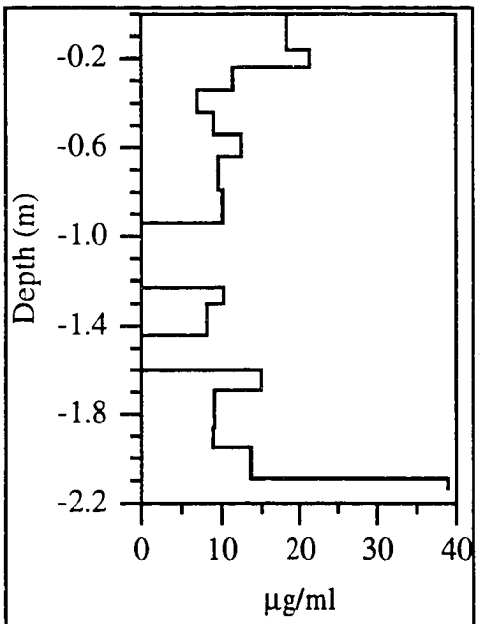

Figure 4.3e. The filtered contaminant concentration from the shore-fast ice, measured by melting ice core samples in bags, filtering onto dried and preweighed quartz fiber filters, and finally dried and weighed.

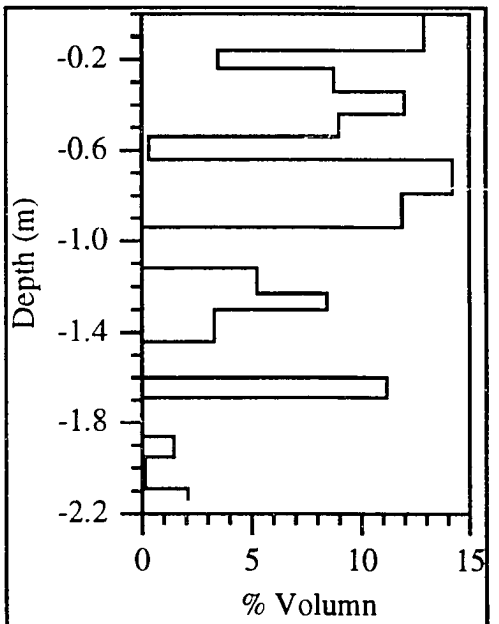

Figure 4.3f. The percent volume of gas and brine inclusions in the shore-fast ice. These values were calculated from the density measurements of 3 cm cubes cut from the ice core after brine drainage occurred.

different by a factor of 1.5. The volume fractions were 3.8% and 5.7% for the floe and fast ice respectively. The inclusions were spherical air bubbles, vertically oriented planer brine pockets, and vertical tubular drainage features. The planer inclusions were dominant in the congelation and platelet ice, where the spherical bubbles dominated the frazil ice. The average contaminant concentrations were 20.4 and 12.5 µg/ml for the ice floe and fast ice, respectively. The fast ice had less contaminant concentration by a factor of 1.6, which agrees with the lower extinction values and the small extinction peak at 400 nm in the ice floe. The scattering coefficient for clean sea ice was estimated at $\sigma = 17\ m^{-1}$, which lead to a value for absorption by contaminants in the ice floe of $\alpha_{detrital}$ 1.1 m^{-1}.

5. Extinction of Ultraviolet–A and Optical Wavelength Light in Winter Antarctic Sea Ice

5.1 Introduction

The purpose of this project was to measure extinction in winter Antarctic sea ice. The work was carried out during a cruise of the ice-reinforced research vessel, N. B. Palmer. The Palmer left Punta Arenas, Chile on 14 August 1993, stopped at O'Higgins and Palmer stations, cruised Southwest to an area North of Thurston Island (about 70° S, 100° W), and traveled as far west as 110° W before returning to Punta Arenas on 3 October 1993. The ice breaker did not reach multiyear ice which was closer to the Antarctic coast. Excluding ridges, ice thicknesses ranged from 0.1 to 2 m with an average of 0.6 m. It was nearly all first year grey ice with some visible brown or greenish layers containing algae.

Ice conditions allowed for light measurements on 21 days between 23 August and 15 September. The data presented here were taken between 10 and 15 September and represent the range of sea ice observed.

The temperature, salinity, and ice structure measurements were taken by Martin Jeffries[55] as part of their research on the cruise.

5.2 Instrumentation

A complete description of the spectrometer and light collectors is the subject of Chapter 2. The diagram of the arrangement on an ice floe is repeated here in Figure 5.1. The entrance and exit slits were opened to 2000 μm to give optical resolutions of 4 and 2 nm with the 1180 and 2360 groove/mm gratings respectively. The PMT signal was sampled at 20 Khz and averaged into points of 1nm resolution.

5.3 Measurements

Once an area of sea ice was selected, the Palmer was pulled along-side and the equipment

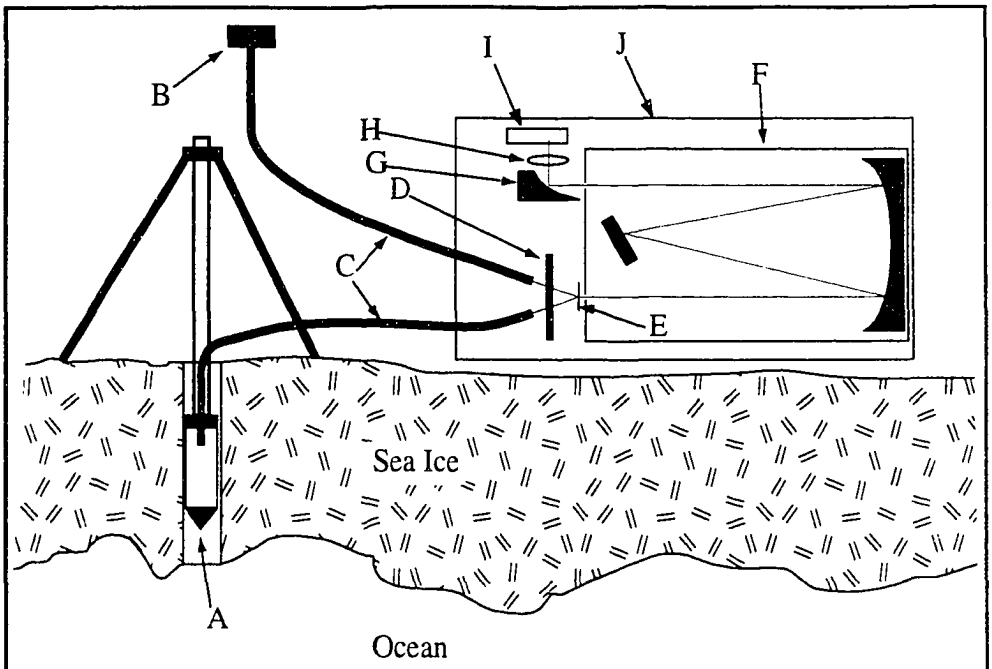

Figure 5.1. Diagram of optics arrangement on an ice floe.

A = Ice light collector	F = Ebert spectrometer
B = Sky flux collector	G = Mirror
C = Quartz fiber optic cables	H = Quartz lens
D = Filter wheel	I = Photomultiplier tube
E = Quartz Diffuser	J = Light tight box

was loaded onto the ice by crane. If it was possible to avoid the shadows of people working nearby, an ice optics site was selected on the same floe as the ice structure work. Otherwise, a nearby floe was chosen. This choice allowed using the ice structure, temperature, and salinity measurements performed by Jeffries group with the ice optics measurements.

Before preparing the site, the instrument was turned on to allow the PMT to stabilize. To prepare the ice, the snow was removed from a 3 to 6 m diameter area. The optical effects of the snow edge on the measurements are addressed in section 5.5. A 5 cm diameter hole was drilled through the ice in the center of the cleared area, and the ice light collector tripod

was set up over the hole. The sky light collector was erected on the south side of the cleared area near the spectrometer.

Spectra were taken at every 10 cm depth in the ice. Measurements at all depths were done with the 1180 groove/mm grating, then the latter was replaced with the 2360 groove/mm grating and measurements were repeated at each depth. If time was limited, spectra were taken at 20 cm depth intervals.

For wavelengths longer than 400 nm, the changes in the sky radiation and the wavelength-dependent instrument transmission were removed by normalizing each ice light spectrum by it's sky flux spectrum. Ice light spectra below 400 nm were scaled by the sky flux value at 400 nm because the sky flux optic cable had poor transmission in this wavelength range. To remove the effects of light guide and instrument transmission, all spectra were normalized by the spectrum at the top depth. The resulting ratio (R) is expressed in Equation 5.1.

$$R(z,\lambda) = \frac{I(z,\lambda)}{F_{sky}(z,\lambda)} \frac{F_{sky}(z_0,\lambda)}{I(z_0,\lambda)} \qquad 400 \le \lambda \le 900 \text{ nm}$$

$$R(z,\lambda) = \frac{I(z,\lambda)}{F_{sky}(z,400)} \frac{F_{sky}(z_0,400)}{I(z_0,\lambda)} \qquad 320 \le \lambda \le 400 \text{ nm}$$

Equation 5.1

The variable $I(z,\lambda)$ is the downward travelling ice light spectrum at depth z in the ice. The sky flux spectrum recorded concurrently with $I(z,\lambda)$ is denoted by $F_{sky}(z,\lambda)$. The depth z_o represents the top depth in the ice where spectra was measured.

The two gratings used to produce a full spectrum overlap around 600 nm. The two spectra of R at each depth differed by factors ranging from 0.98 to 1.04 for the entire data set at this wavelength point. This is expected since the ice light collector could be placed at a slightly different depth between measurements with the two gratings, or a different

arrangement of slush and ice chips between the collector and ice hole wall. The 600 nm to 900 nm part of the spectra was scaled to match the 400 nm to 600 nm section by the point ratio at 600 nm.

Extinction coefficients were calculated from the R spectra at each site using the Beer's law approximation. When interpreting the extinction curves, it is important to remember that the ice light collector follows a cosine response only for zenith angles between 45° and 85°. The results of measurements in Chapter 4 with this collector suggest that the measured extinction is a reasonable approximation of the asymptotic flux extinction for optical depths greater than 0.48 from the top ice surface.

Figures 5.2 through 5.7 show the data from 10 to 15 September. Table 5.1 contains the characteristics of each site.

Figure 5.2a is the normalized downward light profile in the ice calculated from Equation

Figure Number	Date	Latitude	Longitude	Solar Zenith Angle During Sampling	Zero Airmass Sky Flux (wm^{-2})	Ice Δz (m)	Cloud Cover & type
5.2a - e	10 Sept	70.45°S	101.00°W	76.2 - 78.1	325 - 294	0.85	10/10 st
5.3a - e	10 Sept	70.45°S	101.00°W	78.1 - 81.4	281 - 204	0.35	10/10 st
5.4	11 Sept	70.45°S	101.00°W	80.6 - 75.4	223 - 342	-----	10/10 st
5.5a - e	13 Sept	69.81°S	102.81°W	83.4 - 76.9	157 - 311	0.69	10/10 st
5.6a - e	14 Sept	69.58°S	103.70°W	73.5 - 74.2	388 - 372	0.33	1/10 st
5.7a - e	15 Sept	69.40°S	105.00°W	79.3 - 73.0	254 - 400	1.24	1/10 ci

Table 5.1. Site characteristics for the data presented. Figures 5.2, 5.3, 5.5, 5.6, and 5.7 are measurements of light extinction in the ice. Figure 5.4 is spectral albedo for the same ice of Figures 5.2 and 5.3. Latitude, longitude, and solar zenith angles are in degrees. The zero airmass sky flux is in wm^{-2}, ice Δz is in meters, and cloud cover is in tenths of sky coverage. The cloud type "st" is for low stratus, and "ci" is for cirrus.

5.1. Data with a signal to noise ratio less than 50:1 have been removed. Figure 5.2b contains the bulk extinction spectra between each depth in Figure 5.2a. Figures 5.2c, d, and e are the ice temperature, salinity, and structure profile respectively, from the data taken by Jeffries group.

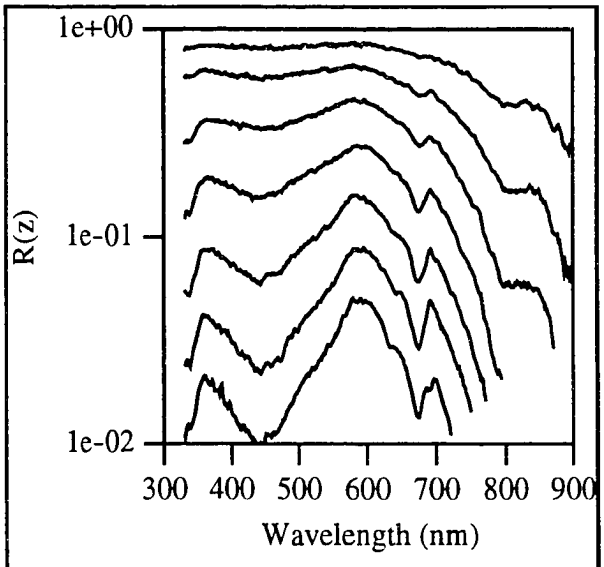

Figure 5.2a. The top to bottom curves are the downward light in sea ice at depths 0.2, 0.3, 0.4, 0.5, 0.6, 0.7, and 0.8 m respectively. The spectra are normalized by the sky flux and the spectrum taken at 0.1 m depth according to Equation 5.1. Data were taken on 10 September. The site characteristics are listed in Table 5.1.

Figure 5.3, 5.5, 5.6, and 5.7 are the same type of presentation as in Figure 5.2a - e. Figure 5.4 is the spectral albedo of the ice described in Figures 5.2 and 5.3. The albedo measurements were taken the day after the extinction measurements. At the time of the albedo measurements, the top surface of the ice had cooled to -7 °C from -4 °C on the previous day, and 4 cm of congelation ice grew on the bottom of the previously 35 cm thick ice of Figure 5.3. The following 15 pages are the above mentioned figures. The text resumes with section 5.4 on page 97, and the discussion of these figures is in section 5.5.

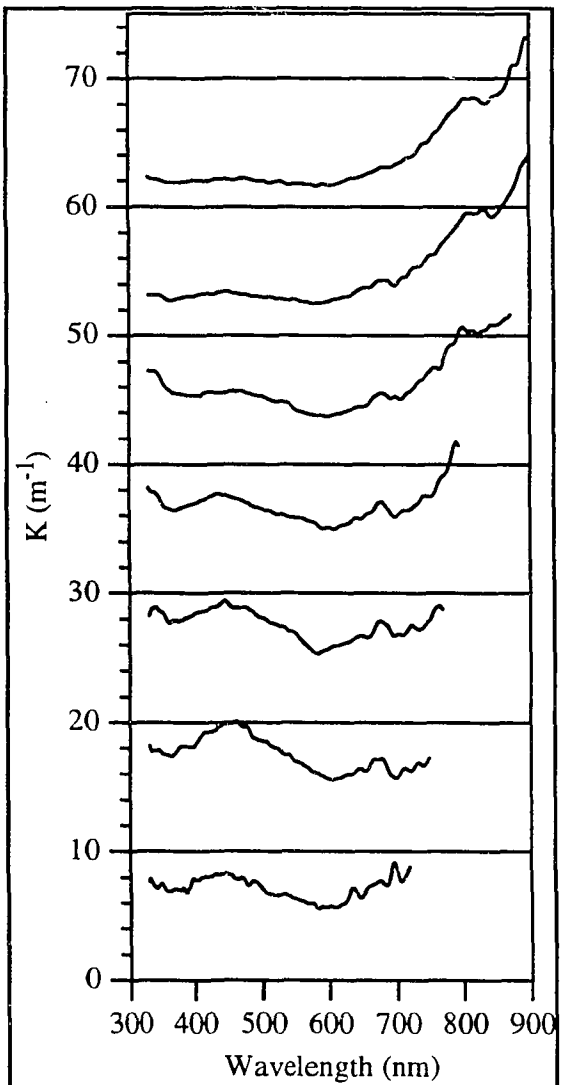

Figure 5.2b. Light extinction between the depths 0.1 - 0.2, 0.2 - 0.3, 0.3 - 0.4, 0.4 - 0.5, 0.5 - 0.6, 0.6 - 0.7, and 0.7 - 0.8 m. These curves were calculated from the data in Figure 5.2a according to Beer's law. Each curve is offset by 10 m^{-1} for clarity so that the zero reference for the 0.1 - 0.2 m extinction is at 60 m^{-1} on the Y axis.

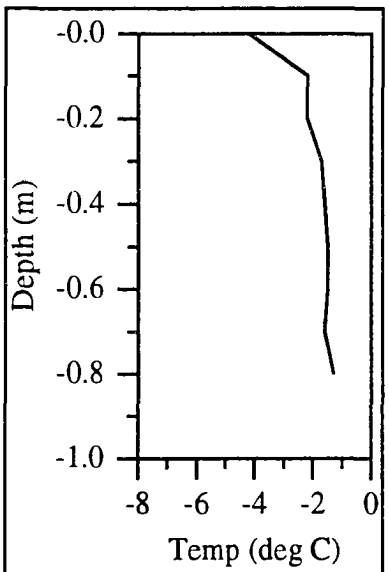

Figure 5.2c. Temperature profile of the ice for Figures 2a, b.

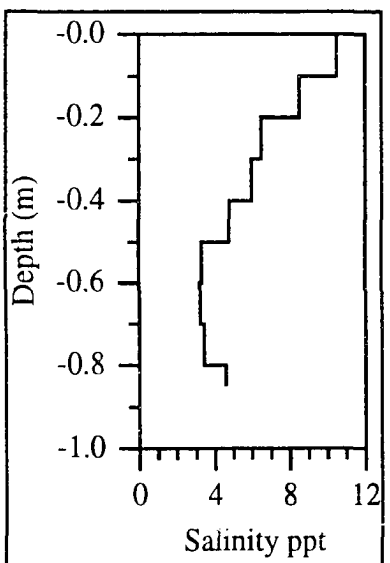

Figure 5.2d. Salinity profile of the ice for Figures 2a, b.

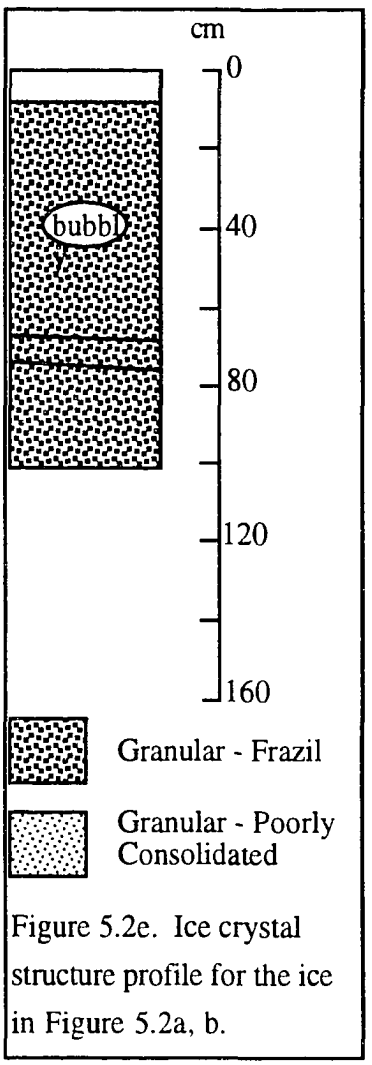

Figure 5.2e. Ice crystal structure profile for the ice in Figure 5.2a, b.

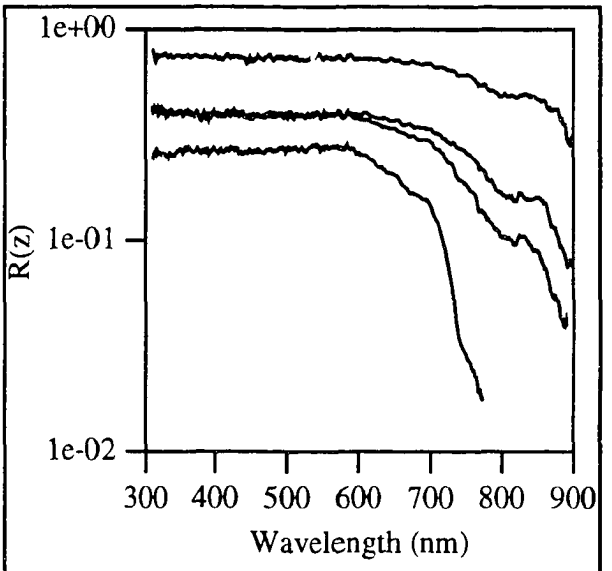

Figure 5.3a. The top to bottom curves are the downward light in sea ice at depths 0.2, 0.3, 0.4 and 0.8 m respectively. The spectra are normalized by the sky flux and the spectrum taken at 0.1 m depth according to Equation 5.1. Data were taken on 10 September. The site characteristics are listed in Table 5.1.

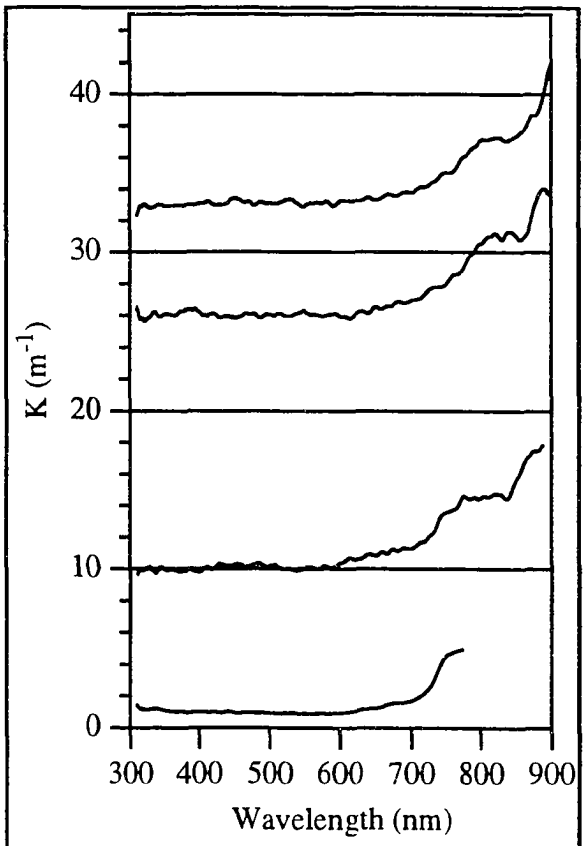

Figure 5.3b. Light extinction between the depths 0.1 - 0.2, 0.2 - 0.3, 0.3 - 0.4 and 0.4 - 0.8 m. These curves were calculated from the data in Figure 5.2a according to Beer's law. Each curve is offset by 10 m^{-1} for clarity so that for the zero reference for the 0.1 - 0.2 m extinction is at 30 m^{-1} on the Y axis.

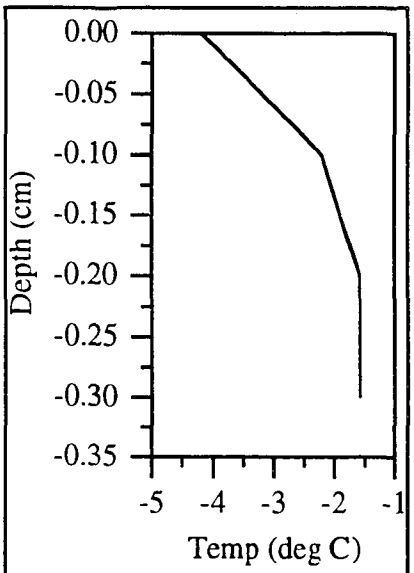

Figure 5.3c. Temperature profile of the ice for Figures 3a, b.

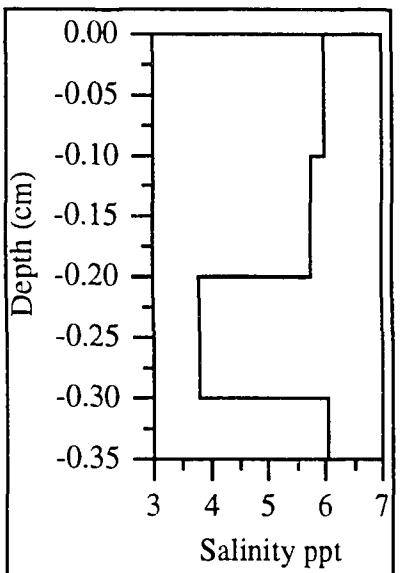

Figure 5.3d. Salinity profile of the ice for Figures 3a, b.

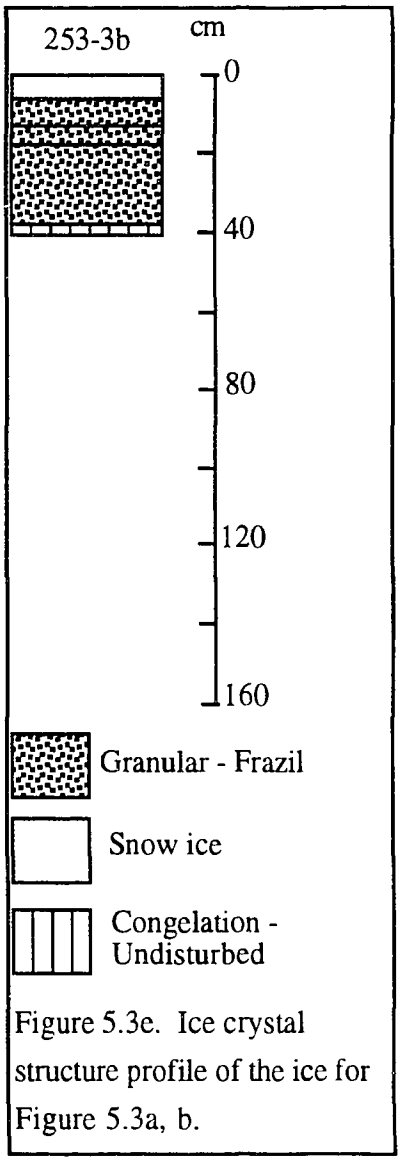

Figure 5.3e. Ice crystal structure profile of the ice for Figure 5.3a, b.

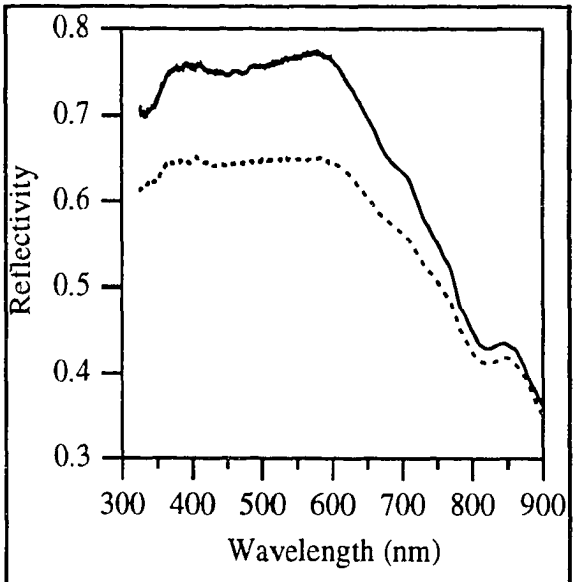

Figure 5.4. The solid curve is the spectral albedo of the ice shown in Figure 5.2, and the dashed curve is albedo of the ice in Figure 5.3. These measurements were taken the day after those shown in Figures 5.2 and 5.3.

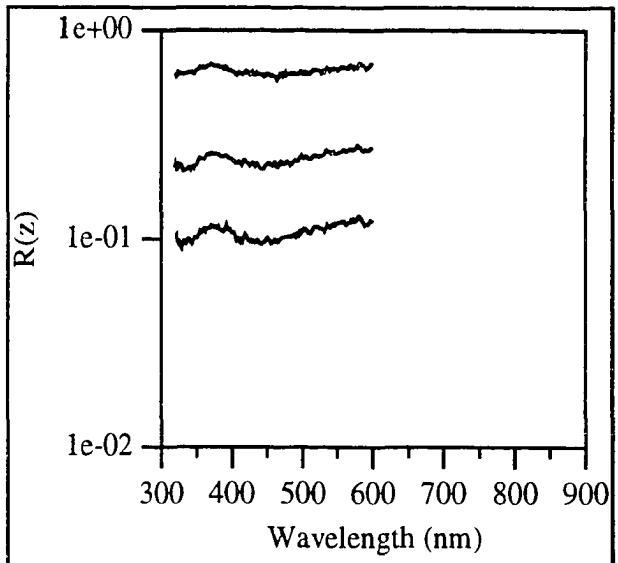

Figure 5.5a. The top to bottom curves are the downward light in sea ice at depths 0.2, 0.4 and 0.6 m respectively. The spectra are normalized by the sky flux and the spectrum taken at 0.1 m depth according to Equation 5.1. Data were taken on 13 September. The site characteristics are listed in Table 5.1.

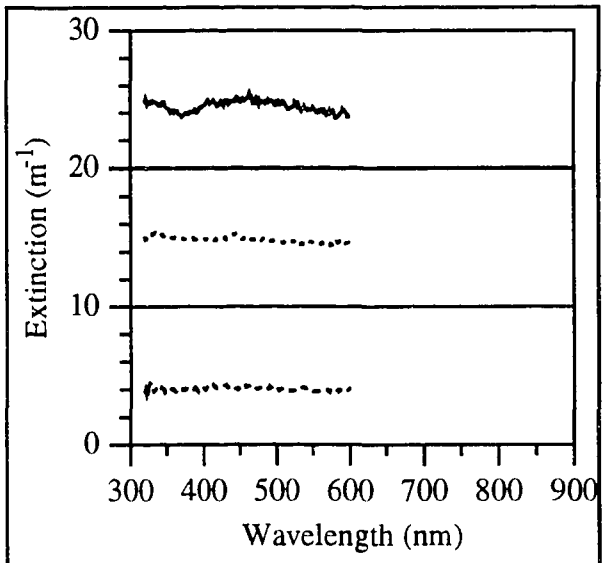

Figure 5.5b. Light extinction between the depths 0.1 - 0.2, 0.2 - 0.4 and 0.4 - 0.6 m. These curves were calculated from the data in Figure 5.2a according to Beer's law. Each curve is offset by 10 m^{-1} for clarity so that for the zero reference for the 0.1 - 0.2 m extinction is at 20 m^{-1} on the Y axis.

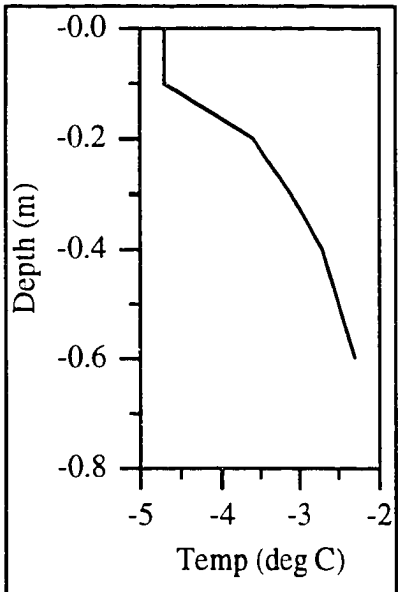

Figure 5.5c. Temperature profile of the ice for Figures 5a, b.

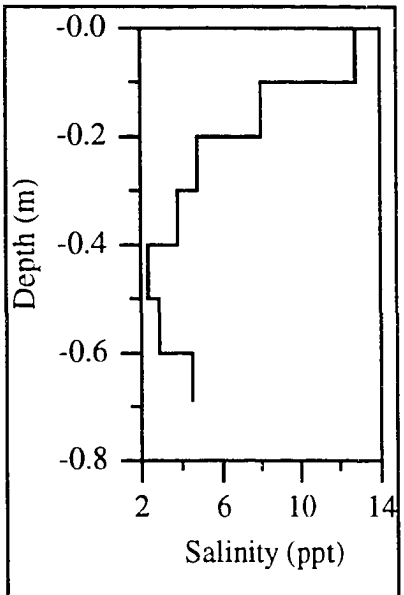

Figure 5.5d. Salinity profile of the ice for Figures 5a, b.

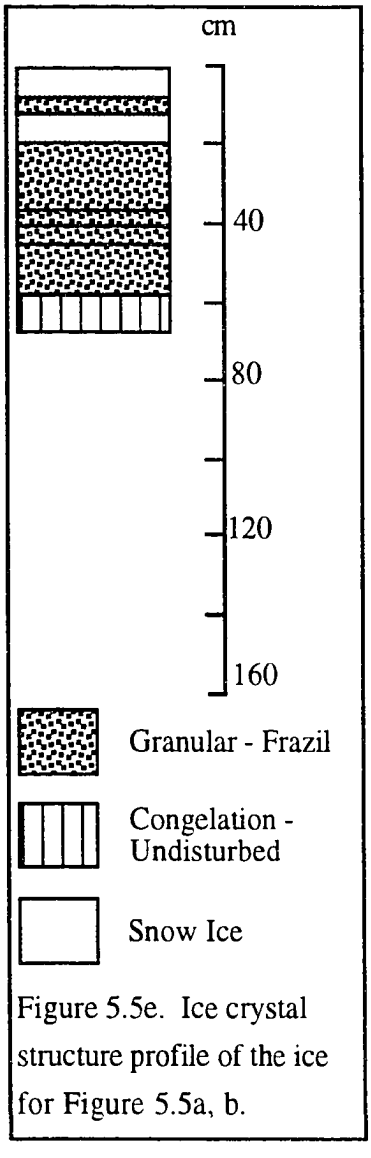

Figure 5.5e. Ice crystal structure profile of the ice for Figure 5.5a, b.

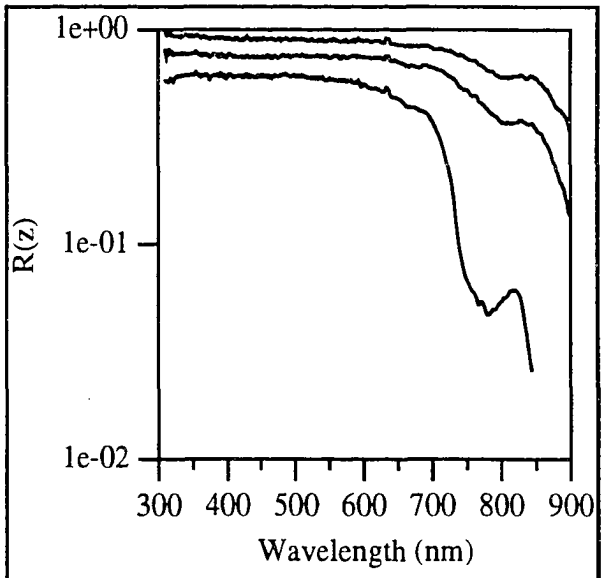

Figure 5.6a. The top to bottom curves are the downward light in sea ice at depths 0.2, 0.3 and 0.8 m respectively. The spectra are normalized by sky flux and the spectrum taken at 0.1 m depth according to Equation 5.1. Data were taken on 14 September. The site characteristics are listed in Table 5.1.

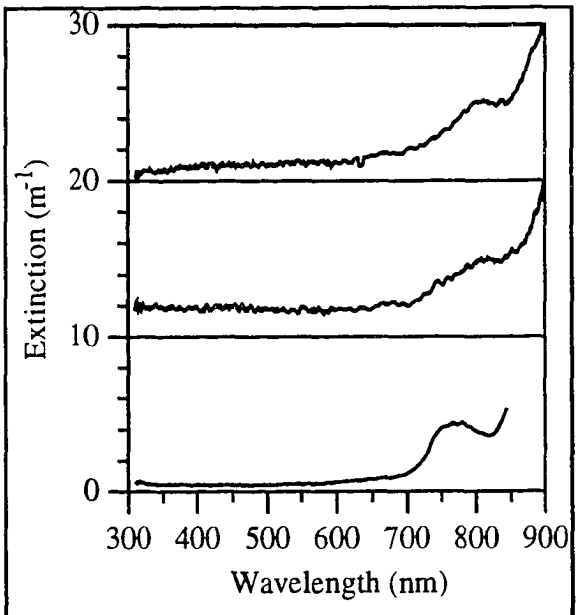

Figure 5.6b. Light extinction between the depths 0.1 - 0.2, 0.2 - 0.3 and 0.3 - 0.8 m. These curves were calculated from the data in Figure 5.6a according to Beer's law. Each curve is offset by 10 m^{-1} for clarity so that for the zero reference for the 0.1 - 0.2 m extinction is at 20 m^{-1} on the Y axis.

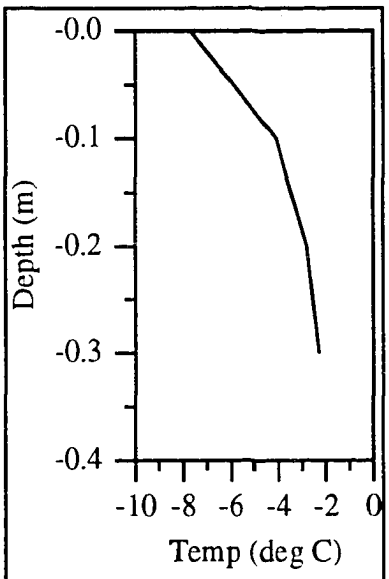

Figure 5.6c. Temperature profile of the ice for Figures 6a, b.

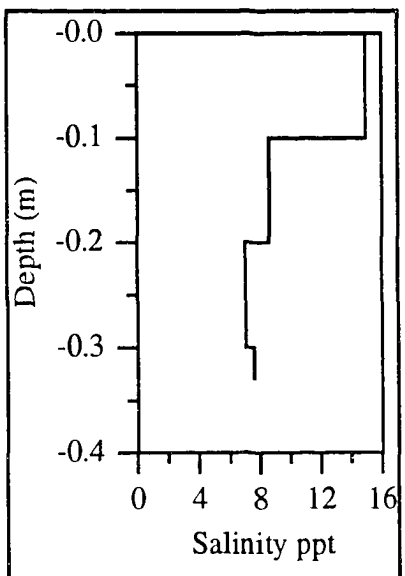

Figure 5.6d. Salinity profile of the ice for Figures 6a, b.

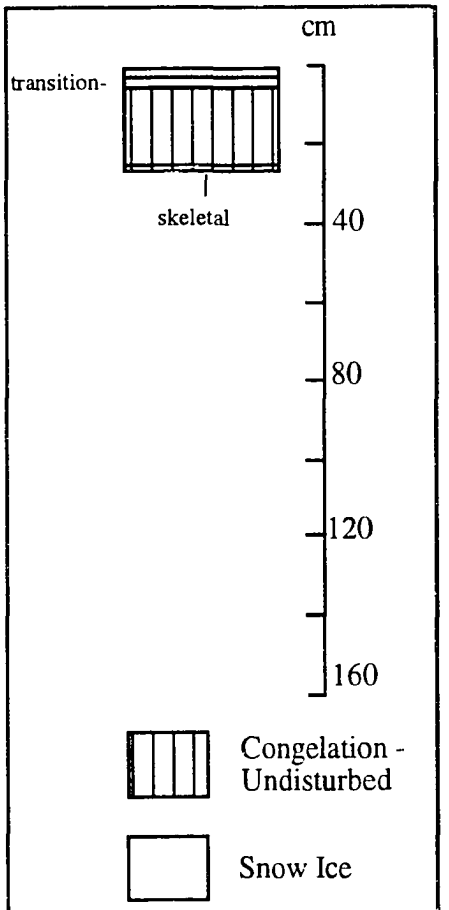

Figure 5.6e. Ice crystal structure profile of the ice for Figure 5.6a, b.

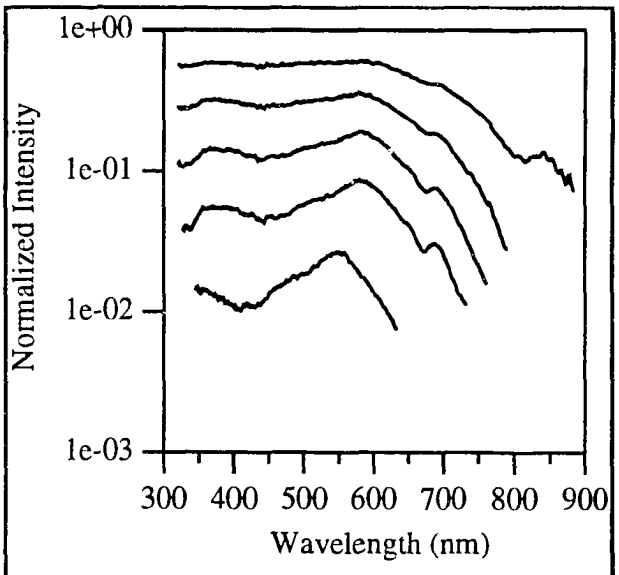

Figure 5.7a. The top to bottom curves are the downward light in sea ice at depths 0.4, 0.6, 0.8,1.0 and 1.2 m respectively. The spectra are normalized by sky flux and the spectrum taken at 0.2 m depth according to Equation 5.1. Data were taken on 15 September. The site characteristics are listed in Table 5.1.

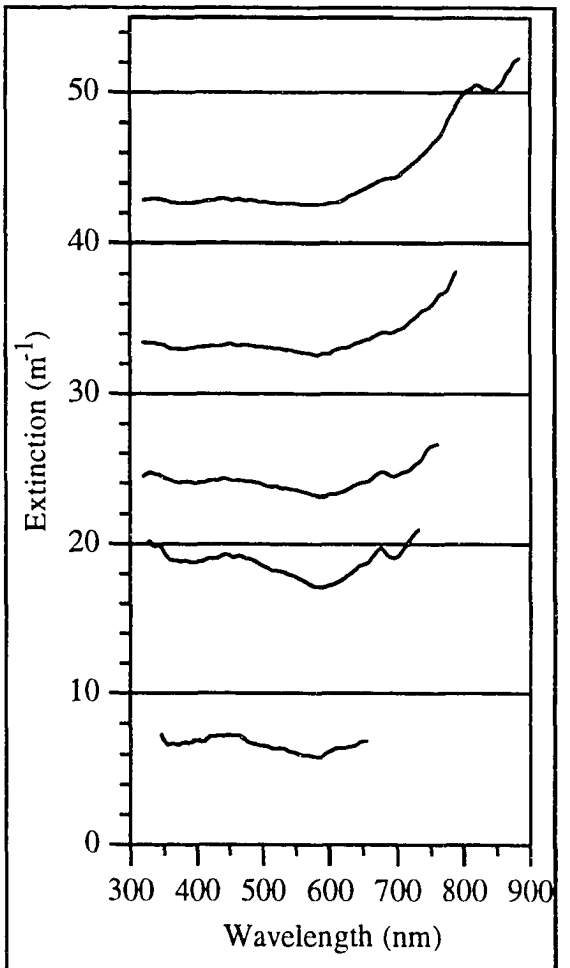

Figure 5.7b. Light extinction between the depths 0.2 - 0.4, 0.4 - 0.6, 0.6 - 0.8, 0.8 - 1.0 and 1.0 - 1.2 m. These curves were calculated from the data in Figure 5.6a according to Beer's law. Each curve is offset by 10 m^{-1} for clarity so that for the zero reference for the 0.2 - 0.4 m extinction is at 40 m^{-1} on the Y axis.

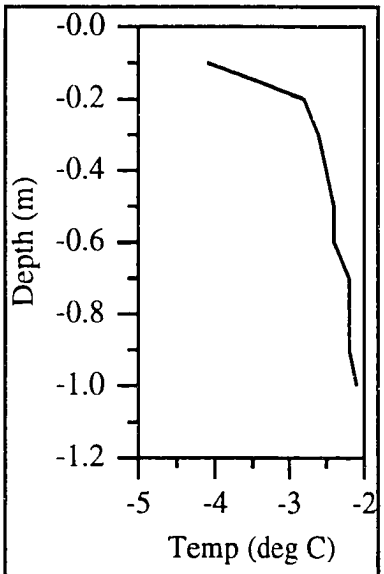

Figure 5.7c. Temperature profile of the ice for Figures 7a, b.

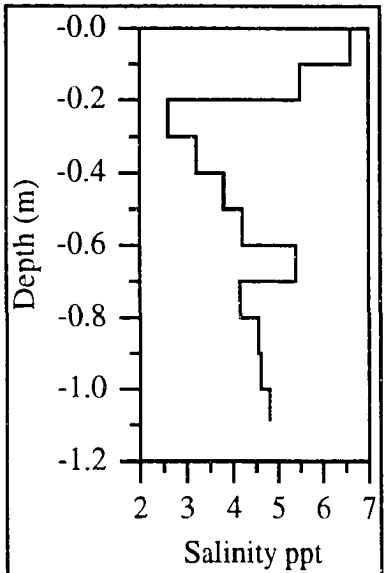

Figure 5.7d. Salinity profile of the ice for Figures 7a, b.

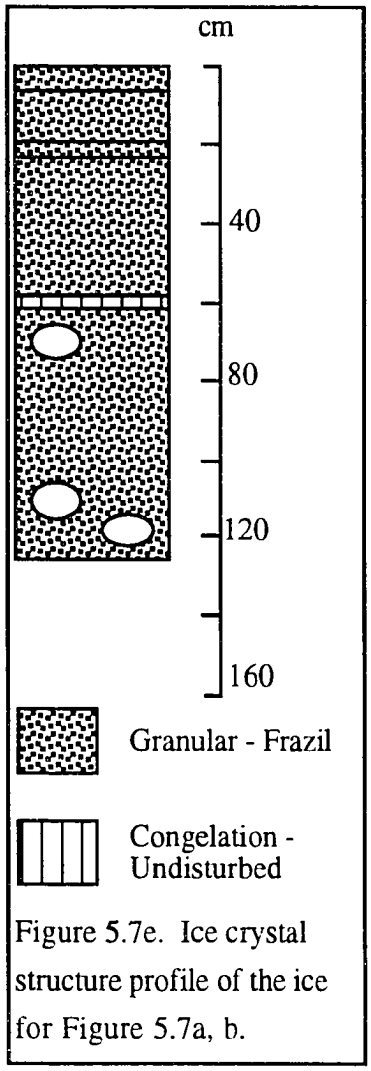

Figure 5.7e. Ice crystal structure profile of the ice for Figure 5.7a, b.

5.4 Modeled Extinction

To further examine the effects of biogenic material in sea ice, a sea ice radiative transfer model by Jin et al.[4] was used to calculate extinction values for comparison to the measurements presented here. The model used the discrete ordinate method[14,57] to numerically solve the radiative transfer equation (Equation 1.1). The boundary condition at the top of the ice was specified as an isotropic radiance field. The angular distribution of radiance in the air was approximated by 16 streams, or angular directions of travel. The Gaussian quadrature rule was used to distribute the eight upward and eight downward streams symmetrically about the horizontal angle. In the ocean, Snell's law was used to refract the atmospheric streams into the correct angles in the ocean. This range of angles is referred to as the refraction region. The range of angles in the ocean where total internal reflection occurs cannot be accounted for by refraction of atmospheric streams[58]. This range of angles is referred to as the internal reflection region. Two upward and two downward streams were added to the internal reflection region to properly account for the radiation that is scattered from the refraction region.

The optical properties of the ice in the model are absorption by pure ice, scattering and absorption by brine pockets and solid salts trapped in the ice, scattering by gas bubbles, and absorption by algae and detrital material. Values for the wavelength dependent absorption by pure ice were taken from measurements by Grenfell and Perovich[19,59]. The relative amounts of gas, brine and solid salts trapped in the ice were calculated from the ice temperature, salinity and density according to relations by Cox and Weeks[29]. The gas bubbles, brine pockets and solid salts were assumed to be spherical and Mie calculations were used to find the absorption and scattering phase functions. The gas bubbles size distribution was assumed to follow a power law $N(r) = N_0 r^{-1.24}$ with upper and lower limits of 2 and 0.1 mm. The brine pocket size distribution was assumed to be uniform with a radius of 0.6S per mm^3 (S = salinity in ppt). Significant amounts of solid salts do not appear in sea ice at temperatures above -23 °C, and the sea ice encountered in this study was well above that limit. The specific absorption spectrum of algae (Figure 1.1) was taken from measurements of absorption by single algae cells performed by Iturriaga et

al.[27]. Absorption by detrital particles[8] (biogenic material without chlorophyll) was modeled according to Equation 5.2.

$$\alpha_{detrital} = \delta c e^{-0.008(\lambda - 400nm)}$$

where

δ = fraction of absorption by algae

c = algae concentration

Equation 5.2

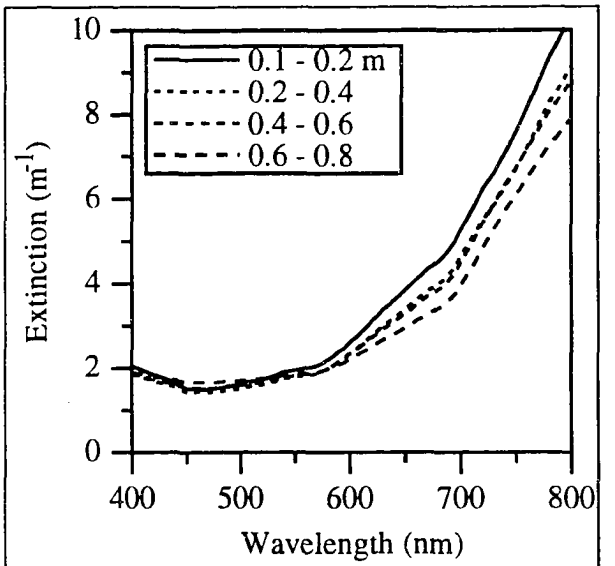

Figure 5.8a. Modeled extinction in sea ice with the physical characteristics of Figure 5.7, and no contaminants.

Measurements by Arrigo et al.[8] show that detrital absorption in sea ice in McMurdo Sound is in the range of 0% to 20% of the absorption by algae in the same samples. Algae concentrations in congelation ice varied between 3.2 and 65 (μg chlorophyll)/(ml sea ice). Algae are commonly measured by the amount of chlorophyll it contains.

The ice was divided into homogenous layers at the boundaries 0.1, 0.2, 0.4, 0.6, 0.8 and 1.24 m. The ocean was taken as a single layer between the depths 1.24 and 500 m. The ocean floor was assumed to be a Lambertian reflecting surface to satisfy the lower boundary condition. The data in Figures 5.7c, and d were used to specify the salinity and temperature profiles for the model ice. The ice density was taken to be 0.89 g/ml at all depths based on the frazil ice type in Figure 5.7e.

Downward flux profiles were generated for clean ice and a range of concentrations of algae and detrital particles. Figure 5.8a is the modeled extinction of downward flux in the clean ice between the depths 0.1 - 0.2, 02 - 0.4, 0.4 - 0.6 and 0.6 - 0.8 m. Figures 5.9 is the modeled extinction in the 0.4 - 0.6 m layer with algae in concentrations of 0, 5, 10, 15 and 20 (μg chlorophyll)/(ml ice) with no detrital material. Figure 5.10 is the downward flux

extinction in the 0.4 - 0.6 m layer with 10 (μg chlorophyll) / (ml ice) of algae, and detrital absorption fractions (δ) of 0, 0.05, 0.1, 0.15, and 0.2. The discussion of the modeled flux extinction is at the end of section 5.5.

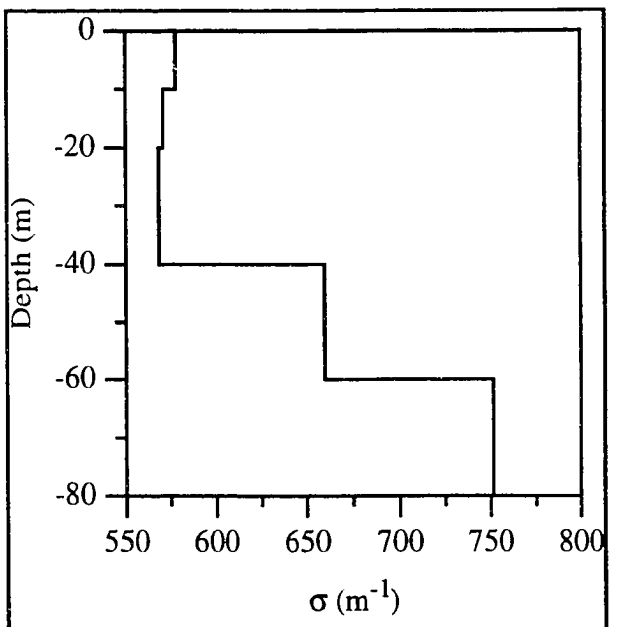

Figure 5.8b. Scattering coefficient calculated from an ice density of 0.89 g/ml, and the temperature and salinity profiles in Figures 5.7c and d.

5.5 Discussion

Figure 5.2a and b show a very strong absorption by algae. The ice appeared greenish - grey to the eye. The characteristic chlorophyll absorption peaks at 330, 430 and 680 nm appear at all depths in Figure 5.2 except for the top 20 cm. The mean extinction of the 0.1 to 0.2 m layer for $320 < \lambda < 600$ nm in Figure 5.2b is 2.2 m^{-1}. This is likely higher than the asymptotic flux extinction because the optical depth is less than the 0.48 limit measured in Chapter 4, but can give an estimate for the absorption by the contaminants in the lower layers at $\lambda = 450$ nm by using equation 1.12. Absorption by pure ice[25] at 450 nm is 0.043 m^{-1}. Using K = 2.2 m^{-1} and assuming there were very little algae in the top layer, the backscattered light is about $\sigma\beta = 56$ m^{-1}. The backscattering fraction coefficient from consolidated grease ice[25] has been measured at $\beta = 0.35$, so scattering in the ice of Figure 5.2b is about $\sigma = 120$ m^{-1}. These values can be applied to the lower layers to estimate the absorption of the algae where $\alpha = \alpha_{ice} + \alpha_{alge}$, and assuming that light scattering by algae is negligible. Table 5.2 shows the absorption by contaminants at 450 nm in Figure 5.2b. The contaminant absorption in Table 5.2 is greater than absorption by pure ice by factors ranging from 1.4 to 19.7. Also note that the scattering skin depth ($1/\sigma$) is 0.8 cm. This agrees with the observation that the ice light collector was not visible when it was lowered in the ice hole to a depth where the top of the collector was 1 cm below the ice surface, and the slush in the

hole was allowed to freeze.

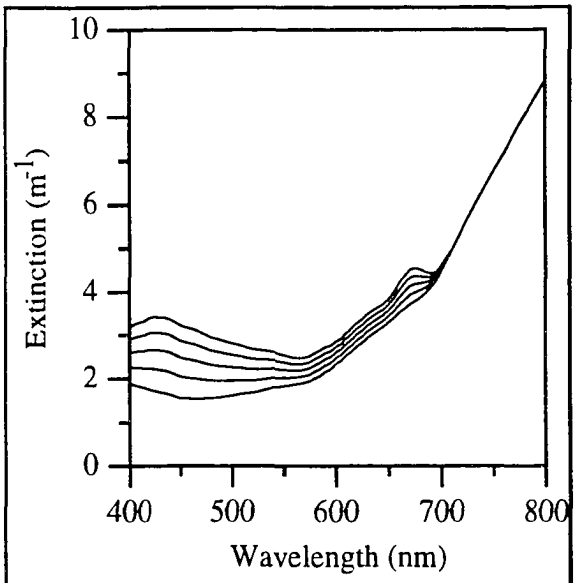

Figure 5.9. Extinction in the 0.4 - 0.6 m layer of Figure 5.8 with algae concentrations of 0, 5, 10, 15, 20 (μg chlorophyll)/(ml ice).

Figure 5.3a and b show a much cleaner piece of ice. This ice was a 0.4 m wide refrozen lead between thick greenish ice floes. Figure 5.2a - e described one of these neighboring floes. The 0.1 - 0.2 m layer in Figure 5.3b has an extinction of 3 m^{-1} for short wavelengths ($320 < \lambda < 600$ nm, similar to the same layer in Figure 5.2b. The 0.2 - 0.3 m layer in Figure 5.3b shows a much larger, but still flat extinction of about 6 m^{-1} in the short wavelengths. Even though the light collector is only 0.2 m away from green ice on two sides, Figure 5.3a and b show no signs of the spectral shape of extinction associated with the algae. The same is true for the measurement in the water between the two green floes (third curve, Figure 5.3b).

There are two possible reasons for this. The first is that the downward flux through the 35 cm thick ice is strongly centered around the vertical direction, and that the collector is receiving much more of this light than from the light exiting the sides of the green ice. The second possibility is that the amount of green light entering the sides of the refrozen lead is fairly constant with depth, even in the water below the thin clean ice. The first explanation is most likely correct considering the very short scattering skin depth of 0.8 cm calculated on the previous page, and that the light entering the top of the ice is much brighter than that entering sideways from the green ice.

Extinction in the layer between 0.3 - 0.4 m is near zero at strong scattering wavelengths, and rises where absorption by water and ice increases (third curve, Figure 5.3b). As mentioned earlier, this measurement is across the ice–ocean surface at the 0.35 m depth.

The light collector has a view of the bottom of the refrozen lead and the walls of the neighboring floes. This means there is the same amount of horizontally travelling short wavelength light in this cavity, as in the ice just above. Of course in the wavelengths longer than 700 nm, absorption by ice and water create some light loss. The bottom extinction curve in Figure 5.3b is typical for absorption in water.

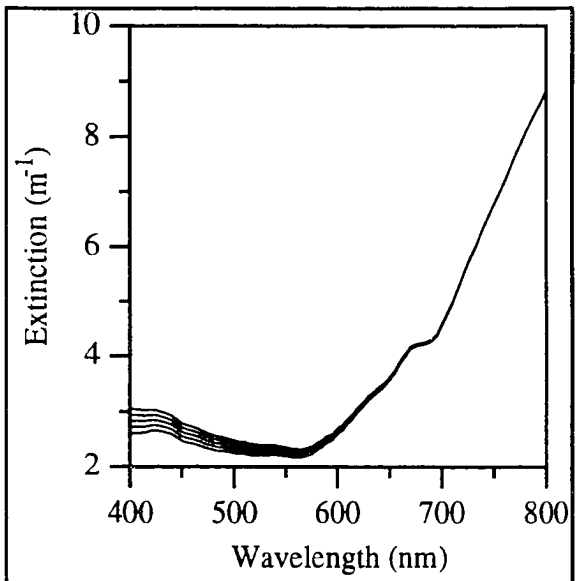

Figure 5.10. Modeled extinction in the 0.4 - 0.6 m layer of Figure 5.8 with 10 (μg chlorophyll)/(ml ice), and detrital absorption fractions (δ) of 0, 0.05, 0.1, 0.15 and 0.2 for the bottom to top curves respectively.

The albedo curves in Figure 5.4 agree with the extinction of Figures 5.2b and 5.3b. The green ice albedo (solid curve, Figure 5.4) has small peaks at 400 nm and 620 nm with sharp decreases for wavelengths shorter than 400 nm and longer than 620 nm. The dominant scattering by inclusion in the ice agrees with the flatness in the 400 - 620 nm band. The green band (500 nm) is where there is a small minimum, but blue (420 nm) and yellow (620 nm) albedo peaks are interpreted by the eye as green.

The dashed curve in Figure 5.4 shows a lower albedo which agrees with a much thinner piece of ice with little absorbing contaminants. The curve is also very flat between 400 and 620 nm with a very small peak at 420 nm.

Figure 5.5a and 5.5b show expected extinction from sea ice with small concentrations of contaminants. The ice is granular-frazil with snow ice on top, and a congelation layer on the bottom 4 cm. The extinction curves are flat in the range 320 to 600 nm. The data stop at 600 nm because measurements were not taken with the 1180 groove/mm grating that day. The small extinction dip at 370 nm in the 0.1 - 0.2 m layer is likely due to changes in

Layer Depth (m)	K(450 nm) - K(600 nm) (m^{-1})	Contaminant Absorption (m^{-1})
0.1 - 0.2	2.20	0
0.2 - 0.3	3.46	0.06
0.3 - 0.4	7.31	0.43
0.4 - 0.5	7.93	0.51
0.5 - 0.6	9.50	0.75
0.6 - 0.7	10.07	0.85
0.7 - 0.8	8.31	0.57

Table 5.2. Contaminant absorption calculated from Equation 1.12, extinction values (K) from Figure 5.2b, absorption by pure ice α_{ice} = 0.043 m^{-1}, and backscattered light $\sigma\beta$ = 56.26 m^{-1}. The backscattered light was found with Equation 1.12 and extinction in the clean 0.1 - 0.2 m layer of Figure 5.2b.

sky radiation since it does not appear in the other layers. Recall that this wavelength band was not normalized by sky flux. The mean extinctions are 4.5, 4.9, and 4.0 m^{-1} for the 0.1 - 0.2, 0.2 - 0.4 and 0.4 - 0.6 m layers respectively which match granular ice with lots of gas bubbles trapped between the crystals. Note that the extinction values do not increase toward the bottom of the ice as in the previous measurements.

Figures 5.6a - e describe another thin, clean ice floe that is warm enough to not contain any solid salts. The extinction values are smaller than the clean ice in Figure 5.5. The magnitude of 1 to 2 m^{-1} for wavelengths between 320 and 700 nm agrees with scattering by primarily brine pockets. This congelation ice likely has fewer gas bubbles than the granular ice of Figure 5.5. As expected, extinction rises from increased absorption by ice for longer wavelengths. The extinction in the water column below is also expected with shortwave extinction an order a magnitude smaller than in the ice.

Figure 5.7a and b show a very similar absorption by algae to Figure 5.2a and b. The ice is also a similar granular type with some large brine drainage features. Their extinctions are similar in both wavelength and depth. This ice floe is thicker, but the relative position of the algae is the same with the maximum extinction at 430 nm occurring in the bottom 65% to 85% of the ice. This is also entirely granular ice.

In order to investigate the effects of the lower ice boundary on the measurements, the change in extinction between the top and bottom layers was compared with the optical thickness between the bottom measurement and the bottom ice surface. Table 5.3 is a list of these values for all five ice floes. The optical thickness is based on the extinction in the bottom layer, and the geometric distance to the bottom surface ($K\Delta z$). Values at wavelength 600 nm are used to limit effects of absorption by algae. Keep in mind that there are a large number of parameters such as gas volume fraction, inclusion size distribution and other contaminants that affect this comparison.

The last two columns in Table 5.3 indicate that the changes in the optical properties of the ice effect the measured extinction more than the lower boundary. In general extinction measurements in the bottom are larger than in the upper layers, but the magnitude of the

Figure Number	K_{bottom} at 600 nm (m^{-1})	K_{top} at 600 nm (m^{-1})	K_{Bottom}/K_{top}	Bottom Optical Thickness
5.2	5.4	1.7	3.2	0.43
5.3	6.0	3.2	1.9	0.30
5.5	4.1	3.8	1.1	0.37
5.6	1.8	1.1	1.6	0.05
5.7	6.2	2.7	2.3	0.25

Table 5.3. A comparison of the rise in extinction between the top and bottom layers in sea ice (K_{bottom}/K_{top}), and the optical thickness between the bottom light measurement in the ice and the bottom surface of the ice.

change varies widely. The last spectrum in Figure 5.6a is extremely close to the bottom of the ice, and the extinction only changes by a factor of 1.6. On the other hand the optical thickness of the entire ice floe is only about 0.35, which is less than the 0.48 criterion suggested in Chapter 4.

The modeled extinction of clean ice in Figure 5.8 has extinction values between 1.6 and 2 m^{-1} in the range of 400 to 550 nm, in comparison to 3 m^{-1} in the 0.1 - 0.2 m layer of Figure 5.7b. The spectral shape of the modeled extinction has a minimum at 450 - 500 nm that does not occur in the measurements. For the case where $\alpha << 2\sigma\beta$ the two-stream model extinction of Equation 1.11 also predicts the same minimum, where extinction is proportional to the square root of absorption by pure ice. A very small 430 nm chlorophyll absorption peak is present in the top layer of Figure 5.7b which means there could be enough spectrally flat absorbing material in the ice to hide the absorption by ice. The measured extinction in the clean ice of Figures 5.3b, 5.5b and 5.6b is also very flat for wavelengths shorter than 600 nm, so the spectrally flat shortwave extinction is a property of the winter Antarctic sea ice. Scattering coefficients calculated by the model (Figure 5.8b) were very large (578 - 751 m^{-1}) compared to the absorption by ice (0.043 - 16.4 m^{-1}) as well as measured and calculated extinction (1.7 - 15 m^{-1} from Figures 5.8a and 5.7b). The point here is that the model described in section 5.4, the two-stream approximation (Equation 1.11), and measured extinction in summer sea ice (Figures 4.2b, 4.3b) shows a coupling between scattering and absorption in how they attenuate light in sea ice. This can be explained by multiple scattering by inclusions increasing the optical path length through the weakly absorbing ice and brine. The longer path length produces extinction values much larger than pure absorption by sea ice would predict, but still following a similar spectral shape. The measured extinction in the clean winter sea ice presented here does not show the coupling when light scattering is more than three orders of magnitude larger than absorption. Spectrally flat extinction has been predicted for thin winter sea ice by a four-stream model by Grenfell[3]. Extinction was calculated to be 20 m^{-1} for wavelengths between 350 and 800 nm for 1mm thick ice with a temperature of -20 °C, salinity of 4‰, and ice density of 0.925 g/ml. For 2 m thick ice, the extinction curve matched the model used here (Figure 5.8a).

The absorption peaks at 430 and 680 nm are present in Figure 5.9. The change in the extinction is fairly sensitive to the amount of chlorophyll used in the model, but there is much more increase in measured extinction values in Figures 5.2b and 5.7b between the cleaner, top layers and the algae laden bottom layers. With an increase of algae from 0 to 10 (μg chlorophyll)/(ml ice), the extinction in Figure 5.9 increased by 53% at 430 nm. Increasing the detrital material from $\delta = 0$ to 0.2 (bottom to top curve in Figure 5.10) raised the extinction by 19%. Compared to 0.2 * 53% = 11% for the increase in absorption by detritus, the 19% increase in extinction is much larger. The extinction in Figure 5.7b contains absorption by algae, detrital material, and other contaminants. This is indicated by the chlorophyll absorption peaks in the lower layers, and the large increase at all wavelengths in the 0.8 - 1.2 m layers compared to the ice above.

5.7 Conclusions

Extinction of downward flux in winter Antarctic sea ice with no contaminants was spectrally flat between 320 and 700 nm. Observed extinction magnitudes in this band were between 1 and 5 m^{-1}. The shape and size of the shortwave extinction are a result of heavy multiple light scattering by the brine and gas inclusions in the ice. Using a backscattering fraction coefficient of $\beta = 35\%$, absorption by ice of $\alpha = 0.043$ m^{-1}, and measured shortwave extinction of 2.2 m^{-1}, the scattering coefficient was estimated at $\sigma = 120$ m^{-1}. These values applied to first year, frazil, grey, sea ice with a temperature between -4 and −10 °C. The extinction curve increases for wavelengths longer than 700 nm. This is where absorption by ice increases rapidly.

The presence of algae and other contaminants in the ice was observed to increase the shortwave extinction from 2 m^{-1} for clean ice, up to 10 m^{-1} for the most effected ice layer. Absorption by the algae was estimated from a two-stream approximation at 0.85 m^{-1} for this layer. The multiple scattering of light in sea ice greatly increased the effects of absorbing material.

Algae were identified by the chlorophyll absorption peaks at 330, 430 and 680 nm. Large algae blooms were not found on the underside of the ice observed, but there were algae

distributed through the lower bulk of two ice floes. The largest algae concentration occurred in the bottom 15% to 35% of the floes that contained contaminants.

The modeled clean ice had smaller extinction values than the measurements. Also, there was a minimum at 450 - 500 nm in the modeled extinction that did not occur in the winter sea ice extinction measurements presented here. Doubling the chlorophyll concentration increased extinction at 450 nm by a factor of 1.2. Doubling the absorption fraction of detrital material in the model increased the extinction by about a factor of 1.06 at 450 nm.

Extinction from the ultraviolet-A through yellow (320 - 600 nm) in clean winter sea was spectrally flat with values ranging from 1.7 - 5 m^{-1} for different ice floes. The extinction minimum at 450 nm corresponding to the minimum in absorption by water and ice does not appear in any of the winter ice measurements. Model calculations based on an ice temperature of -3 C, salinity of 4‰, and ice density of 0.89 g/ml, produced values for scattering of 660 m^{-1} and an extinction of 1.54 m^{-1} at 450 nm. This scattering value is more than 6000 times larger than the absorption by ice and water ($\alpha < 0.1$ m^{-1}) in the shorter wavelengths (320 - 600 nm). The flat shortwave measured extinction suggests that increasing the optical path length through a weakly absorbing material by multiple scattering is not the dominant effect in this case. Since light scattering by inclusions that are larger than the wavelength of light is independent of wavelength, the flat shortwave extinction curve is likely due to light lost out the top and bottom of the ice, even though these surfaces are optically far away. The observed longwave region (600 - 900 nm) confirmed the expected rise in extinction toward longer wavelengths due to the rapidly increasing absorption by ice and brine. Measured winter ice extinction values at 900 nm were in the range of 10 to 15 m^{-1}. Modeled extinction spectra had similar or slightly lower values in the shortwave band than the measured curves. The modeled extinction also had an extinction minimum at 450 - 500 nm instead of the flat measured extinction in winter sea ice.

6. Overall Conclusions

6.1 Spectrometer Performance

The use of light collectors separated from the spectrometer by light guides allows acquiring high resolution spectra of downward travelling light in snow or sea ice. The ice light collector did not allow for downward flux measurements because it had a cosine angular response only for zenith angles between 45° and 85°. Finding a suitable fluid to fill the volume of the collector could greatly improve the angular response.

Care must be used when interpreting the data taken with this light collector. Sea ice is a strongly scattering medium so that the collected light could be assumed proportional to the downward flux at depths where any direct beam source radiation has been converted to diffuse radiation by multiple scattering events. This region was measured to be below optical depths of 0.48 from the top ice surface. This is the point where the sharply decreasing extinction was observed to approach an asymptotic value.

The spectrometer has a spectral resolution that far exceeds the spectral structure observed in sea ice. The finest absorption band is from chlorophyll at 680 nm. A 10 nm resolution easily maps the shape of this curve; the spectrometer collected data between 1 and 6 nm. The dynamic range of the instrument is useful over three orders of magnitude in brightness, although the UVA and near infrared light levels under deep snow or 2 m of sea ice are at the limits of detection.

6.2 Extinction in Antarctic Sea Ice

Measurements of light extinction in sea ice were expanded into the ultraviolet-A band. Extinction in melting summer sea ice increases from 0.7 m^{-1} at 400 nm to 1 m^{-1} at 350 nm. Light scattering was estimated by a two-stream approximation at 33 m^{-1} from an extinction of 1 m^{-1}, and an absorption by ice of 0.043 m^{-1} at 450 nm. There was also an increase in extinction at all wavelengths toward the bottom layers of the ice. This is expected due to an increased amount of downward travelling light that exits the bottom of the ice, instead of

being scattered up and into the light collector. Measurements in the wavelength range of 400 to 900 nm were in general agreement with the results of other studies of warm, blue sea ice.

Extinction from the ultraviolet-A through yellow (320 - 600 nm) in clean winter sea ice was spectrally flat with values ranging from 1.7 - 5 m^{-1}. The extinction minimum at 450 nm corresponding to the minimum in absorption by water and ice does not appear in any of the winter ice measurements. Model calculations based on an ice temperature of -3 °C, salinity of 4‰, and ice density of 0.89 g/ml, produced values for scattering of 660 m^{-1} and extinction of 1.54 m^{-1} at 450 nm. This scattering value is more than 6000 times larger than the absorption by ice and water ($\alpha < 0.1$ m^{-1}) in the shorter wavelengths (320 - 600 nm). The flat shortwave measured extinction suggests that increasing the optical path length through a weakly absorbing material by multiple scattering was not the dominant effect in this case. Since light scattering by inclusions that are larger than the wavelength of light is independent of wavelength, the flat shortwave extinction curve is likely due to light lost out the top and bottom of the ice, even though these surfaces are optically far away. The observed yellow to near–infrared region (600 - 900 nm) confirmed the expected rise in extinction toward longer wavelengths due to the rapidly increasing absorption by ice and brine. Measured winter ice extinction values at 900 nm were in the range of 10 to 15 m^{-1}. Modeled extinction spectra had similar or slightly lower values in the shortwave band than the measured curves. The modeled extinction also had an extinction minimum at 450 - 500 nm instead of the flat measured extinction in winter sea ice.

The presence of algae in the ice increased the extinction by as much as a factor of five in the shortwave region. The absorption peaks of chlorophyll at 330, 430 and 680 nm were evident in the extinction of dirty ice. Large algae blooms were not encountered on the bottom of the ice. When it was present, the algae were detected through most of the ice with the highest concentration in the bottom 15% to 35%. Doubling the chlorophyll concentration increased the modeled extinction at 450 nm by a factor of 1.2. Doubling the absorption fraction of detrital material increased the extinction by about a factor of 1.06 at 450 nm.

7. References

1. T. Grenfell, "The effects of ice thickness on the exchange of solar radiation over the polar oceans," J. Glac., **22** (1979).

2. G. Maykut and N. Untersteiner, "Some results from a time dependent, thermodynamic model of sea ice," J. Geophys. Res. **76**, 1550-1575 (1971).

3. T. Grenfell, "A radiative transfer model for sea ice with vertical structure variations," J. Geophys. Res., **96**, 16991-17001 (1991).

4. Z. Jin, K. Stamnes, W. Weeks, and S. Tsay, "The effects of sea ice on the solar energy budget in the atmosphere-sea ice-ocean system: A model study," J. Geophys. Res, in press (1994).

5. Smith, R. Prézelin, B., Baker, K., Bidigare, R., Boucher, N., Coley, T, Karentz, D., MacIntyre, S., Matlick, H., Menzies, D., Ondrusek, M., Wan, Z. and Waters, K., "Ozone depletion: Ultraviolet radiation and phytoplankton biology in Antarctic Waters," Science **25**, 952-959 (1992).

6. D. Perovich, G. Cota , G. Maykut, and T. Grenfell, "Bio-optical observations of first-year arctic sea ice," Geophys. Res. Lett. **20**, 1059-1062 (1993).

7. C. Sullivan, A. Palmisano and J. Soohoo, "Influence of sea ice and sea ice biota on downwelling irradiance and spectral composition of light in McMurdo Sound," SPIE **489** Ocean Optics VII, 159-165 (1984).

8. K. Arrigo, C. Sullivan, and J. Kremer, "A bio-optical model of Antarctic Sea Ice," J. Geophys. Res. **96**, 10581-10592 (1991).

9. J. SooHoo, A. Palmisano, S. Kottmeier, M. Lizotte, S. SooHoo and C. Sullivan, "Spectral light absorption and quantum yield of photosynthesis in sea ice microalgae and a bloom of phaeocystis pouchetii from McMurdo Sound, Antarctica," Mar. Ecol. Prog. Ser. **39**, 175-189 (1987).

10. J. Calkins and T. Thordardottir, "The ecological significance of solar UV radiation and aquatic organisms," Nature **283**, 563-566 (1980).

11. S. El-Sayed, "Effects of ultraviolet radiation on Antarctic marine phytoplankton," 5th SCAR Symposium on Antarctic Biology, Hobart, 29 Aug 1988.

12. H. Trodahl, and R. Buckley, "Ultraviolet levels under sea ice during the Antarctic Spring," Science **245**, 194-195 (1989).

13. J. SooHoo, A. Palmisano, S. Kottmeier, M. Lizotte, S. SooHoo and C. Sullivan, "AMERIEZ 1986: Photoadaptation of phytoplankton and light limitation of primary production on the ice-edge zone of the Weddell Sea," Ant. J., 185–187 (1987).

14. S. Chandrasekhar, "Radiative Transfer," Dover, 393pp (1960).

15. G. Thomas and K. Stamnes, "Radiative Transfer," to be published by Cambridge University Press.

16. T. Grenfell and G. Maykut, "The optical properties of ice and snow in the Arctic basin," J. Glac. **18**, 445-463 (1977).

17. R. Roulet, G. Maykut, and T. Grenfell, "Spectrophotometers for the measurement of light in polar ice and snow," App. Opt. **13**, 1652-1659 (1974).

18. D. Perovich and T. Grenfell, "Laboratory studies of the optical properties of young sea ice," J. Glac. **27**, 331-346 (1981).

19. T. Grenfell and D. Perovich, "Radiation absorption coefficients of polycrystalline ice from 400 - 1400 nm," J. Geophys. Res. **86**, 7447-7450 (1981).

20. D. Perovich and J. Govoni, "Absorption coefficients of ice from 250 to 400 nm," Geophys. Res. Lett. **18**, 1233-1235 (1991).

21. R. Buckley and H. Trodahl, "Scattering and absorption of visible light by sea ice," Nature **326**, 867-869 (1987).

22. H. Trodahl, R. Buckley, and S. Brown, "Diffusive transport of light in sea ice," App. Opt. **26**, 3005-3011 (1987).

23. H. Trodahl, R. Buckley, and M. Vignaux, "Anisotropic light radiance in and under sea ice," Cold Reg. Sci. Tech. **16**, 305-308 (1989).

24. H. Trodahl, "Enhanced ultraviolet transmission of Antarctic sea ice during the austral spring," Geophys. Res. Lett **17**, 2177-2179 (1990).

25. T. Grenfell and D. Hedrick, "Scattering of visible and near infrared radiation by NaCl ice and glacier ice," Cold Reg. Sci. Tech. **8**, 119-127 (1983).

26. R. Iturraiga and C. Sullivan, "Spectral light absorption characteristics of individual sea ice microalgae from McMurdo Sound, Antarctica," Ant. J., (1989).

27. R. Iturriaga, B. Mitchell and D. Kiefer, "Microphotometric analysis of individual particles absorption spectra," Limnol. Oceanogr. **33**, 128-135 (1988).

28. D. Perovich, "Theoretical estimates of light reflection and transmission by spatially complex and temporally varying sea ice covers," J. Geophys. Res. **95**, 9557-9567 (1990).

29. G. Cox and W. Weeks, "Equations for determining the gas and brine volumes in sea ice samples," J. Glac. **29**, 306-316 (1983).

30. The mention of brand names in this paper is for information purposes only and does not constitute an endorsement of the product by the authors or their institutions.

31. W. Fastie, "A small plane grating monochromator," J. Opt. Soc. Am. **42**, 641-652 (1952).

32. W. Fastie, "Experimental Performance of Curved Slits," J. Opt. Soc. Am. **43**, 1174–1175 (1953).

33. Fisher Scientific Co., "Instruction Manual for the 82-000 Series 0.5 m Ebert Scanning Spectrometer," Engineering Publication No. 82-000/IM Rev. 7 (1971).

34. T. Quakenbush, "Ultraviolet (A) and short–wave radiation on the Juneau Icefield, Alaska," in press, Polorforschung **62**, (1994).

35. J. Farman, B. Gardiner, and J. Shanklin, " Large losses of total ozone in Antarctica reveal seasonal ClO_x/NO_x interaction," Nature **315**, 207-210 (1985).

36. P. Crutzen and F. Arnold, "Nitric acid cloud formation in the cold Antarctic Atmosphere: a major cause for the springtime "ozone hole"," Nature **324**, 651-655 (1986).

37. W. Brune, "Stratospheric chemistry," Rev. Geophys. Sup., 12-24 (1991).

38. M. Miller, "Phenomena associated with the deformation of a glacier bore-hole," Extrait des Comtes et Rapports, Assemblee Generale de Toronto, 440-441 (1957).

39. C. Byers, K. Daellenbach, J. Markillie, S. McGee, and E. Peterson, "Results of the summer 1988 surveying program," Report prepared for the Juneau Icefield Research Program, 45pp (1988).

40. G. Wendler and N. Streten, "Short term heat balance study on a coast range glacier," Pure App. Geophys. **77**, 68-77 (1969).

41. M. Iqbal, "An introduction to solar radiation," Academic Press, 390pp (1983).

42. L. Garrison, L. Murray, D. Doda, and A. Green, "Diffuse-direct ultraviolet ratios with a compact double monochromator," App. Opt. **17**, 827-836 (1978).

43. W. Livingston, "Landscape as viewed in the 320 nm ultraviolet," J. Opt. Soc. Am. **37**, 1653-1657 (1983).

44. J. Bolsenga, "Spectral reflectance of snow and fresh-water ice from 340 through 1100 nm," J. Glac. **29**, 296-305 (1983).

45. G. Liljequist, "Radiation and wind and temperature profiles over an Antarctic snowfield," Toronto Met. Conference, Royal Met. Soc. London, 78-87 (1954).

46. I. Dirmhirn and E. Trojer, "Albedomessungen auf dem hintereisferner," Archiv für Meteorologie, Geophysik und Bioklimatologie **6**, 400-416 (1955).

47. S. Warren, "Optical properties of snow," Rev. Geophys. Space. Phy. **20**, 67-89 (1982).

48. T. Grenfell, and D. Perovich, "Spectral albedos of an alpine snow pack," Cold Reg. Sci. Tech. **4**, 121-127 (1981).

49. F. Eaton and I. Dirmhirn, "Reflected Irradiance Indicatrices of Natural Surfaces and their effect on albedo," App. Opt. **18**, 994-1008 (1979).

50. W. Ambach and H. Eisner, "Albedo verschiedener schneeoberflächen für erythemwirksame solare strahlung," Wetter und Leben **38**, 1-4 (1986).

51. G. Wendler, F. Eaton, and T. Otake, "Multiple reflection effects on irradiance in the presence of Arctic stratus clouds," J. Geophys. Res. **86**, 2049-2057 (1981).

52. J. Dozier, R. Davis and A. Nolin, "Reflectance and transmittance of snow at high spectral resolution," IEEE Geophys. Rem. Sen. Soc. **2**, 662-664 (1989).

53. W. Ambach and H. Mocker, "Messungen der strahlungsextinktion mittels eines kugelförmigen empfängers in der oberflächennahen eisschicht eines gletschers und im alteis," Archiv für Meteorologie, Geophysik und Bioklimatologie **10**, 84-99 (1959).

54. G. Wendler, "Some measurements of the extinction coefficient of river ice," Polarforschung **6**, 253-256 (1970).

55. M. Jeffries, R. Shaw, K. Morris, A. Veazy and H. Krouse, "Crystal structure, stable isotopes ($\delta^{18}O$), and development of sea ice in the Ross, Amundsen, and Bellingshausen seas," J. Geophys. Res. **99**, 985-995 (1994).

56. G. Weller, "Radiation diffusion in Antarctic ice media," Nature **221**, 355-356, (1969).

57. K. Stamnes, S. Tsay, W. Wiscombe and K. Jayaweera, "Numerically stable algorithm for discrete–ordinate–method radiative transfer in multiple scattering and emitting layered media," Appl. Opt. **27**, 2502-2509, (1988).

58. Z. Jin and K. Stamnes, "Radiative transfer in nonuniformly refracting layered media: atmosphere–ocean system," Appl. Opt. **33**, 431-442, (1994).

59. S. Warren, "Optical constants of ice from the ultraviolet to the microwave," Appl. Opt. **23**, 1206-1225, (1984).